Modeling and Control of Dielectric Elastomer Enabled Actuators for Soft Robots

Wenjun Ye

A Thesis
in
The Department
of
Mechanical, Industrial and Aerospace Engineering

Presented in Partial Fulfillment of the Requirements
for the Degree of
Doctor of Philosophy (Mechanical Engineering) at
Concordia University
Montréal, Québec, Canada

January 2024

Concordia University
School of Graduate Studies

This is to certify that the thesis prepared

By: **Mr. Wenjun Ye**

Entitled: **Modeling and Control of Dielectric Elastomer Enabled Actuators for Soft Robots**

and submitted in partial fulfillment of the requirements for the degree of

Doctor of Philosophy (Mechanical Engineering)

complies with the regulations of this University and meets the accepted standards with respect to originality and quality.
Signed by the Final Examining Committee:

_____ Chair
Dr. Rabindranath Raut

_____ External Examiner
Dr. Xiang Chen

_____ External to Program
Dr. Lan Lin

_____ Examiner
Dr. Youmin Zhang

_____ Examiner
Dr. Javad Dargahi

_____ Co-supervisor
Dr. Chun-Yi Su

_____ Co-supervisor
Dr. Farhad Aghili

Approved by _____
Graduate Program Director

_____ 2023

_____
Mourad Debbabi, Dean
Gina Cody School of Engineering and Computer Science

Abstract

Modeling and Control of Dielectric Elastomer Enabled Actuators for Soft Robots

Wenjun Ye, Ph.D.
Concordia University, 2024

The field of robotics has undergone a significant transformation, extending its scope well beyond its traditional role in manufacturing automation. It has now found applications in various domains such as healthcare, field exploration, and collaborative human-robot interactions. Nevertheless, a main concern across these diverse applications remains the safety of interactions involving humans. Traditional robots, comprised of rigid links and joints, inherently carry risks when operating close to human beings. This risk is exacerbated by the absence of compliance in their actuation mechanisms. In contrast, soft robots are constructed from inherently soft or extensible materials, affording them the ability to deform and absorb energy during collisions. This distinctive characteristic endows them with a continuously deformable structure and muscle-like actuation, closely resembling biological systems and offering a greater number of degrees of freedom. Consequently, soft robots hold the potential to exhibit extraordinary levels of adaptability, sensitivity, and agility.

The emergence of soft robots marks a new frontier at the intersection of multiple disciplines, including engineering, materials science, mechanics, physics, chemistry, biology, and robotics. This interdisciplinary confluence catalyzes innovation, pushing the boundaries of robotic capabilities and unlocking fresh avenues for exploration and practical applications.

Among the materials ideally suited for soft robotics, Dielectric Elastomer (DE) is one of the promising candidates due to its exceptional performance attributes. However, the intricate nonlinear characteristics inherent to Dielectric Elastomer Actuators (DEAs), including phenomena such as hysteresis, stress relaxation, and various dependencies, pose great challenges in modeling and control.

This dissertation is dedicated to advancing the modeling and control strategies for Dielectric Elastomer Actuators (DEAs) with the primary objective of integrating them into soft robot applications.

The research endeavors commence with a solid foundation in the form of extensive experimental tests. These tests investigate the input-output characteristics of DEAs, systematically exploring their responses under varying input amplitudes, frequencies, and mechanical loads. The experimental results unveil intricate and multifaceted behaviors influenced by factors such as input frequencies, amplitudes, and external mechanical loads.

This study focuses specifically on conical and planar Dielectric Elastomer Actuators (DEAs) and introduces two distinct models based on fundamental physical principles. These proposed models are inspired by the concept of free energy within viscoelastic materials, allowing them to comprehensively capture the intricate behaviors exhibited by DEAs while considering their complex dependencies. Particularly, these models can describe the intricate influences of multiple factors that shape DEA behaviors. The precision and effectiveness of these models are rigorously validated through meticulous comparisons with experimental data.

Due to the necessity for actuator-specific details in physics-based models, an innovative approach is presented, namely a data-in-loop model. This groundbreaking model adopts nonlinear elements, encompassing phenomena such as creep and hysteresis, thus avoiding the need for geometry-specific information and effectively representing the intricate behaviors of DEAs.

The presence of nonlinear effects in DEAs can lead to harmful consequences, including inaccuracies, oscillations, and instability. To effectively counter these effects, a controller design approach is proposed, adopting feedforward inverse compensation methods for controller design. In this framework, a model based on Prandtl-Ishlinskii (PI) hysteresis blocks is adopted to account for the nonlinearities within DEAs. The direct inverse compensation technique is employed with the inverse of the PI model. Building upon this foundation, a robust adaptive controller is then developed. This comprehensive methodology is designed to mitigate the adverse impacts of nonlinearities in DEAs, ultimately enhancing their control performance and addressing the formidable challenges posed by dynamic behaviors.

Acknowledgments

I am sincerely grateful to all those who have been a guiding light and a source of support during my Ph.D. studies. Their unwavering assistance, invaluable constructive feedback, and heartfelt advice have been instrumental in shaping my research and personal growth.

First and foremost, my deepest appreciation goes to my esteemed supervisors, Dr. Chun-Yi Su and Dr. Farhad Aghili. Their profound insights, unceasing encouragement, and unwavering support have been pivotal throughout my academic pursuit and the process of crafting this thesis.

A special mention must also be made for my adorable pets, whose love, encouragement, and companionship have provided solace and motivation, making the accomplishment of my Ph.D. study all the more meaningful.

Lastly, I extend my heartfelt thanks to my colleagues and friends: Dr. Jundong Wu, Dr. Yawu Wang, Mr. Peng Huang, and Dr. Pan Zhang, among others. Their selfless assistance and kindness have been a cornerstone of my academic journey.

In this moment of achievement, I am humbled by the community that has stood by me. My gratitude knows no bounds for the collective impact of all these wonderful individuals on my academic and personal endeavors.

Contents

List of Figures ix

List of Tables xiii

Nomenclature xiv

1 Introduction 1

1.1 A Brief Introduction to Soft Robots . . . 2

1.2 Dielectric Elastomer Actuators (DEAs) . . . 4

1.2.1 Advancement of Dielectric Elastomer Actuators and Their Benefits . . . 4

1.2.2 Working Principle . . . 4

1.2.3 Dielectric Elastomer Materials . . . 6

1.3 Input-Output Responses of DEAs . . . 7

1.3.1 Description of the Experimental Platform . . . 7

1.3.2 The Input and Output Responses of DEAs . . . 8

1.3.3 Experimental Results Summary . . . 10

1.4 Objectives and Contributions . . . 14

1.4.1 Objectives of the Dissertation Research . . . 14

1.4.2 Contributions of the Dissertation Research . . . 15

1.5 Organization of the Thesis . . . 16

2 Literature Review 18

2.1 Modeling of DEAs . . . 18

2.2 Control of DEAs . . . 22

2.2.1 Model Free Control Strategy . . . 23

2.2.2 Model Based Control Strategy . . . 24

3 Physics Based Modeling for Dielectric Elastomer Actuators 26
3.1 Introduction . . . 26
3.2 Physics Based modeling for Dielectric Elastomer Actuators with Conical Shape . . . 26
3.2.1 Model Development . . . 26
3.2.2 Actuation Voltages . . . 34
3.2.3 Parameters Identification . . . 35
3.2.4 Model Validation . . . 36
3.3 Physics Based modeling for Planar Dielectric Elastomer Actuators . . . 52
3.3.1 Model Development . . . 52
3.3.2 Actuation Voltages . . . 57
3.3.3 Parameters Identification . . . 58
3.3.4 Model Validation . . . 58
3.4 Concluding Remarks . . . 64

4 Data-in-Loop Modeling for Dielectric Elastomer Actuators 68
4.1 Introduction . . . 68
4.2 Data-in-Loop Dynamic Model of DEAs . . . 68
4.2.1 Electrical Modeling . . . 68
4.2.2 Mechanical Modeling . . . 70
4.2.3 Electromechanical Coupling . . . 71
4.3 Creep Block . . . 72
4.4 Hysteresis Block . . . 73
4.4.1 Introduction to Hysteresis Nonlinearities Models . . . 73
4.4.2 Hysteresis Structure Selection . . . 80
4.5 Mechanical Part . . . 80
4.6 Parameter Identification . . . 81
4.7 Model Validation . . . 83
4.8 Concluding Remarks . . . 84

5 Control Approach for Dielectric Elastomer Actuators with data-in-loop Model 91
5.1 Introduction . . . 91
5.2 Problem Statement . . . 92
5.3 Prandtl-Ishlinskii (PI) Hysteresis Model . . . 93
5.3.1 Play Operator . . . 94
5.3.2 Prandtl-Ishlinskii Model . . . 95

5.3.3 Some Advantages of PI Model . . . 96
5.3.3.1 Inverse Prandtl-Ishlinskii Model (Inverse PI Model) . 97
5.3.3.2 Decomposition of Discrete Prandtl-Ishlinskii Model . 98
5.4 Controller Design . . . 98
5.4.1 Controller Structure . . . 99
5.4.2 Virtual Control Law Design . . . 100
5.4.3 Dynamic Parameter and Hysteresis Adaptation . . . 100
5.4.4 Stability Analysis . . . 101
5.5 Simulation Study . . . 102
5.6 Experimental verification . . . 104
5.7 Concluding Remarks . . . 106

6 Conclusions and Future Work **107**
6.1 Concluding Remarks . . . 107
6.2 Recommendations for Future Works . . . 108
6.3 Publications . . . 109

References **112**

List of Figures

Figure 1.1 Mobile soft-robotic systems inspired by a range of biological systems. [1] . . . 3
Figure 1.2 Illustration of actuation strain versus actuation pressure/density for various actuation technologies [2] . . . 5
Figure 1.3 Working principle of DEA [3] . . . 6
Figure 1.4 The experimental platform . . . 8
Figure 1.5 The conical shape DE actuator . . . 9
Figure 1.6 Input-output relation of DEA with different frequencies . . . 10
Figure 1.7 Input-output relation of DEA with different frequencies . . . 11
Figure 1.8 Input-output relation of DEA with different amplitudes . . . 12
Figure 1.9 Input-output relation of DEA with different amplitudes . . . 12
Figure 1.10 Input-output relation of DEA with different external loads . . 13
Figure 1.11 Input-output relation of DEA with different external loads . . 13
Figure 2.1 Structure of mechanics based models . . . 21
Figure 3.1 States of the DEA. (a) Undeformed state, (b) Pre-stretched state, and (c) Electro-deformed state. . . . 27
Figure 3.2 Displacement of element in cylindrical coordinates: (a) Cylindrical coordinates, and (b) Displacement of element in each state. 30
Figure 3.3 Rheological Model: Part A exclusively comprises a spring, whereas each unit in Part B is composed of a spring in conjunction with a series-wound dashpot. . . . 32
Figure 3.4 Picture of experimental platform, which mainly includes computer, high voltage amplifier, laser distance sensor, I/O module and conical DEA. . . . 34
Figure 3.5 Diagram of driving voltage applied in parameters identification. 36
Figure 3.6 Differential Evolution algorithm used for identification . . . 37
Figure 3.7 Comparison of model prediction and experimental result with different driving voltage amplitudes and different frequencies. . . . 38

Figure 3.8 Error between model prediction and experimental result. . . . 39
Figure 3.9 Comparisons of model prediction and experimental result with driving voltage frequency $0.2Hz$ 40
Figure 3.10 Comparisons of model prediction and experimental result with driving voltage frequency $0.4Hz$ 41
Figure 3.11 Comparisons of model prediction and experimental result with driving voltage frequency $0.6Hz$ 42
Figure 3.12 Comparisons of model prediction and experimental result with driving voltage frequency $0.8Hz$ 43
Figure 3.13 Comparisons of model prediction and experimental result with driving voltage frequency $1.0Hz$ 44
Figure 3.14 Comparisons of model prediction and experimental result with driving voltage amplitude $6.0kV$ 45
Figure 3.15 Comparisons of model prediction and experimental result with driving voltage amplitude $6.5kV$ 46
Figure 3.16 Comparisons of model prediction and experimental result with driving voltage amplitude $7.0kV$ 47
Figure 3.17 Comparisons of model prediction and experimental result with driving voltage amplitude $7.5kV$ 48
Figure 3.18 Comparisons of model prediction and experimental result with driving voltage amplitude $8.0kV$ 49
Figure 3.19 Comparisons of model prediction and experimental result corresponding to force versus time 50
Figure 3.20 Comparisons of model prediction and experimental result corresponding to force versus displacement 50
Figure 3.21 Comparisons of model prediction and experimental result corresponding to force versus voltage 51
Figure 3.22 Amplitude-frequency response curve 51
Figure 3.23 States of the DEA. (a) Initial state. (b) Pre-stretching state. (c) Electro-deformed state 52
Figure 3.24 The generalized Kelvin model, which is divided into two main parts 53
Figure 3.25 Mechanical relation diagram of a spring and damper in an element of the generalized Kelvin model 55

Figure 3.26 Picture of experimental platform for planar DEA, which mainly includes computer, high voltage amplifier, laser distance sensor, I/O module and planar DEA. 57
Figure 3.27 Differential Evolution algorithm used for identification 59
Figure 3.28 Comparison of model output and experimental result with different amplitudes and frequencies. 60
Figure 3.29 Comparison between model output and experimental results at a driving voltage frequency of 0.2 Hz 61
Figure 3.30 Comparison between model output and experimental results at a driving voltage frequency of 0.6 Hz 62
Figure 3.31 Comparison between model output and experimental results at a driving voltage frequency of 1.0 Hz 63
Figure 3.32 Comparison between model output and experimental results at a driving voltage amplitude 6.0 kV 65
Figure 3.33 Comparison between model output and experimental results at a driving voltage amplitude 7.0 kV 66
Figure 3.34 Comparison between model output and experimental results at a driving voltage amplitude 8.0 kV 67
Figure 4.1 Schematic diagram of electrical model 69
Figure 4.2 Schematic diagram of viscoelastic model 70
Figure 4.3 Schematic diagram of electromechanical coupling 72
Figure 4.4 Input-output relationship of creep operator (4.7 73
Figure 4.5 Schematic diagram of electrical model 74
Figure 4.6 Relay Operator 77
Figure 4.7 Preisach Model 77
Figure 4.8 Krasnoselskii-Pokrovskii (KP) model 78
Figure 4.9 Play operator and stop operator 79
Figure 4.10 Oneside play operator 81
Figure 4.11 Simplified Kelvin-Voigt model 82
Figure 4.12 Selected DEAs model 83
Figure 4.13 Model validation with driving voltage frequency $0.2Hz$ 84
Figure 4.14 Model validation with driving voltage frequency $0.4Hz$ 85
Figure 4.15 Model validation with driving voltage frequency $0.6Hz$ 86
Figure 4.16 Model validation with driving voltage frequency $0.8Hz$ 86
Figure 4.17 Model validation with driving voltage frequency $1.0Hz$ 87
Figure 4.18 Model validation with driving voltage amplitude 6.0 kV 87

Figure 4.19 Model validation with driving voltage amplitude 6.5 kV 88
Figure 4.20 Model validation with driving voltage amplitude 6.0 kV 89
Figure 4.21 Model validation with driving voltage amplitude 6.5 kV 89
Figure 4.22 Model validation with driving voltage amplitude 8.0 kV 90
Figure 5.1 Simplified DEA model with assumptions 92
Figure 5.2 Structure of the control problem for DEAs 94
Figure 5.3 Play operator and stop operator 95
Figure 5.4 Hysteresis nonlinearities described by PI model 96
Figure 5.5 The structure of the controller 100
Figure 5.6 Trajectory tracking of the developed controller, with disturbances 103
Figure 5.7 Prediction of system parameter $\theta = 3$, with and without disturbances 104
Figure 5.8 Tracking error of the system with hysteresis actuator, with and without disturbances 104
Figure 5.9 Trajectory tracking for $x_d = 0.1(0.5 + \sin(t))\ mm$ 105
Figure 5.10 Control signal for $x_d = 0.1(0.5 + \sin(t))\ mm$ 106

List of Tables

Table 1.1 Comparison between EAP and widely used transducer actuators [4] 6
Table 1.2 Typical materials for DEAs 7
Table 3.1 Parameters of the conical DEA model. 37
Table 3.2 Errors of model validation with different driving voltage amplitudes. 39
Table 3.3 Errors of model validation with different driving voltage frequencies. 45
Table 3.4 Geometry parameters of DEA for experiment platform 58
Table 3.5 Parameters of the planar DEA model. 59
Table 3.6 Modeling errors across various driving voltage amplitudes . . . 61
Table 3.7 Modeling errors across various driving voltage amplitudes . . . 64
Table 4.1 Identified parameters of the data-in-loop model. 83
Table 5.1 Controller Parameters 103

Nomenclature

$\hat{\cdot}$	estimated variables
$\tilde{\cdot}$	estimation errors
Δ	disturbances
δ_i	stress
ϵ	Permittivity
ϵ_0	permittivity of the vacuum
ϵ_r	relative permittivity of the DE material
Γ_i	learning gain
$\lambda_{\cdot}$	stretches of DEA
$\lambda_{pre,\cdot}$	pre-stretches of DEA
μ_i	shear moduli of spring i
$\Omega(r)$	initial loading curve
ϕ	voltage on DEA
$\Pi[v](t)$	hysteresis nonlinearity
Π^{-1}	inverse hysteresis
ρ	density of DE material
θ	unknown dynamic parameters
$\varphi(x)$	known basis functions

$\xi_{\cdot,\cdot}$	stretches induced by the dashpots
$C(\cdot)$	creep nonlinearity
D	electric displacement
d_i	thickness of DEA in status i
e	tracking error
$F_r(t)$	output of Play operator
$H(\cdot)$	hysteresis nonlinearity
$H_a(t)$	output of asymmetric hysteresis
J_i	deformation limits of spring i
K	control gain
p(r)	density function on threshold r
Q	charge on electrodes
R	frame radius
R_0	loading plate radius
T_{em}	electromechanical coupling coefficient of the DEA
V_i	volume of DEA in status i
W	free energy densigy
w(t)	output of PI hysteresis model
W_s	free energy density attributed to elastomer's stretching

Chapter 1

Introduction

This dissertation sets out to provide a comprehensive exploration of the modeling and control aspects pertaining to Dielectric Elastomer (DE) enabled Actuators, a highly promising avenue for the advancement of soft robotics. Within this chapter, we initiate by introducing both the advantages and drawbacks associated with these materials, thereby establishing the motivation underlying our proposed research.

In light of the advancements within the realm of material sciences, Dielectric Elastomers (DEs) have emerged as a frontrunner among actuation materials for soft robots. The recognition of their potential has sparked the impetus to incorporate DEs into the domain of soft robotics.

Within the literature, coupled with insights drawn from our own experiments, it becomes evident that the input and output responses of DE-enabled actuators encompass intricate dynamic behaviors. However, existing research findings are at a relatively nascent stage and lack a control-oriented perspective. As a consequence, these findings cannot be readily applied to our research objectives. To address this gap, we have devised an independent experimental platform termed the Dielectric Elastomers Actuators (DEAs) system. Through this platform, we have undertaken a series of comprehensive tests encompassing different geometries, input amplitudes, frequencies, and external loads. The objective of this empirical endeavor is to gain a profound understanding of the input-output behaviors exhibited by DEAs.

Drawing upon the extensive data garnered from our experiments, we subsequently propose modeling and control strategies. These strategies are developed with the intent of enhancing the precision of control for DEAs, serving as the principal goal that drives this dissertation.

1.1 A Brief Introduction to Soft Robots

Industrial robots predominantly consist of rigid materials like metal and plastic, enabling them to excel in tasks requiring precise and repetitive actions within controlled environments. However, this rigidity becomes a limitation when dealing with unknown external constraints or obstacles, hindering their adaptability to unstructured surroundings. Traditional industrial robots struggle to modify their shapes to accommodate such dynamic environments.

As the field of robotics extends its reach from traditional manufacturing automation to domains like healthcare, field exploration, and collaborative human-robot manipulation, the significance of soft robots becomes increasingly evident. Soft robots possess the unique ability to undergo substantial deformations and navigate through unstructured and constrained environments. Unlike their hard-bodied counterparts, soft robots are constructed using intrinsically soft and/or extensible materials, allowing them to deform and absorb energy during collisions. This unique characteristic results in a continuously deformable structure with muscle-like actuation, resembling biological systems and providing a greater number of degrees of freedom. Consequently, soft robots have the potential to exhibit remarkable levels of adaptation, sensitivity, and agility.

This emergence of soft robots represents a new frontier at the intersection of multiple disciplines, encompassing engineering, materials science, mechanics, physics, chemistry, biology, and robotics. The convergence of these fields is driving innovation and redefining the boundaries of what robots can achieve, opening up new avenues for exploration and practical applications.

As depicted in Figure 1.1, soft robots possess the potential to showcase unparalleled levels of adaptation, sensitivity, and agility. These robots are anticipated to have the capability to flex and contort with remarkable curvatures, rendering them suitable for operation within constrained spaces [5]. By changing their structures in a continuous way, soft robots can achieve movements that closely mimic biological motions [6]. Furthermore, they can dynamically adjust their form to accommodate various environmental conditions, utilizing compliant locomotion for object manipulation [7], traverse rugged terrains while maintaining resilience [8], or execute rapid and agile maneuvers akin to evasive actions observed in fish [9].

In the last decade, the realm of soft robotics has experienced remarkable expansion, resulting in the creation of a multitude of soft robot variations that employ a diverse array of actuation technologies and mechanisms [8; 10–12]. The advancement

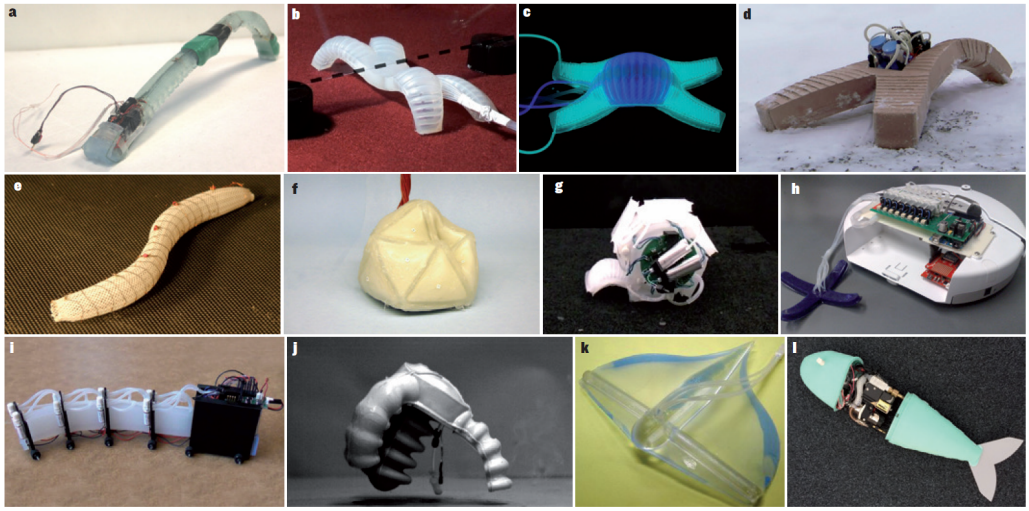

Figure 1.1: Mobile soft-robotic systems inspired by a range of biological systems. [1]

of soft robotics primarily derives its impetus from principles of bioinspiration and biomimicry, harnessing the intrinsic potential for significant and continuous deformations, often characterized by an ostensibly infinite spectrum of degrees of freedom. Segmenting these soft robots based on disparities in their actuation technologies, they can be effectively categorized into two principal groupings.

The first category centers around tendon-driven actuation, often referred to as continuum robots, distinguishing them from discrete and serpentine robots that incorporate rigid links [13]. Depending on the chosen tendon-driven mechanism, which can involve intrinsic actuators, extrinsic actuators, or a combination of both (intrinsic-extrinsic hybrid actuators), continuum robots can be designed to exhibit elasticity along with an extensive array of infinite degrees of freedom (DOFs). These characteristics have found successful applications within medical and search and rescue domains. Nevertheless, it is noteworthy that such continuum robots typically rely on conventional motors and transmission mechanisms (such as gears and ball screws), which precludes them from embodying true softness in their structures.

The second category is rooted in soft smart materials actuation. In contrast to tendon-driven actuation reliant on conventional motors and transmission mechanisms, soft smart materials have the intrinsic capability to directly convert various physical stimuli—such as force, electrical, thermal, magnetic, light, or chemical signals—into tangible physical displacements. Within this category, the commonly employed soft smart materials for the construction of soft robots encompass a range of options, including shape memory alloys (SMAs), shape memory polymers (SMPs), pneumatic fiber braids, elastomeric polymers, hydrogels [14], and electroactive polymers (EAPs).

Among those materials mentioned, Dielectric Elastomers (DEs), which fall under the category of electronic electroactive polymers (EAPs), hold particular promise within the burgeoning domain of soft robotics. This promise is rooted in their notable attributes, including lightweight composition, substantial deformability, elevated energy density, rapid responsiveness, and inherent softness [4; 15; 16].

1.2 Dielectric Elastomer Actuators (DEAs)

1.2.1 Advancement of Dielectric Elastomer Actuators and Their Benefits

The repertoire of commonly utilized soft smart materials for the construction of soft robots encompasses several categories, including shape memory alloys (SMAs), shape memory polymers (SMPs) [17], pneumatic fiber braids, elastomeric polymers, hydrogels [14], and electroactive polymers (EAPs). Notably, Dielectric Elastomer Actuators (DEAs) stand out as a distinctive electrically driven soft smart material actuator [18]. DEAs operate by responding to an applied external voltage, yielding substantial deformations. DEAs hold particular promise for applications within the realm of soft robotics. This promise is rooted in the distinctive amalgamation of attributes they possess: extensive deformation capabilities ($> 100\%$), elevated energy density ($> 3.4 MJm^{-3}$), rapid response times (in the millisecond range), lightweight composition (approximating that of water), and cost-effectiveness (within the range of hundreds of commercial elastomer products). An especially noteworthy advantage lies in the fact that dielectric elastomers function as motion-generating materials, mirroring the characteristics of natural human muscles in terms of force, strain (displacement per unit length or area), and actuation pressure/density. This distinctiveness positions them as superior compared to alternative contenders, as illustrated in Figure 1.2[2]. Table 1.1 gives a comparison among the popular soft materials for actuators.

1.2.2 Working Principle

The fundamental working principle of dielectric elastomer actuators (DEAs) is easily comprehensible [3]. In general, Dielectric Elastomer Actuators (DEAs) are constructed with a thin membrane of dielectric elastomer, wedged between two compliant electrodes. This structural composition renders DEAs essentially as pliable

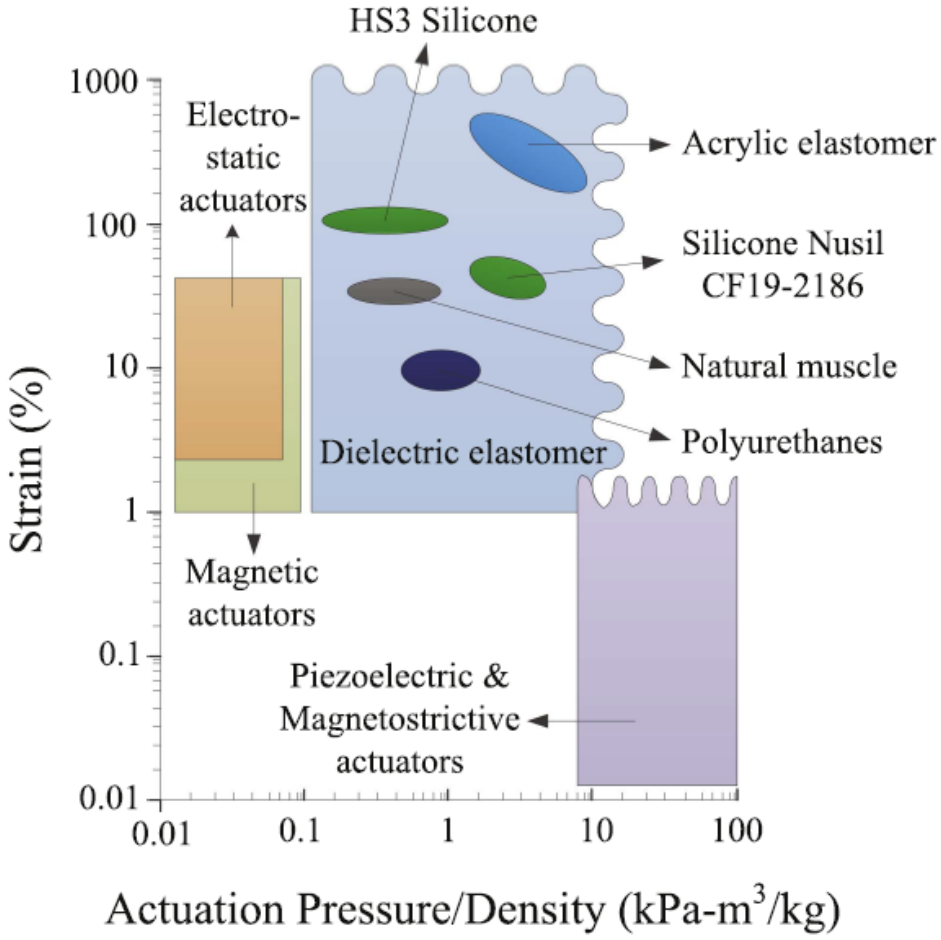

Figure 1.2: Illustration of actuation strain versus actuation pressure/density for various actuation technologies [2]

variable capacitors. The compliant electrodes, fashioned from an even more yielding material, exhibit mechanical stiffness lower than that of the dielectric elastomers [34]. The operational principle of DEAs hinges on what is referred to as electrostatic deformation. Upon the application of an electric field across the electrodes, charges traverse an external conducting pathway, moving from one electrode to the other. The consequent electrostatic force between the opposing charges on the two electrodes induces compression of the membrane's thickness. Given that dielectric elastomers are essentially impervious to compression, this compression results in a simultaneous expansion of the membrane's planar area. These alterations in shape seamlessly convert electrical energy into mechanical energy, thereby furnishing the mechanism of actuation. The working principle of this actuation is illustrated in Figure 1.3.

Table 1.1: Comparison between EAP and widely used transducer actuators [4]

Property	Electronic EAP	SMA	EAC
Actuation strain	Over 300%	$< 8\%$ (short fatigue life)	Typically $0.1\% - 0.3\%$
Force	0.1–25 MPa	200 MPa	$30 - 40MPa$
Reaction speed	μ sec to min	millisecond to minute	microsecond to second
Drive voltage	1–2.5 g/cc	5 - 6 g/cc	6 - 8 g/cc
Consumed power	10 - 150 $V/\mu m$	5 V	50 - 800 V
Fracture behavior	Resilient, elastic	Resilient, elastic	Fragile

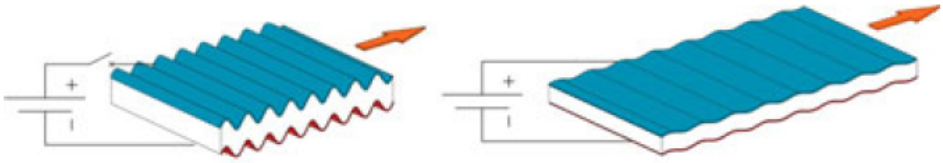

Figure 1.3: Working principle of DEA [3]

1.2.3 Dielectric Elastomer Materials

The significance of the thin membrane composed of dielectric elastomers becomes evident when examining Figure 1.3. In the realm of dielectric elastomer research, materials possessing a broad spectrum of elastic moduli are imperative, coupled with exceedingly low viscosity and electrical conductivity, in addition to high dielectric constant and breakdown strength[19]. Over the course of the past two decades, a considerable array of elastomeric materials has undergone rigorous testing. These commonly utilized elastomers can be broadly categorized into two primary groups: acrylics and silicones.

As indicated by reports [20; 21], acrylics emerge as a highly promising choice for accomplishing significant strain in DEAs. The attractiveness of acrylics is further bolstered by the availability of the cost-effective 3M VHB acrylic elastomer line, prominently exemplified by widely employed variants such as VHB 4910 and VHB 4905. Recent advancements have spotlighted DEAs employing prestretched 3M VHB acrylic elastomers, leading to the achievement of substantial voltage-induced linear strains exceeding 380% and area strains surpassing 1000% [2]. Nonetheless, it is important to note that acrylics do exhibit robust viscoelastic nonlinearity, a trait that can potentially impact DEA performance, particularly if adequate measures are not taken to accurately account for this viscoelastic behavior.

DEAs employing silicone elastomers exhibit reduced actuation strains compared to DEAs utilizing acrylics. Nevertheless, silicone elastomers hold the distinct advantage of displaying lower viscoelastic tendencies when contrasted with acrylics. They are known for their capability to operate at higher frequencies while incurring fewer losses, as reported in [2]. However, akin to acrylics, silicones also exhibit a relatively low dielectric constant. Consequently, achieving substantial strains mandates the application of elevated electric fields. Table 1.2 compares two typical materials for DEAs.

Table 1.2: Typical materials for DEAs

Polyacrylate	Polydimethylsiloxane
VHB	PDMS
Strong viscosity	Relatively low viscosity
Very large deformation $> 380\%$	Relatively small deformation
Dielectric constant around 4.8	Dielectric constant around 2.8
Relative high actuating voltage	Very high actuating voltage

1.3 Input-Output Responses of DEAs

The input and output responses in DEAs serve as a critical benchmark for evaluating actuator performance. In the existing literature, the scrutiny of actuator input-output responses remains an area that lacks comprehensive exploration. To the best of our knowledge, a thorough investigation encompassing a diverse spectrum of input frequencies, amplitudes, and mechanical loads has not yet been conducted. This knowledge gap prompts our initiative to undertake experimental tests on the input-output responses ourselves. Accordingly, we have developed a dedicated DEA testbed. Subsequently, a series of experimental tests have been executed on this platform. The acquired experimental data constitute valuable resources for our subsequent endeavors in comprehending, modeling, and controlling the input-output responses of the actuator within the context of this dissertation.

1.3.1 Description of the Experimental Platform

The test of input and output responses is conducted within the framework of the designed DEA experimental system. As shown in Figure 1.4, this platform encompasses the following components:

Computer: Serving as the central control unit, a desktop computer orchestrates the system's operations.

I/O module: A data interface (Model number: PCIe-6361; Manufacturer: National Instruments, USA). facilitates the transmission of voltage signals to the amplifier and the retrieval of displacement signals from the laser sensor.

High voltage amplifier: A TREK high voltage amplifier (Model number: 10/40A-HS-H-CE; Manufacturer: TREK, USA), characterized by a gain of $1000V/V$, is employed to generate the necessary driving voltage to power the DEAs.

Laser distance sensor: Utilizing a KEYENCE laser sensor (Model number: LK-H152; Manufacturer: Keyence, Japan) endowed with a resolution of $1\mu m$, the platform accurately measures the displacement exhibited by the DEA.

DE actuator: One conical and one planar DEAs are fabricated. They are mainly assembled by five components: (1) DE membrane (Material: PDMS; Manufacturer: Wacker Chemie AG, Germany; Undeformed thickness: $d_0 = 200\mu m$). (2) Frame (Material: Polymethyl methacrylate (PMMA). (3) Load-bearing plate (Material: PMMA). (4) Electrode (Material number: DD-10; Manufacturer: Saidi Technology, China). (5) Adjustable external weight.

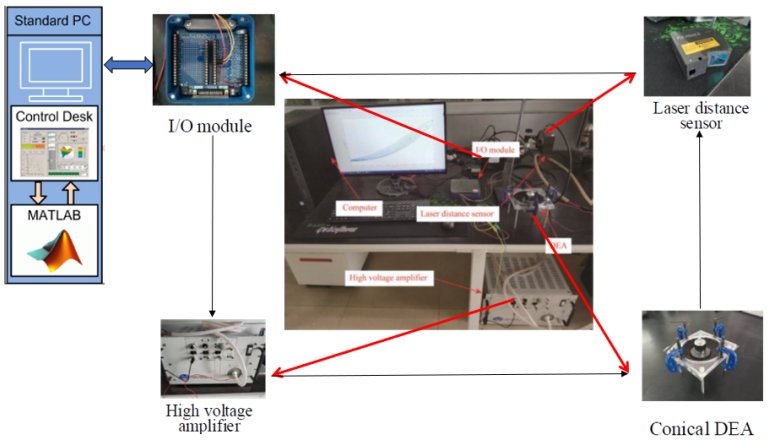

Figure 1.4: The experimental platform

1.3.2 The Input and Output Responses of DEAs

Utilizing the devised experimental platform, a series of investigations have been conducted to scrutinize the operational characteristics of Dielectric Elastomer

Actuators (DEAs), as visually depicted in Fig. 1.5. The adopted DEA consists primarily of five distinct constituent elements:

1. Dielectric Elastomer (DE) membrane crafted from Polydimethylsiloxane (PDMS), sourced from Wacker Chemie AG, Germany. The undeformed thickness of the DE membrane is denoted as $d_0 = 200\mu m$.

2. Structural frame constructed from Polymethyl methacrylate (PMMA), featuring an inner circular geometry with a radius of $R = 6cm$.

3. Load-bearing plate, also fabricated from PMMA, possessing a circular geometry with a radius of $R_0 = 3cm$.

4. Electrode material identified as MG Chemicals-846-Carbon Conductive Grease, sourced from MG Chemicals.

5. Weight element with a mass of $m = 200g$.

These components collectively constitute the conical DEA platform employed in the study of DEAs' behavior.

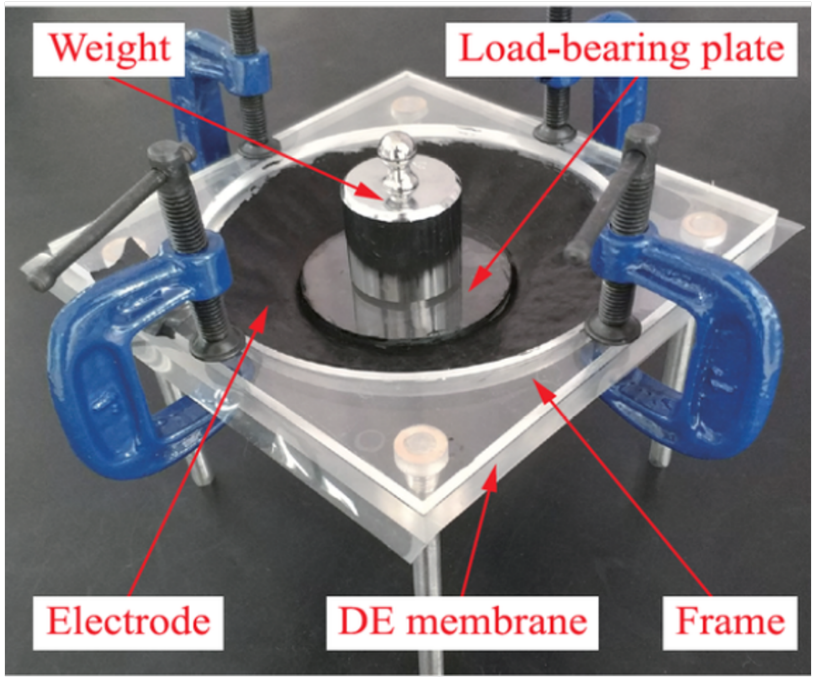

Figure 1.5: The conical shape DE actuator

The resulting input-output relationships of DEAs are depicted in Figures 1.6 to 1.11. These figures illustrate the outcomes obtained from the experimental trials.

It can be observed that the input ouptut responses of DEAs are highly nonlinear. Like the other smart materials, it shows the hysteresis nonlinearity behaviors.

In Figure 1.6, a range of input signals with distinct frequencies have been applied to the system, revealing an evident frequency-dependent behavior in the system's responses. The validity of this dependency is confirmed through Figure 1.7, showcasing the response to varying frequency input signals.

Furthermore, Figures 1.8 and 1.9 underscore that the responses of DEAs are intrinsically tied to the amplitudes of the input signals.

In the context of Figures 1.10 and 1.11, the exhibited responses demonstrate that external loads exert a discernible influence on the input-output behaviors of DEAs.

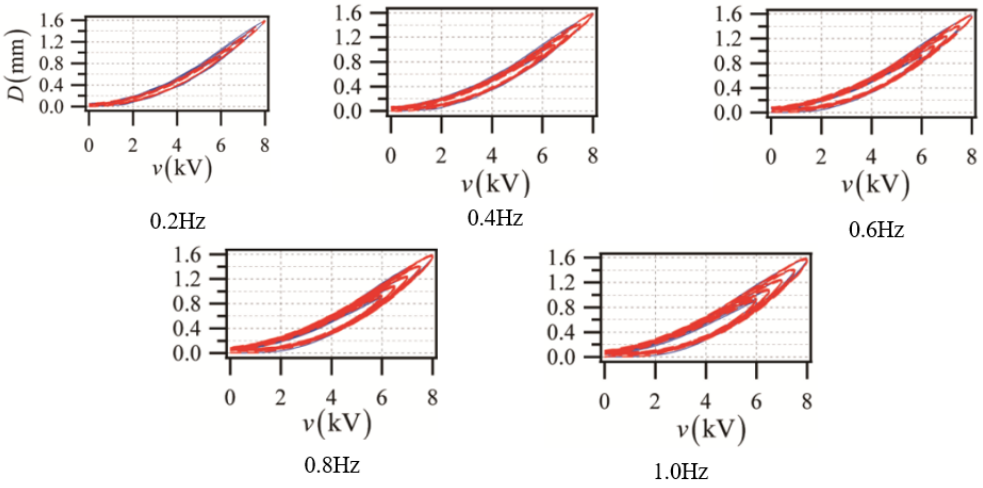

Figure 1.6: Input-output relation of DEA with different frequencies

1.3.3 Experimental Results Summary

Based on the results derived from the aforementioned experimental tests, it can be inferred that DEAs exhibit highly nonlinear behaviors, characterized by:

Memory effect The actuator's output is not solely contingent on the current input, but also on the input's historical progression.

Multiple dependency As evidenced in Figs. 1.6 to 1.11, the configurations of input-output relationships are influenced by signal frequency, signal magnitude, and external loads.

Asymmetry The input-output relationships do not demonstrate symmetry; their patterns are distinct in both input and output directions.

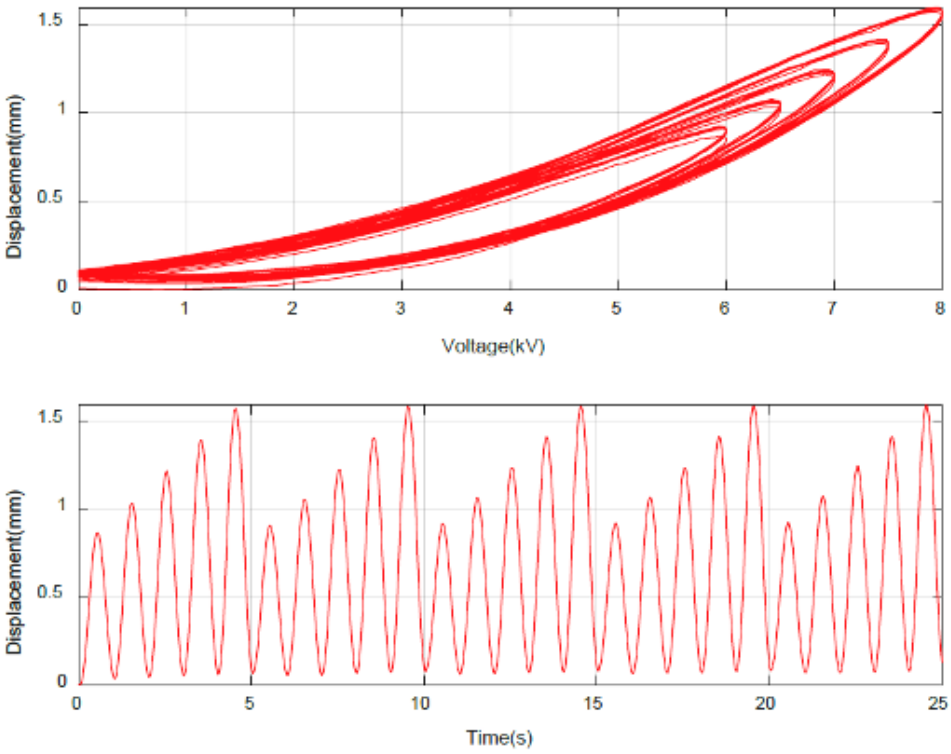

Figure 1.7: Input-output relation of DEA with different frequencies

Dynamic diversity In practical applications, actuators are often interconnected with the dynamics of the underlying system, adding an additional layer of complexity to the problem.

These findings collectively emphasize the intricate and multifaceted nature of DEA behaviors, underscoring the need for comprehensive modeling and control strategies.

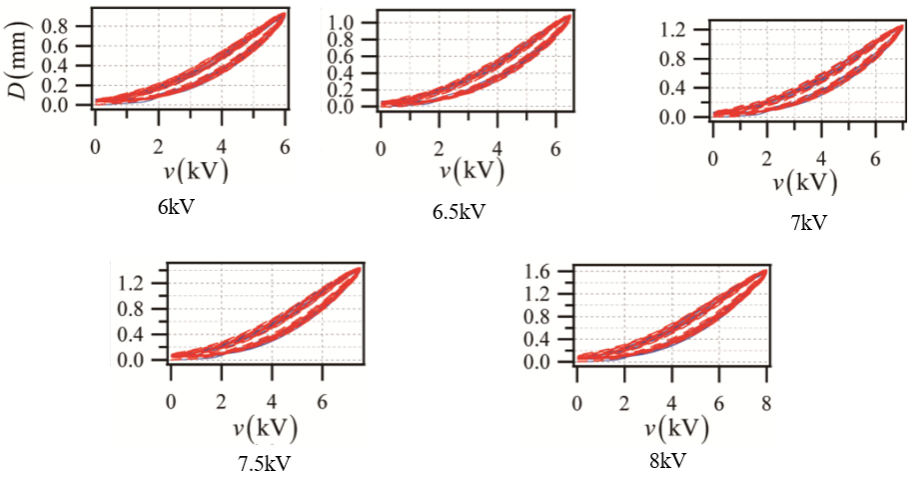

Figure 1.8: Input-output relation of DEA with different amplitudes

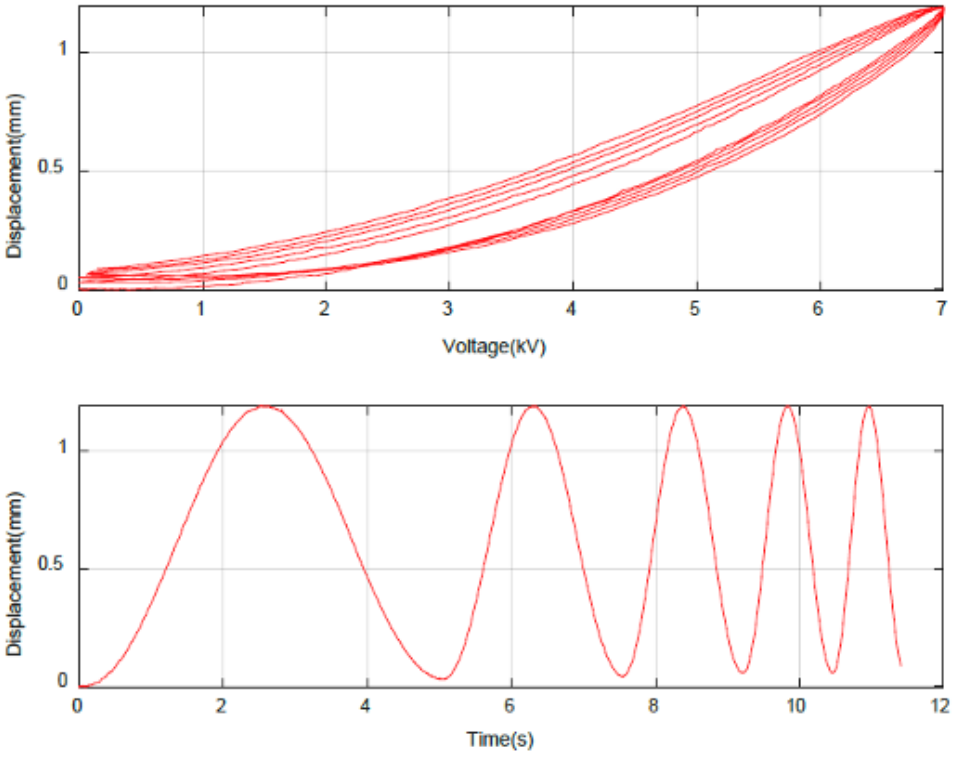

Figure 1.9: Input-output relation of DEA with different amplitudes

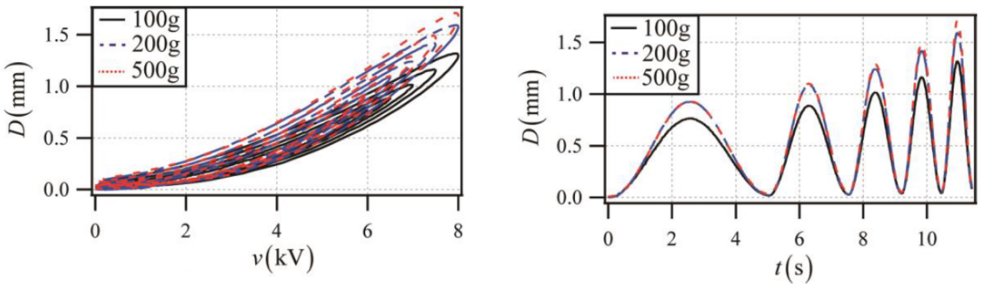

Figure 1.10: Input-output relation of DEA with different external loads

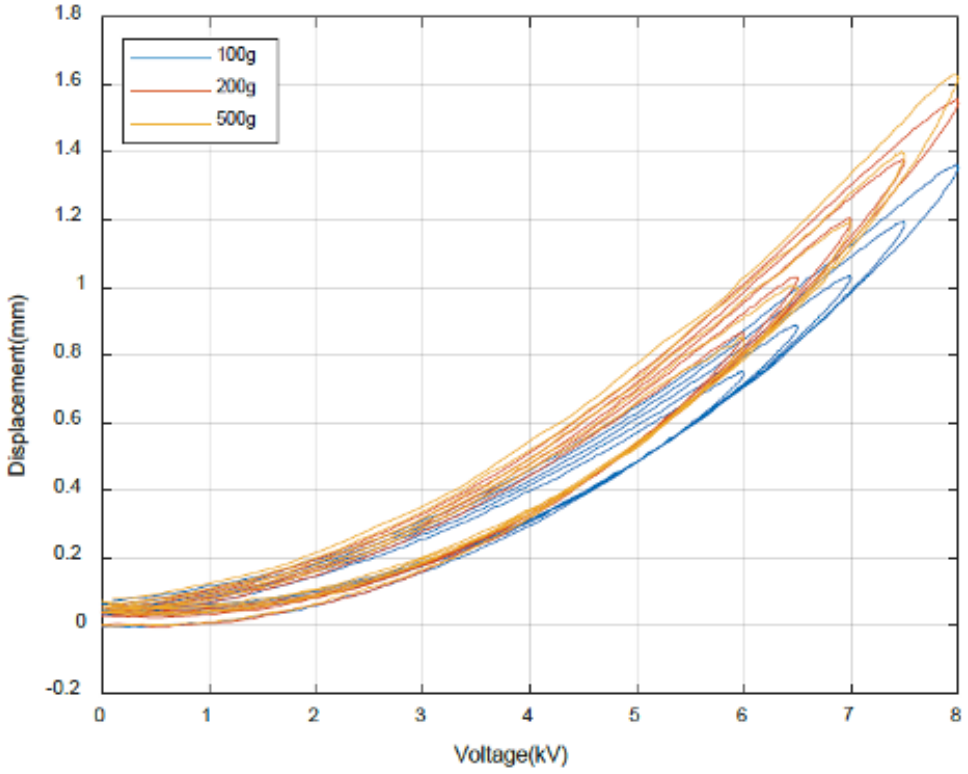

Figure 1.11: Input-output relation of DEA with different external loads

1.4 Objectives and Contributions

1.4.1 Objectives of the Dissertation Research

The experimental outcomes presented in Section 1.3 clearly demonstrate the intricate and dynamic nonlinear behaviors observed in the input and output responses of DEAs. This type of nonlinearity in actuator systems is widely recognized to lead to inaccuracies, oscillations, and other unexpected behaviors within control systems. Such effects present considerable challenges in applying these actuators effectively. Consequently, the primary objective of this dissertation research is to devise a robust modeling and control framework capable of mitigating the complexities arising from these nonlinear effects. The ultimate goal is to enhance the tracking performance of DEAs, enabling their more reliable and precise application.

In order to comprehensively comprehend and elucidate the intricate nonlinear phenomenon evident in the input and output responses of DEAs, it is paramount to formulate an encompassing model that aptly characterizes these behaviors. As discussed earlier, the input-output characteristics of DEAs exhibit multifaceted nonlinear attributes resulting from the interplay of diverse input frequencies and mechanical loads. Notably, the existing literature does not offer models tailored to these novel actuators that take into account these specific properties. Consequently, the need arises to pioneer the development of new models capable of accurately encapsulating these intricate behaviors. The forthcoming research endeavors will be dedicated to crafting these innovative models that align with the distinctive characteristics of DEAs.

Enhancing the positioning and tracking performance of DEAs necessitates the development of a tailored control scheme grounded in the newly devised dynamic model. The intricacy inherent in this endeavor lies in the integration of established control methodologies with the bespoke dynamic model. The challenge pertains to effectively amalgamating these existing control strategies with the unique attributes of the developed dynamic model. To concur this challenge, a feedforward inverse compensation approach rooted in the dynamic model will be formulated. This approach will serve as a vital conduit, effectively linking the developed model with the existing control methodologies. By leveraging feedforward inverse compensation, the distinctiveness of the dynamic model can be incorporated into the control strategies, enabling enhanced positioning and tracking capabilities for DEAs.

1.4.2 Contributions of the Dissertation Research

Following the aforementioned objectives, the primary contributions of this dissertation can be emphasized as follows:

1. A comprehensive set of experimental tests has been carried out to analyze the input-output characteristics of DEAs across varying input amplitudes ($6.0kV - 8.0kV$), frequencies ($0.2Hz - 1Hz$), and mechanical loads ($m = 100g - 500g$). The experimental results have undergone meticulous scrutiny, yielding significant insights. The experimentation reveals the following observations: (1) The input-output responses of DEAs are marked by their intricate and complex nature; (2) The observed responses exhibit notable dependency on factors such as input frequencies, input amplitudes, and external mechanical loads. These findings underscore the multifaceted behaviors exhibited by DEAs in response to various input conditions and provide crucial groundwork for the subsequent modeling and control strategies.

2. Focusing on conical DEAs and planar DEAs, this dissertation introduces two distinct models derived from the fundamental principles of physics. Drawing inspiration from the concept of free energy within viscoelastic materials, these proposed models are designed to encapsulate the intricate behaviors exhibited by DEAs, encompassing their complex dependencies. Notably, these models are adept at capturing the interplay of multiple factors influencing DEA behaviors. The accuracy and efficacy of the proposed models are substantiated through the scrutiny of experimental results. These empirical validations serve to underscore the models' aptitude in accurately representing the nuanced behaviors of DEAs, enhancing our understanding and control of these dynamic systems.

3. The models outlined above demand an extensive array of actuator-specific details, necessitating the development of separate models for distinct actuators, including detailed geometry specifications. To circumvent this limitation, a more versatile approach is presented: a data-in-loop model. This innovative model employs an array of nonlinear blocks, encompassing features such as creep and hysteresis, thereby enabling the representation of intricate DEA behaviors without relying on geometry-specific information. By employing this approach, the model sidesteps the requirement for actuator-specific details and can effectively capture the multifaceted behaviors of DEAs. Furthermore, this data-in-loop model has the capacity to accommodate and represent the complex

dependencies inherent in DEA systems.

4. The nonlinear effects exhibited in DEAs can lead to adverse consequences that undermine their performance, resulting in inaccuracies and oscillations. To counteract these detrimental effects, a strategic approach is employed: the application of feedforward inverse compensation methods for controller design. Anchored in this approach, a model founded on PI (Proportional-Integral) hysteresis blocks is deployed to effectively characterize the nonlinear impact within DEAs. The direct inverse compensation technique is then harnessed to deduce the inverse of the PI model. Building upon this foundation, a robust adaptive controller is meticulously formulated. By leveraging this comprehensive methodology, the aim is to mitigate the adverse impacts stemming from nonlinearities in DEAs, ultimately enhancing their control performance and ameliorating the challenges posed by dynamic behaviors.

1.5 Organization of the Thesis

The structure of the dissertation is organized as follows:

In Chapter 2, an overview of modeling and control methodologies, along with an in-depth exploration of the current state-of-the-art in the realm of Dielectric Elastomer Actuators (DEAs) are provided.

In Chapter 3, the attention will be directed towards conical and planar DEAs. Within this context, two physics-based models will be meticulously developed, each tailored to the respective geometry. The chapter will also delve into methods for identifying relevant parameters and will present experimental validations to substantiate the efficacy of the models.

In Chapter 4, the development of a data-in-loop model tailored for DEAs is investigated. It is designed to overcome the need for geometry-specific information. This model comprises an array of selectable nonlinear blocks, including elements like creep blocks, hysteresis blocks, and mechanical components. In practice, a model featuring a first-order creep structure, a PI hysteresis structure, and a simplified Kelvin model is employed as an implementation example, effectively showcasing the validation of the proposed methodologies. This chapter elucidates the practical application of the data-in-loop approach and its ability to encapsulate the intricate behaviors of DEAs.

In Chapter 5, the nonlinear effects present in DEAs through compensation

techniques are addressed. Specifically, feedforward inverse compensators are constructed to counteract the nonlinear impact within the context of PI hysteresis. Building upon this foundation, the chapter proceeds to develop an inverse-based robust adaptive controller designed to effectively manage the complex behaviors of DEAs. This chapter outlines the strategic approach taken to enhance the control performance and stability of DEAs in the presence of nonlinearities.

In the concluding Chapter 6, the dissertation wraps up by providing a comprehensive summary of the findings and outcomes. Furthermore, this chapter offers recommendations for potential avenues of further research, highlighting areas that can contribute to the ongoing advancement of the field.

Chapter 2

Literature Review

DE-actuated soft robots encompass various research phases, including design and fabrication, modeling, analysis of system behaviors, controller design, and closed-loop system performance testing. This dissertation's research will specifically concentrate on the aspects of modeling and control.

2.1 Modeling of DEAs

The dynamics exhibited by soft robotic systems diverge from those observed in traditional rigid-bodied robots. When comprised of a series of dielectric elastomer (DE) actuation elements, these robots manifest behavior resembling a continuous continuum. In theoretical terms, the ultimate configuration of the robot can be elucidated through a continuous function, demanding the application of continuous mathematical principles for its modeling. Given that the attributes of soft robots deviate from those of conventional rigid linkage-based systems, researchers have devised novel static, dynamic, and kinematic models to encapsulate their capacity for bending and flexing [22].

Robots entirely fashioned from DEs currently lack well-established models or planning and control algorithms. This predicament chiefly stems from their inherent deformations, which are characterized by continuity, intricacy, and pronounced compliance. Consequently, a pivotal stride in advancing the field pertains to the formulation of control-centric models and analyses concerning DE actuators [23–25].

Early approaches to dynamic modeling of Dielectric Elastomer Actuators (DEAs) utilized linear-elasticity and free boundary approximations to yield reasonable predictions of DEA behavior within the regime of small strains (less than 10%) [20; 26]. However, in response to the limitations imposed by small strains

and linear elasticity, nonlinear models emerged, grounded in hyper-elasticity frameworks [27–29], and tailored to encapsulate DEA behavior [30; 31]. A more sophisticated characterization of DEA responses was derived from the perspective of thermodynamics in the work of Suo et al. [32]. This contribution furnished a model proficient in accurately predicting substantial deformations. Consequently, a repertoire of foundational models was developed to facilitate both linear and nonlinear dynamic analysis of DEAs. While these first-principle models significantly propelled DEA advancement, they frequently lack suitability for control-focused analysis and design due to their inherent complexity, encompassing numerous terms and parameters.

Moreover, DEAs frequently manifest time-varying traits, a facet inadequately addressed by many current models or restricted to simplified assumptions regarding time-dependent phenomena [31]. A noteworthy gap exists in the present methodology concerning DEA modeling within the context of control-oriented tasks. Hence, the development of modeling approaches meticulously tailored to control-focused objectives is imperative.

So far, the main approaches in models for Dielectric Elastomer Actuators (DEAs) has been developed by material scientists, who have primarily employed mechanistic principles as the foundational basis for their modeling. The mechanism modeling method undertakes a comprehensive analysis of the deformation mechanisms inherent in Dielectric Elastomer Actuators (DEAs) by leveraging fundamental principles and the laws of physics. Through rigorous mathematical derivation, a dynamic model, which encapsulates their motion characteristics, is formulated. Currently, two primary methodologies stand at the forefront of DEA dynamics modeling: the modeling approach grounded in the principles of virtual work and the modeling technique rooted in the Euler-Lagrange equation.

Employing the modeling methodology predicated on the virtual work principle, Suo [32] meticulously formulated a comprehensive dynamics model framework for Dielectric Elastomer Actuators (DEAs), firmly grounded in the principles of continuum mechanics and thermodynamics. Central to this framework is the articulation of the free energy density inherent in DE materials, for which a spectrum of hyperelastic material models, including but not limited to the Neo-Hookean model [33], the Gent model [34], and the Ogden model [28], has been aptly employed. Expanding on this foundational work, Zhu et al. [35] advanced the field by crafting a kinetic model tailored to spherical DEAs, leveraging the virtual work principle as their analytical cornerstone, while simultaneously conducting a comprehensive analysis of

their dynamic performance. In a parallel endeavor, Xiao et al. [36] extended this modeling paradigm to encompass planar DEAs, once again rooted in the virtual work principle. Furthermore, Gupta et al. [37] undertook an exhaustive examination of the stresses inherent in planar antagonistic DEAs and proceeded to establish a dynamic model firmly anchored in the virtual work principle. Concurrently, Gu et al. [38] introduced a generalized Maxwell model to capture the intricate viscoelastic behavior exhibited by DE materials. This pioneering approach underpinned the development of a dynamic DEA model, aligning with the virtual work principle. Notably, Gu et al. [38] extended their efforts by employing the generalized Maxwell model to forge a kinetic model for DEAs. This kinetic model was specifically designed to provide a quantitative elucidation of the motion characteristics exhibited by DEAs when subjected to cyclic driving voltage.

In the modeling approach for Dielectric Elastomer Actuator (DEA) dynamics founded upon the Euler-Lagrange equation, it is essential to note that the potential energy incorporated into the Lagrange equation deviates from conventional interpretations. Instead, it encompasses the integral of the system's free energy density function over its volumetric domain, encompassing elements such as Helmholtz's free energy and potential energy. Xu et al. [39] notably advanced this modeling paradigm by formulating a dynamic model for planar DEAs grounded in the Euler-Lagrange equation. Their diligent work encompassed a thorough investigation into the dynamic response exhibited by DEAs under varying loads through computational simulations. Simultaneously, Sheng et al. [40] contributed significantly by developing a kinetic model specific to planar DEAs, also hinging on the Euler-Lagrange equation. Through meticulous simulations, they provided valuable insights into the pronounced temperature and frequency dependencies characterizing the dynamic response of DEAs. Further enriching the field, Joglekar [41] leveraged a diverse set of material models, including the Neo-Hookean, Mooney-Rivlin, and Ogden models, to effectively describe the free energy density inherent in DE materials. Subsequently, Joglekar established a dynamic model for planar DEAs, rooted in the Euler-Lagrange equations. This endeavor was complemented by a comprehensive investigation into the dynamic performance of DEAs, facilitated by numerical simulations.

Upon scrutinizing the dynamics of the Dielectric Elastomer Actuator (DEA) mechanisms as modeled in the aforementioned studies, a noteworthy commonality emerges—they uniformly exhibit quadratic input characteristics. This shared trait can be attributed to the conceptualization of the DEA as a variable capacitor denoted

as C, where the voltage V_C across this capacitor equates to the driving voltage V, i.e., $V_C = V$. Furthermore, considering that the principal factor driving DEA deformation is the Maxwell stress denoted as σ which is computed as explicated in Eq. (2.1) in [21], it becomes apparent that the dynamical models developed in the cited literature inherently entail a quadratic input term in the form of V^2. It is worth highlighting that systems characterized by quadratic inputs present theoretical challenges with regard to control. This inherent characteristic introduces a novel dimension of complexity when it comes to both modeling and controlling DEAs. Consequently, it underscores the necessity for innovative control strategies and modeling paradigms to effectively grapple with these intricacies.

$$\sigma = \varepsilon\varepsilon_0 E^2 = \varepsilon\varepsilon_0 (\frac{V_C}{d})^2 \tag{2.1}$$

where $\varepsilon_0, \varepsilon, E$ and d are vacuum dielectric constant, the dielectric constant of the DE material, the electric field strength and the thickness of the DE film, respectively.

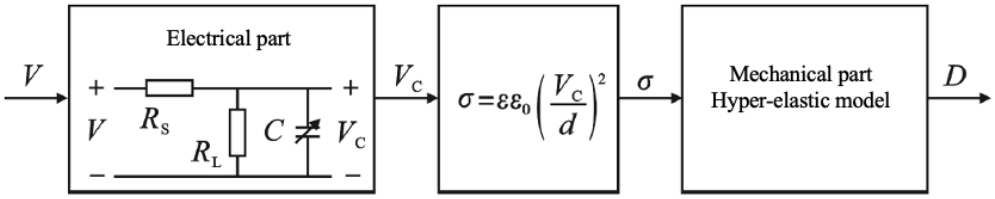

Figure 2.1: Structure of mechanics based models

In Fig. 2.1, the electrical model is a kinetic equation that describes the response of the capacitor voltage V_C to the driving voltage V in a circuit consisting of R_S, R_L and C. Its input V is the input of the DEA kinetic model, while the mechanical model describes the stress-strain relationship of the DEA with the help of a hyperelastic material model. The mechanical model describes the stress-strain relationship of the DEA with the help of a hyperelastic material model. The two are coupled to each other by means of the Maxwell stress σ, so that the input of the mechanical model has the quadratic term variable V_C^2 . Therefore, DEA is a class of coupled electromechanical nonlinear systems where mechanical model has quadratic inputs. Based on this modeling framework, [3] established the electrical model of DEA using R_S, R_L and C, used the generalized Kelvin-Voigt model as the mechanical model, and coupled the electrical model and mechanical model with each other using Maxwell stress σ to establish the dynamics model of DEA.

In light of the ongoing exploratory nature of research pertaining to the physical mechanism underlying Dielectric Elastomer Actuator (DEA) electrodeformation, it is evident that the current theoretical analyses remain insufficient in providing a comprehensive elucidation of its intricate kinematic properties. This inherent complexity presents formidable challenges when attempting to formulate dynamic models for DEA systems. Furthermore, addressing the control aspects of a specific subset of electromechanically coupled nonlinear systems, characterized by the absence of quadratic inputs in the electrical model and quadratic inputs in the mechanical model, presents an enduring and intricate challenge, as highlighted in prior research [42]. This represents a significant theoretical impediment in the pursuit of achieving precise motion control objectives within the realm of DEA technology.

2.2 Control of DEAs

In contrast to the control of rigid bodies, characterized by their movements describable by a finite number of degrees of freedom, the motions of soft bodies evade confinement to mere planar trajectories. Elastic soft materials are endowed with a spectrum of deformations encompassing bending, twisting, stretching, compressing, buckling, wrinkling, and more. This array of motion can be conceptualized as presenting an unbounded multitude of degrees of freedom, which considerably amplifies the intricacies associated with controlling soft robots. Effective control of soft robots necessitates novel paradigms in modeling, control strategies, dynamic analysis, and high-level planning. While considerable progress has been made in design and modeling endeavors, the realm of control for Dielectric Elastomer Actuators (DEAs) and DEA-driven robots remains relatively unexplored. Despite certain attempts to control DEAs through adaptive [3; 23; 25] or feedback [43] techniques, these approaches generally disregard nonlinear material behavior, viscoelasticity, and hysteretic effects during their formulation. Consequently, their efficacy is often confined to situations involving modest displacements or limited control durations.

The formidable control challenge intrinsic to soft robots employing DEAs can largely be attributed to the profound nonlinearities stemming from substantial deformations within the system, notably hysteresis and viscoelasticity.

Hysteresis nonlinearity holds a pervasive presence in oscillatory phenomena observed in experimental tests of DEAs. For decades, hysteresis nonlinearity has posed a formidable quandary for control design engineers. Traditional control techniques, founded upon Laplace domain and state space control methodologies, were

originally devised for differentiable linear or nonlinear systems. A common approach involves formulating an inverse representation to counteract the effects of hysteresis, a pioneering notion attributed to Tao and Kokotovic [44]. Recent advancements in this approach are discussed in references such as [45]. However, due to the intricate and uncertain nature of hysteresis, constructing its inverse description remains a challenging endeavor. Additionally, this cancellation process introduces compensation errors, potentially jeopardizing stability analysis for closed-loop systems, except for specific scenarios [44].

The dynamics modeling of Dielectric Elastomer Actuators (DEA) remains a nascent field, and achieving precise motion control objectives within this context remains a vexing challenge. Notably, DEA constitutes an electromechanical coupled nonlinear system that lacks quadratic inputs within its electrical model but possesses quadratic inputs within its mechanical model. This unique attribute renders the control problem exceptionally intricate and unresolved. Many extant control strategies are formulated without dedicated attention to the quadratic term variables within the DEA mechanical model, classifiable into two overarching categories: model free control strategies, model-based control strategies.

2.2.1 Model Free Control Strategy

Instead of modeling the dynamics of DEA, the model-independent control strategy designs a model-independent feedback controller and adjusts the parameters of the controller through experiments to directly eliminate the deviation between the output signal and the given signal of the system. Therefore, the model-independent feedback control strategy has certain advantages in the practical application of DEA.

The traditional PID feedback control strategy is a typical model-independent feedback control strategy, which has the advantages of simple structure and easy realization, and has been widely used in engineering practice. Although the traditional PID feedback control strategy can be used to realize the motion control objective of DEA, the complex motion characteristics (especially the hysteresis nonlinear characteristics) of DEA cannot be effectively dealt with by using only the PID control strategy, which leads to poor control effect[46; 47]. Researchers have also explored the application of other model-free control strategies in the motion control of DEA. Druitt et al. [48]used a model-independent neural network-fuzzy controller to realize the motion control of DEA. Li et al. [49] proposed a model-free control strategy based on a deep reinforcement learning framework for the motion control of

DEA, and realized its motion control objectives. agent-based sliding mode control strategy to achieve the motion control objective of DEA.

In the model-independent feedback control strategy, the controller parameters often need to be calibrated in real experiments. In order to solve the problem of difficult parameter adjustment in practical applications, Huang et al. [47] designed a model-independent nonlinear PID controller; then, the dynamics model of DEA was used as the control object, and the controller parameters were coarsely adjusted through simulation; finally, the controller parameters were finely adjusted in experiments. Then, using the dynamics model of DEA as the control object, the controller parameters are coarsely adjusted through simulation; finally, the controller parameters are finely adjusted in the experiment to realize the tracking control objective of DEA. In this study, the design of the controller is model-independent and the model is only used for initial tuning of the controller parameters in the simulation. Therefore, the above control strategy is favorable for rapid engineering applications. However, due to the small number of model-independent control frameworks currently available, the control strategy has significant limitations in terms of controller design.

2.2.2 Model Based Control Strategy

In Fig. 2.1, the mechanistic model of a Dielectric Elastomer Actuator (DEA) is delineated into two interrelated components: an electrical model characterized by the absence of quadratic inputs and a mechanical model that incorporates quadratic term variables. This particular modeling structure poses a significant challenge when addressing control problems associated with DEAs. Notably, the existing body of research in this domain is rather limited, with only a scarcity of studies delving into control strategies grounded in mechanistic models.

The prevailing mechanism-based control strategies within the realm of Dielectric Elastomer Actuators (DEAs) have primarily been tailored to the dynamics model characterized by quadratic inputs, with a notable omission of consideration for the electrical model as depicted in the framework illustrated in Fig. 6. In such approaches, the DEA is often simplistically treated as a variable capacitor. Notably, Gupta et al. [37] and Gu et al. [50] have advanced mechanism-based dynamics models specifically designed for planar antagonistic DEAs. In these works, an analytical inverse of the comprehensive dynamics model is formulated by removing the square root term, effectively rendering it a feed-forward inverse compensation controller. This analytical inverse expression is subsequently employed to facilitate

the attainment of tracking control objectives for the DEA. Similarly, Rizzello et al. [51] have established a mechanical dynamics model for conical DEAs grounded in mechanical dynamics principles. To address the quadratic inputs inherent in the model, a square root module is introduced for compensation. Furthermore, a series of robust Proportional-Integral-Derivative (PID) feedback controllers are designed, each corresponding to an equilibrium point in the approximate linear model of the DEA dynamics. These controllers are then cascaded with the square root module to realize precise position control targets for the DEA. It is noteworthy that, within the context of the electrical model encompassed by the modeling framework presented in Fig. 2.1, research pertaining to control strategies grounded in mechanistic models remains comparatively limited.

The aforementioned studies have indeed embarked upon an initial exploration of mechanistic model-based control strategies for Dielectric Elastomer Actuators (DEAs). Nevertheless, it is essential to acknowledge that the intrinsic complexity of the mechanistic dynamics model governing DEAs has led these investigations to adopt a relatively simplistic approach, namely, the utilization of a square-root module for the purpose of mitigating the quadratic term variables. A notable gap in these studies pertains to the limited attention paid to stability analysis within the context of the control system. Consequently, a comprehensive investigation into the stability aspects of these mechanistic model-based control strategies remains a crucial avenue for future research and development in the field of DEA control methodologies.

Chapter 3

Physics Based Modeling for Dielectric Elastomer Actuators

3.1 Introduction

In this chapter, guided by fundamental principles of physics, two distinct dynamic models will be formulated—one tailored to conical Dielectric Elastomer Actuators (DEAs) and the other specifically designed for planar DEAs. In tandem, methods pertinent to the identification of relevant parameters will be expounded. The efficacy of these models will be substantiated through empirical validation using experimental findings.

3.2 Physics Based modeling for Dielectric Elastomer Actuators with Conical Shape

3.2.1 Model Development

In this section, we outline the formulation of a dynamic model tailored for a conically shaped Dielectric Elastomer Actuator (DEA). To enhance clarity, we define three distinct states of the DEA a priori, namely the "undeformed state," the "pre-stretched state," and the "electro-deformed state." Visual depictions of these states are provided in Figure 3.1. The detailed characteristics of each state are expounded upon in the following subsections:

(A) Undeformed State:

In the initial undeformed state, a Dielectric Elastomer (DE) membrane possessing

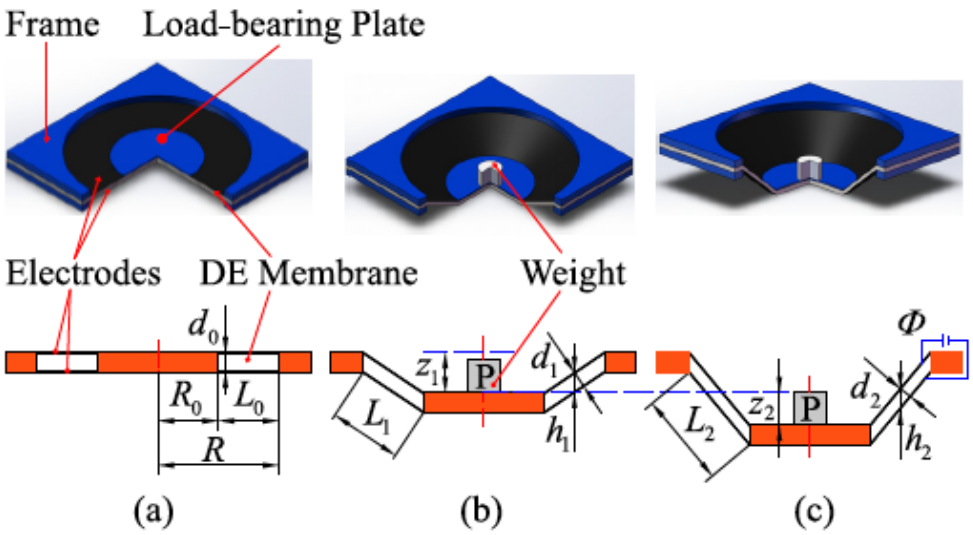

Figure 3.1: States of the DEA. (a) Undeformed state, (b) Pre-stretched state, and (c) Electro-deformed state.

a thickness denoted as d_0 is securely clamped within a frame featuring an inner circular radius of R. Positioned at the geometric center of the DE membrane is a load-bearing plate with a distinct radius of R_0. The two annular regions flanking the DE membrane are coated with compliant electrodes, yielding a radial extent for the Dielectric Elastomer Actuator (DEA) denoted as $L_0 = R - R_0$.

(B) Pre-stretched State:

Transitioning to the pre-stretched state, a mass m is centrally placed upon the load-bearing plate. Under the influence of gravitational force P, this mass descends by a displacement of z_1 to achieve equilibrium. Consequently, the DE membrane undergoes a pre-stretching process, adopting a conical configuration. As depicted in Figure 3.1(b), the dimensional attributes of the DEA in the pre-stretched state are designated by L_1, d_1, and h_1. Here, L_1 signifies the generatrix length, d_1 signifies the thickness, and h_1 quantifies the disparity in elevation between the upper and lower surfaces.

(C) Electro-deformed State:

Upon the application of a driving voltage F to the electrodes, the DE membrane undergoes a reduction in thickness accompanied by an expansion in surface area. This phenomenon induces the mass to undergo a downward displacement of z_2. The dimensional parameters characterizing the electro-deformed state are portrayed in Figure 3.1(c) and are denoted by L_2, d_2, and h_2. Here, L_2 represents the generatrix length, d_2 embodies the thickness, and h_2 signifies the difference in height.

The volumes associated with the Dielectric Elastomer Actuator (DEA) in its three distinct states – undeformed, pre-stretched, and electro-deformed – are expressed as follows:

$$\begin{cases} V_0 = \pi d_0 (R^2 - R_0^2) \\ V_1 = \pi h_1 (R^2 - R_0^2) \\ V_2 = \pi h_2 (R^2 - R_0^2) \end{cases} \tag{3.1}$$

To be precise, it is important to acknowledge that the deformation of the conically shaped Dielectric Elastomer Actuator (DEA) is inherently characterized by inhomogeneity, a point underscored by Zhang et al. [52]. However, for the sake of streamlining the dynamic modeling process, the incorporation of deformation inhomogeneity is intentionally excluded in the subsequent phases of development. This approach aligns with the methodology proposed by Rizzello et al. [51].

Given the DEA's inherent incompressibility, as expounded in the study by Suo et al. [32], the volume of the DEA remains invariant throughout its various states. This leads to the relationship $V_0 = V_1 = V_2$. By referencing Eq. (3.1), we can derive:

$$d_0 = h_1 = h_2 \tag{3.2}$$

In accordance with Eq. (3.2), the interrelations among z_1, z_2, d_1, and d_2 are described as follows:

$$\begin{cases} d_1 = h_1 \dfrac{L_0}{L_1} = d_0 \dfrac{L_0}{\sqrt{z_1^2 + L_0^2}} \\ d_2 = h_2 \dfrac{L_0}{L_2} = d_0 \dfrac{L_0}{\sqrt{(z_1 + z_2)^2 + L_0^2}} \end{cases} \tag{3.3}$$

The conical-shaped DEA under investigation in this paper is characterized by its generatrix, thickness, and circumferential stretches, which are utilized for concise representation of the DEA's states. In the pre-stretched state, the DEA's pre-stretches are denoted as $\lambda_{pre,L}$, $\lambda_{pre,d}$, and $\lambda_{pre,C}$, respectively. In the electro-deformed state, the stretches of the DEA are represented as λ_1, λ_2, and λ_3, respectively. As illustrated in Figure 3.1, the ensuing equations are upheld:

$$\begin{cases} \lambda_{pre,L} = \dfrac{L_1}{L_0} \\ \lambda_{pre,d} = \dfrac{d_1}{d_0} \\ \lambda_{pre,C} = \dfrac{2\pi}{2\pi} = 1 \end{cases} \tag{3.4}$$

$$\begin{cases} \lambda_1 = \dfrac{L_2}{L_0} \\ \lambda_2 = \dfrac{d_2}{d_0} \\ \lambda_3 = \dfrac{2\pi}{2\pi} = 1 \end{cases} \tag{3.5}$$

By referencing Equations (3.2) through (3.5), the subsequent equation is established:

$$\lambda_1\lambda_2\lambda_3 = \lambda_{pre,L}\lambda_{pre,d}\lambda_{pre,C} = 1 \tag{3.6}$$

The correlation between the charge Q and the voltage ϕ is given by:

$$Q = \phi C = \phi\frac{\varepsilon\pi L_2(R + R_0)}{d_2} = \frac{\varepsilon\phi\pi(R^2 - R_0^2)\lambda_1^2}{d_0} \tag{3.7}$$

where ε represents the permittivity and C signifies the capacitance of the DE material.

Utilizing Equations (3.3) to (3.6), the correlation between $\delta\lambda_1$ and δz_2 can be expressed as:

$$\frac{\delta z_2}{\delta\lambda_1} = \frac{L_2 L_0}{\sqrt{L_2^2 - L_0^2}} \tag{3.8}$$

By combining Equations (3.6) and (3.7), the alteration in charge on the electrode can be described as follows:

$$\delta Q = \frac{\varepsilon\pi(R^2 - R_0^2)}{d_0}(\lambda_1^2\delta\phi + 2\phi\delta\lambda_1) \tag{3.9}$$

To compute the work associated with the inertial forces during the electromechanical deformation, our analysis revolves around the utilization of cylindrical coordinates as illustrated in Figure 3.2. Within this context, O, r, φ, and z respectively denote the coordinate origin, the radial distance, the azimuth angle, and the height in the cylindrical coordinate system.

As depicted in Figure 3.2(b), our focus shifts to an infinitesimal element

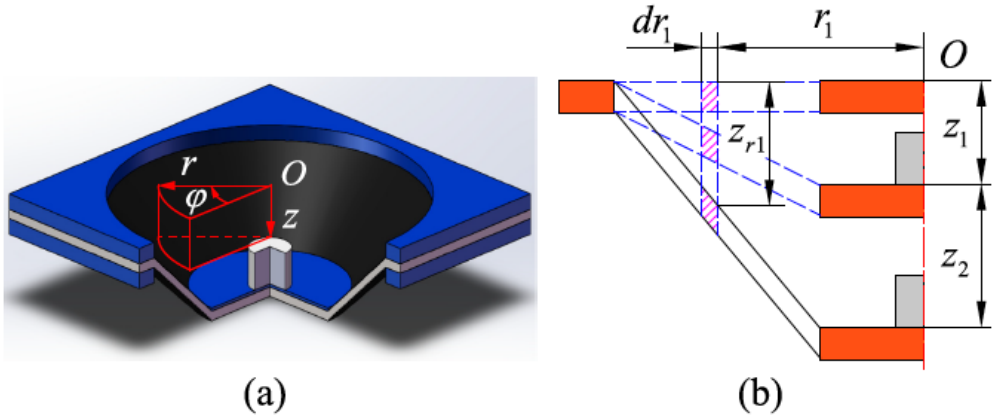

Figure 3.2: Displacement of element in cylindrical coordinates: (a) Cylindrical coordinates, and (b) Displacement of element in each state.

characterized by an inner radius of r_1 and an outer radius of $r_1 + dr_1$. In the electro-deformed state, the element's displacements along the r-direction, φ-direction, and z-direction are 0, 0, and z_{r1}, respectively. Consequently, the interrelation between z_{r1} and z_2 is expressed as:

$$z_{r1} = (z_1 + z_2)\frac{R - r_1}{R - R_0} \tag{3.10}$$

In each material element, the inertial forces are null along the r-direction and φ-direction, while along the z-direction, it is represented as dF_{r1}. By invoking D'Alembert's principle, the ensuing expression can be deduced:

$$dF_{r1} = -\rho \cdot 2\pi d_0 r_1 d_{r1} \cdot \frac{d^2 z_{r1}}{dt^2} \tag{3.11}$$

where ρ signifies the density of the DE material.

Consequently, the variations in the work accomplished by the inertial forces amount to 0, 0, and $\delta H_{I,z}$ for the r-direction, φ-direction, and z-direction, respectively. By making reference to Equations (3.10) and (3.11), the work executed by the inertial force dF_{r1} can be defined as:

$$\delta H_{I,z} = \int_{R_0}^{R} \delta z_{r1} dF_{r1} = -\frac{\rho\pi d_0 L_0 (R + 3R_0)}{6} \frac{d^2 z_2}{dt^2} \delta z_2 \tag{3.12}$$

The alteration in the free energy of the DEA corresponds to the aggregate of the work accomplished by the driving voltage, the gravitational force, and the inertial forces. This relationship can be expressed as follows:

$$\pi d_0(R^2 - R_0^2)\delta W = \phi\delta Q + P\delta z_2 + (0 + 0 + \delta H_{I,z}) \tag{3.13}$$

where W denotes the free energy density of the DEA, and δW signifies the alteration in W.

By substituting Equations (3.9) and (3.12) into Equation (3.13), the variation in the free energy density W is given by:

$$\delta W = \frac{\varepsilon\phi(\lambda_1^2\delta\phi + 2\phi\lambda_1 d\lambda_1)}{d_0^2} + \frac{P\delta z_2}{\pi d_0(R^2 - R_0^2)} - \frac{\rho(R + 3R_0)}{6R + R_0}\frac{d^2 z_2}{dt^2}\delta z_2 \tag{3.14}$$

Upon inserting Equation (3.8) into Equation (3.14), we arrive at:

$$\frac{\partial W}{\partial \lambda_1} = \frac{2\varepsilon\phi^2\lambda_1}{d_0^2} + \frac{PL_2}{\pi d_0(R + R_0)\sqrt{L_2^2 - L_0^2}} - \frac{\rho L_2 L_0(R_3 R_0)}{6(R + R_0)\sqrt{L_2^2 - L_0^2}}\frac{d^2 z_2}{dt^2} \tag{3.15}$$

where

$$\frac{d^2 z_2}{dt^2} = \frac{-L_0^4}{(L_2^2 - L_0^2)^{3/2}}(\frac{d\lambda_1}{dt})^2 + \frac{L_2 L_0}{\sqrt{L_2^2 - L_0^2}}\frac{d^2\lambda_1}{dt^2} \tag{3.16}$$

To encapsulate the viscoelastic nature of the DE material, we embrace the rheological model featuring two parallel units, depicted in Figure 3.3 [53]. In this configuration, section A comprises solely a spring α_0, while section B incorporates four parallel units. Each unit within section B is comprised of a spring α_i in conjunction with a dashpot connected in series. Within this modeling framework, we presume each dashpot to behave as a Newtonian fluid possessing a viscosity η_i. Denoting $\xi_{i,j}$ (where $j = 1, 2$) as the stretches induced by the dashpots, the stretches of the spring α_i are determined through the multiplication rules $\lambda_{i1}^e = \lambda_1/\xi_{i1}$ and $\lambda_{i_2}^e = \lambda_2/\xi_{i2}$.

The free energy density W of the DEA, as described in Suo et al.'s work [32], is formulated as follows:

$$W = W_s + \frac{D^2}{2\varepsilon} \tag{3.17}$$

where W_s signifies the Helmholtz free energy attributed to the elastomer's stretching, while D represents the electric displacement. The electric displacement D can be defined as:

$$D = \frac{Q}{\pi L_2(R + R_0)} \tag{3.18}$$

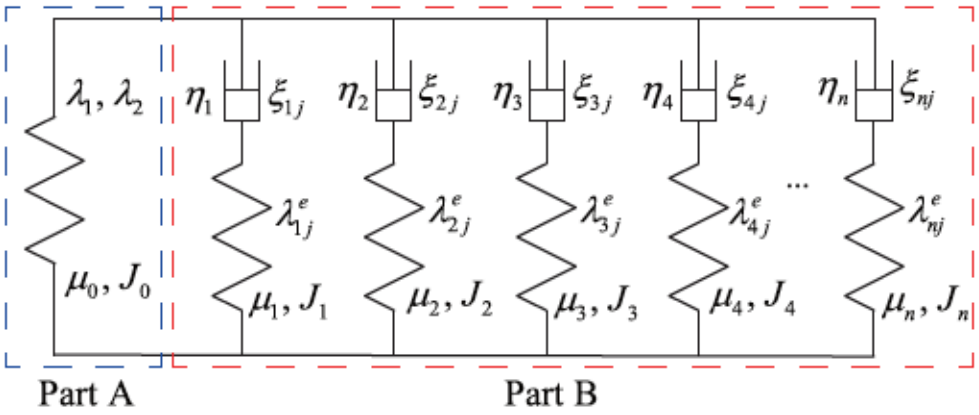

Figure 3.3: Rheological Model: Part A exclusively comprises a spring, whereas each unit in Part B is composed of a spring in conjunction with a series-wound dashpot.

In this section, we opt to employ the Gent model [53] to characterize the elastic energy density of the DEA. As such, the elastic energy density of the DEA is expressed as follows:

$$\begin{aligned} W_s = &\sum_{i=0}^{n} W_{ela}^{\alpha_i} = -\frac{\mu_0 J_0}{2} ln(1 - \frac{\lambda_1^2 + \lambda_2^2 + \lambda_1^{-2}\lambda_2^{-2} - 3}{J_0}) \\ &- \sum_{i=1}^{n} \frac{\mu_i J_i}{2} ln(1 - \frac{\lambda_1^2 \xi_{i1}^{-} 2 + \lambda_2^2 \xi_{i2}^{-} 2 + \lambda_1^{-2}\lambda_2^{-2} \xi i1^2 \xi i2^2 - 3}{J_i}) \end{aligned} \tag{3.19}$$

where $W_{ela}^{\alpha_i}$ represents the elastic energy densities associated with the spring α_i. The parameters μ_i correspond to the shear moduli of the spring α_i, while J_i denote the deformation limits of the same spring α_i.

By utilizing Equations (3.5) through (3.7), as well as Equations (3.17) to (3.19), the free energy density of the DEA can be expressed as:

$$\begin{aligned} W = &\frac{\varepsilon \phi^2 \lambda_1^2}{2 d_0^2} + \frac{\mu_0 J_0}{2} ln(1 - \frac{\lambda_1^2 + \lambda_1^{-2} - 2}{J_0}) \\ &- \sum_{i=1}^{n} \frac{\mu_i J_i}{2} ln(1 - \frac{\lambda_1^2 \xi_{i1}^{-2} \lambda_1^{-2} \xi_{i2}^2 + \xi_{i1}^2 \xi_{i2}^2 - 3}{J_i}) \end{aligned} \tag{3.20}$$

In accordance with Newton's third law of motion, the stresses present in the spring α_i (where $i = 1, 2, 3, \ldots, n$) are identical to the corresponding stresses in the dashpot. As a result, the following relationship holds:

$$-\xi_{ij}\frac{\partial Wela}{\partial \xi_{ij}} = \eta_i \frac{d\xi_{ij}}{dt} \ (i = 1, 2, 3, 4, \cdots, n; j = 1, 2) \tag{3.21}$$

By combining Equations (3.19) and (3.21), the strain rates attributed to the dashpots can be formulated as:

$$\begin{cases} \dfrac{\xi_{i1}}{dt} = \dfrac{\mu_i}{\eta_i} - \dfrac{-\lambda_1^2\xi_{i1}^{-2} + \xi_{i1}^2\xi_{i2}^2}{1 - \frac{\lambda_1^2\xi_{i1}^{-2}\lambda_1^{-2}\xi_{i2}^{-2} + \xi_{i1}^2\xi_{i2}^2 - 3}{J_i}} \\ \dfrac{\xi_{i2}}{dt} = \dfrac{\mu_i}{\eta_i} - \dfrac{-\lambda_1^2\xi_{i2}^{-2} + \xi_{i1}^2\xi_{i2}^2}{1 - \frac{\lambda_1^2\xi_{i1}^{-2}\lambda_1^{-2}\xi_{i2}^{-2} + \xi_{i1}^2\xi_{i2}^2 - 3}{J_i}} \end{cases} \tag{3.22}$$

The viscoelastic relaxation time T_i of the DEA is defined as the quotient of η_i divided by μ_i, where $i = 1, 2, \ldots, n$. Consequently, the relationship is given by:

$$T_i = \frac{\eta_i}{\mu_i} \tag{3.23}$$

Upon substituting Equation (3.20) into Equation (3.15), and subsequently amalgamating the outcome with Equation (3.22), the dynamic model delineating the behavior of the conical DEA can be elucidated as follows:

$$\begin{cases} \dfrac{\rho\lambda_1^2 L_0^2(R+3R_0)}{6(R+R_0)(\lambda_1^2-1)}\dfrac{d^2\lambda_1}{dt^2} = \dfrac{\rho\lambda_1^2 L_0^2(R+3R_0)}{6(R+R_0)(\lambda_1^2-1)}(\dfrac{d\lambda_1}{dt})^2 + \dfrac{P\lambda_1}{\pi d(R+R_0)\sqrt{\lambda_1^2-1}} \\ \quad + \dfrac{\varepsilon\phi^2\lambda_1}{d_0^2} + \mu_0\dfrac{\lambda_1 - \lambda_1^{-3}}{1 - \frac{\lambda_1^2+\lambda_2^{-2}-2}{J_)}} - \sum_{i=1}^{n}\mu_i\dfrac{\lambda_1\xi_{i1}^{-2} - \lambda_1^{-3}\xi_{i1}^{-2}}{1 - \frac{\lambda_1^2\xi_{i1}^{-2}+\lambda_1^{-2}\xi_{i2}^{-2}+\xi i1^2\xi_{i2}^2-3}{J_i}} \\ \dfrac{d\xi_{i1}}{dt} = -\dfrac{\mu_i}{\eta_i}\dfrac{-\lambda_1^2\xi_{i1}^{-2} + \xi_{i1}^2\xi_{i2}^2}{1 - \frac{\lambda_1^2\xi_{i1}^{-2}+\lambda_1^{-2}\xi_{i2}^{-2}+\xi i1^2\xi_{i2}^2-3}{J_i}} \\ \dfrac{d\xi_{i2}}{dt} = -\dfrac{\mu_i}{\eta_i}\dfrac{-\lambda_1^2\xi_{i2}^{-2} + \xi_{i1}^2\xi_{i2}^2}{1 - \frac{\lambda_1^2\xi_{i1}^{-2}+\lambda_1^{-2}\xi_{i2}^{-2}+\xi i1^2\xi_{i2}^2-3}{J_i}} \quad (i = 1, 2, 3, \cdots, n) \end{cases} \tag{3.24}$$

Up to this point, we have formulated a dynamic model that comprehensively accounts for the inherent nonlinearity, intricate electromechanical interplay, and time-evolving viscoelastic characteristics of the conical DEA. In the subsequent phases of our study, we undertake experimental procedures to procure empirical data pertinent to the conical DEA. Subsequently, we employ the differential evolution algorithm to ascertain the values of the yet-to-be-determined parameters in Equation (3.24), leveraging the acquired experimental data as a foundation for parameter

identification.

3.2.2 Actuation Voltages

To ascertain the parameters inherent in the elaborated model, our initial step involves introducing the applied driving voltage within the experimental setup. Subsequently, we proceed to identify the undetermined parameters by leveraging the differential evolution algorithm. Given considerations for precision and hardware limitations, we opt to employ four spring-dashpot units within the dynamic model represented by Equation (3.24), as an apt representation for characterizing the viscoelastic nature of the DEA.

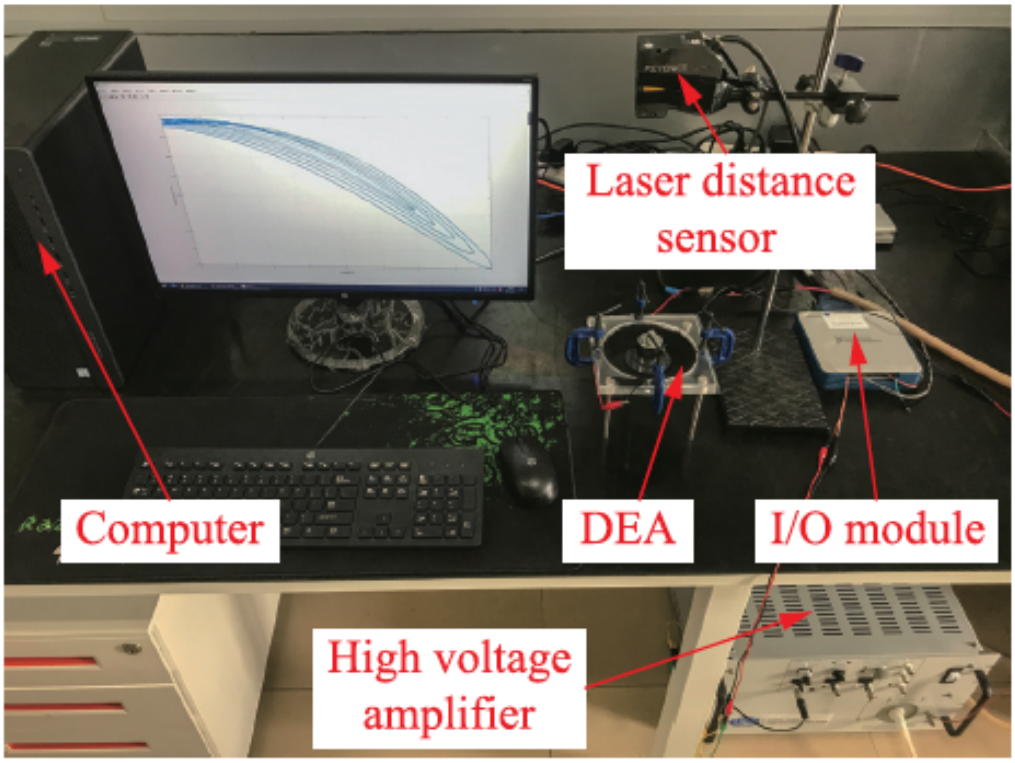

Figure 3.4: Picture of experimental platform, which mainly includes computer, high voltage amplifier, laser distance sensor, I/O module and conical DEA.

In order to facilitate the acquisition of experimental data, we implement the application of a multi-amplitude, multi-frequency driving voltage as outlined below:

$$
\begin{cases}
t_m = rem(t, \sum_{1}^{5} \frac{1}{f_i}) & \\
v(t_m) = a_1 sin(f_1 \pi t_m), & 0 \le t_m \le 1/f_1 \\
v(t_m) = a_2 sin(f_2 \pi t_m - f_2 \pi / f_1), & f_1 \le t_m \le \sum_{1}^{2} 1/f_i \\
v(t_m) = a_3 sin(f_3 \pi t_m - f_3 \pi \sum_{1}^{2} 1/f_i), & \sum_{1}^{2} 1/f_i \le t_m \le \sum_{1}^{3} 1/f_i \\
v(t_m) = a_4 sin(f_4 \pi t_m - f_4 \pi \sum_{1}^{3} 1/f_i), & \sum_{1}^{3} 1/f_i \le t_m \le \sum_{1}^{4} 1/f_i \\
v(t_m) = a_5 sin(f_5 \pi t_m - f_5 \pi \sum_{1}^{4} 1/f_i), & \sum_{1}^{4} 1/f_i \le t_m \le \sum_{1}^{5} 1/f_i
\end{cases}
\tag{3.25}
$$

The given equation represents the multi-amplitude, multi-frequency driving voltage, with the following definitions: a_i represents the amplitude, f_i signifies the frequency, t denotes the time, and $rem(\alpha/\beta)$ indicates the remainder of α divided by β. By introducing the variable $t_m = rem(t, \sum_1^5 \frac{1}{f_i})$, we are able to generate the periodic driving voltage within the time interval $t \in [0, +\infty)$. By configuring various values of a_i and f_i, we can produce driving voltages characterized by diverse amplitudes and frequencies over a single period.

3.2.3 Parameters Identification

In the pre-stretched state, the vertical displacement of the weight is recorded as $z_1 = 1.26, \text{cm}$. The experimental sampling period is defined as $T = 0.01, \text{s}$. When the parameters are set to $a_i = 5.5 + 0.5i$ kV, (for $i = 1, 2, \ldots, 5$) and $f_i = 0.2i$ Hz, the graph illustrating the driving voltage is presented in Figure 3.5. To circumvent the occurrence of negative weight displacements, the maximum frequency of the driving voltage is constrained to 1.0 Hz in all conducted experiments [54].

The Differential Evolution algorithm employed for parameters identification is concisely outlined in Figure 3.6. Given our lack of prior knowledge regarding the values of J_i, μ_i, and T_i, we opt to establish sufficiently broad search ranges to ensure the efficacy of the differential evolution algorithm in locating the optimal solution. Accordingly, the search range for J_i is defined as $(0, 9 \times 10^8]$, the search range for μ_i is established as $(0, 8 \times 10^6]$, and the search range for T_i is designated as $(0, 3 \times 10^6]$.

To conveniently assess the predictive capabilities of the model, we introduce two

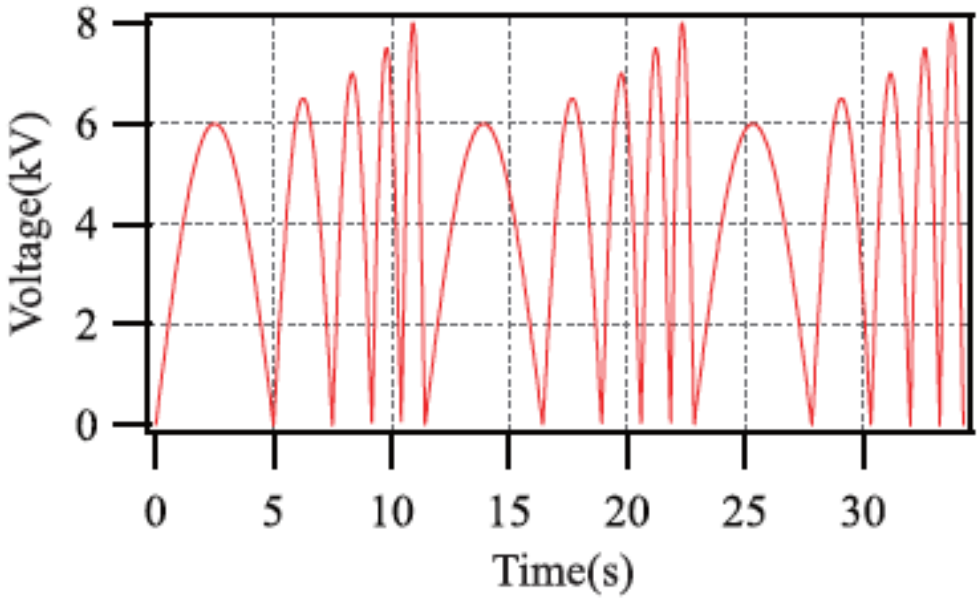

Figure 3.5: Diagram of driving voltage applied in parameters identification.

performance metrics: the root-mean-square error (e_{rms}) and the maximum tracking error (e_m).

$$\begin{cases} e_{rms} = \sqrt{\dfrac{1}{n}\sum_{i=1}^{n}(z_{ei} - z_{mi})^2} \times 100\% \\ e_m = \dfrac{max(|z_{ei} - z_{mi}|)}{max(z_{ei}) - max(z_{mi})} \times 100\% \end{cases} \tag{3.26}$$

Here, z_{ei} and z_{mi} respectively denote the experimental data and the model-predicted values of the vertical displacement. The variable n represents the number of samples within the sampling time.

Figure 3.7 provides a visual comparison between the model predictions and the experimental results. The discrepancy between the model predictions and the experimental outcomes, i.e., $z_e - z_m$, is depicted in Figure 3.8. Table 1 presents the identified parameters obtained for the dynamic model defined in Equation (3.24). The root-mean-square error (e_{rms}) is calculated as 0.69%, while the maximum tracking error (e_m) amounts to 1.60%.

3.2.4 Model Validation

The input to the dynamic model described by Equation (3.24) is the voltage outlined in Equation (3.25). By varying the values of a_i and f_i, the current section aims to

Algorithm: *Model Evolution*

Input: *Input voltage signal, material and geometrocal parameters*

Output: *Prediction of time-dependent electromechanical response of the actuator*

begin
  Input the parameters of the spring μ_i, J_i *(where i=0,1,...,n) and the relaxation time of the dashpots* T_j *(where j=1,2,...,n)*
  Input the dielectric permitivity ε *of the material*
  Input the geometrical parameters R, R_0, d_0, z_1
  Input the voltage signal **(25)**
  Initialize the variables $\lambda_1, \xi_{j1}, \xi_{j2}$
  Call the **ode15s** *function for the specified time interval* t
    Get the voltage value ϕ_l *at time instant* t_l
    Calculate $d\lambda_1/dt, d^2\lambda_2/dt^2, d\xi_{j1}/dt, d\xi_{j2}/dt$ *for given* ϕ_l *using system of equation* **(24)**
    Integration to find $\lambda_1(t), \xi_{j1}(t)$ *and* $\xi_{j2}(t)$
end
end

Figure 3.6: Differential Evolution algorithm used for identification

Table 3.1: Parameters of the conical DEA model.

i	$\mu_i(kPa)$	J_i	$T_i = \eta_i/\mu_i$
i=0	0.1	6.8×10^7	–
i=1	5277.4	79.9×10^7	0.01
i=2	0.1	80.1×10^7	3945.71
i=3	33.1	7.9×10^7	9.82
i=4	571.2	3.7×10^7	8484.73

assess the generalization capability of the proposed dynamic model for the conical DEA.

Model validation with different driving voltage amplitudes

The amplitudes of the driving voltage are defined as $a_i = 5.5 + 0.5i$ kV, for $i = 1, 2, \ldots, 5$. Additionally, the frequencies are established as $f_i = 0.2, 0.4, 0.6, 0.8, 1.0$ Hz correspondingly. Consequently, each test experiment utilizes a driving voltage characterized by varying amplitudes while maintaining a single frequency.

By applying the driving voltage with a single frequency and multiple amplitudes,

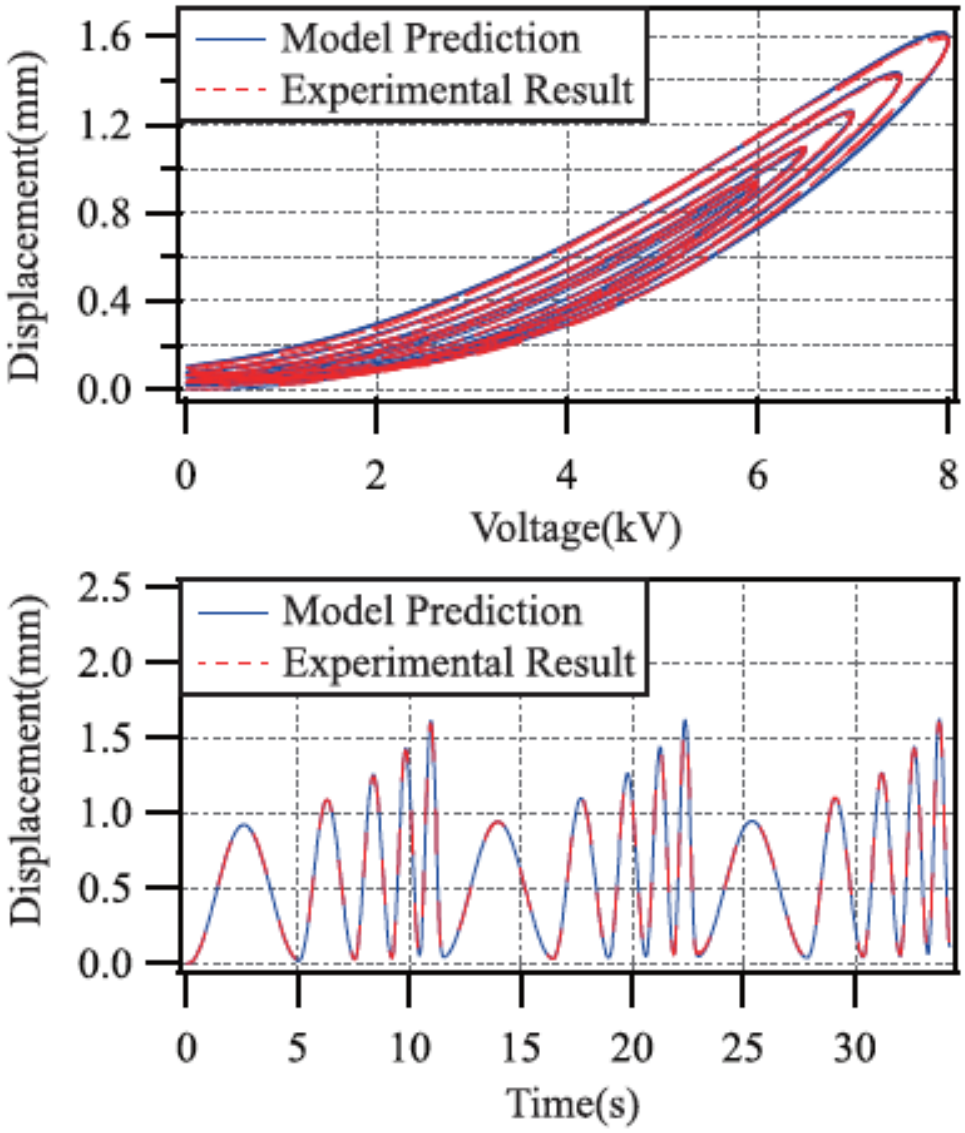

Figure 3.7: Comparison of model prediction and experimental result with different driving voltage amplitudes and different frequencies.

the comparative analysis between the model predictions and the experimental results for each individual test experiment is presented in Figures 3.9 to 3.13. The modeling error associated with each test experiment is summarized in Table 3.2.

Based on the outcomes detailed above, it is evident that the root-mean-square error of the modeling for each test experiment remains below 3%, and the maximum modeling error for any given test experiment is less than 6%. Consequently, it can be deduced that the proposed dynamic model for the DEA exhibits a commendable level of generalization capability.

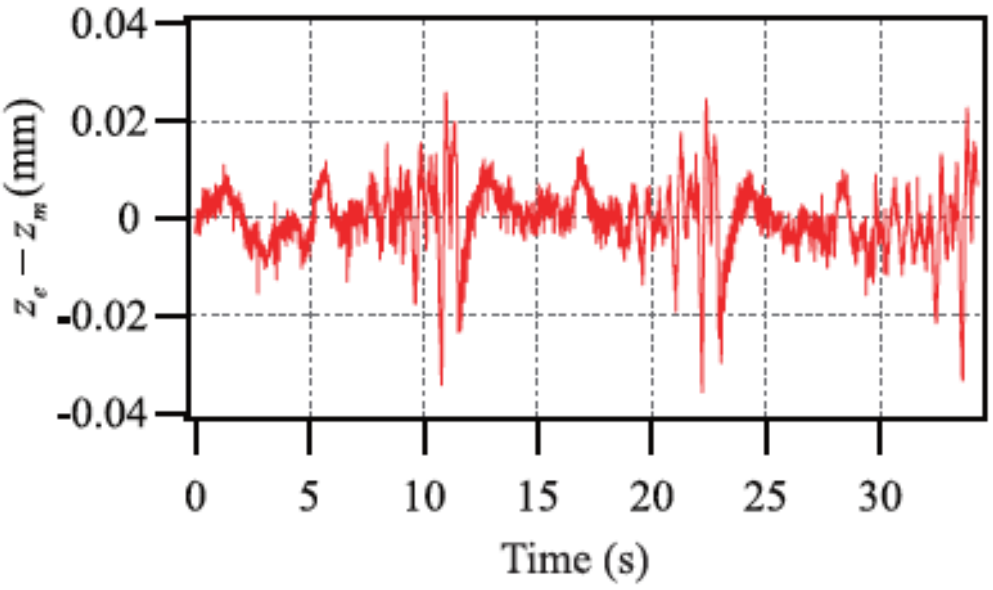

Figure 3.8: Error between model prediction and experimental result.

Table 3.2: Errors of model validation with different driving voltage amplitudes.

i	e_{rms}	e_m
f=0.2	1.7734	5.4161
f=0.4	1.6875	4.1992
f=0.6	1.7013	4.3098
f=0.8	1.3202	3.6769
f=1.0	1.2557	2.6517

Model validation with different driving voltage frequencies

The amplitudes of the driving voltage are configured as $a_i = 6.0, 6.5, 7.0, 7.5, 8.0, \text{kV}$ for $i = 1, 2, \ldots, 5$. Concurrently, the frequencies are defined as $f_i = 0.2i, \text{Hz}$ for $i = 1, 2, \ldots, 5$. Consequently, each test experiment employs a driving voltage characterized by varying frequencies while maintaining a single amplitude.

By applying the driving voltage with a single amplitude and multiple frequencies, the comparative evaluation between the model predictions and the experimental results for each individual test experiment is presented in Figures 3.14 to 3.18. The modeling error associated with each test experiment is summarized in Table 3.3.

Based on the results presented above, it is evident that the root-mean-square error of the modeling for each test experiment remains below 2%, and the maximum modeling error for any given test experiment is less than 3%. These outcomes reaffirm the exceptional performance of the developed dynamic model in terms of

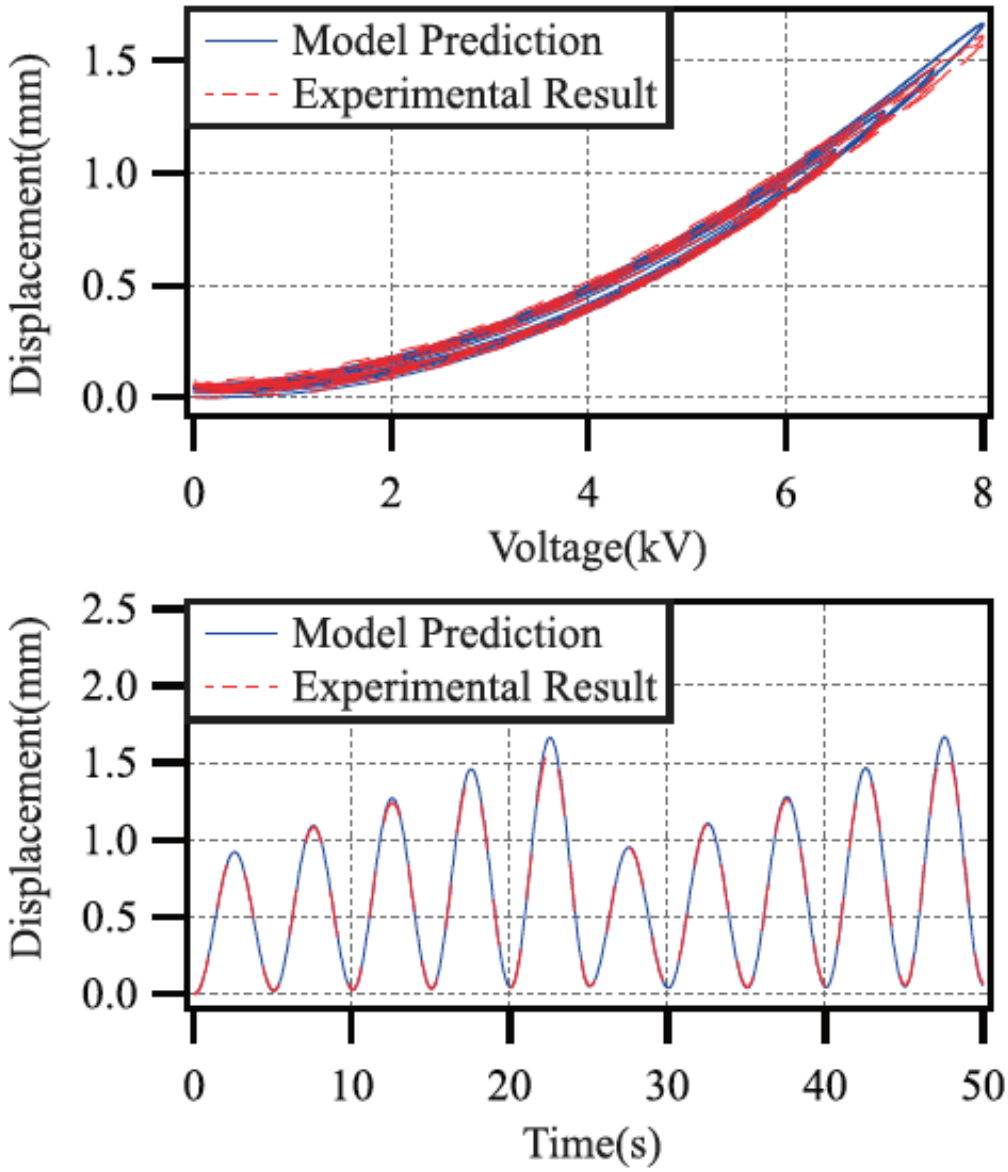

Figure 3.9: Comparisons of model prediction and experimental result with driving voltage frequency $0.2Hz$

its generalization ability.

Model validation corresponding to force analysis

To provide a more comprehensive validation of the proposed model, tests evaluating the force-versus-displacement and force-versus-voltage dynamic responses are conducted. The chosen amplitudes and frequencies of the driving voltage are defined as $a_i = 5.5{+}0.5i$ kV and $f_i = 0.2i$ Hz, respectively. In this verification process,

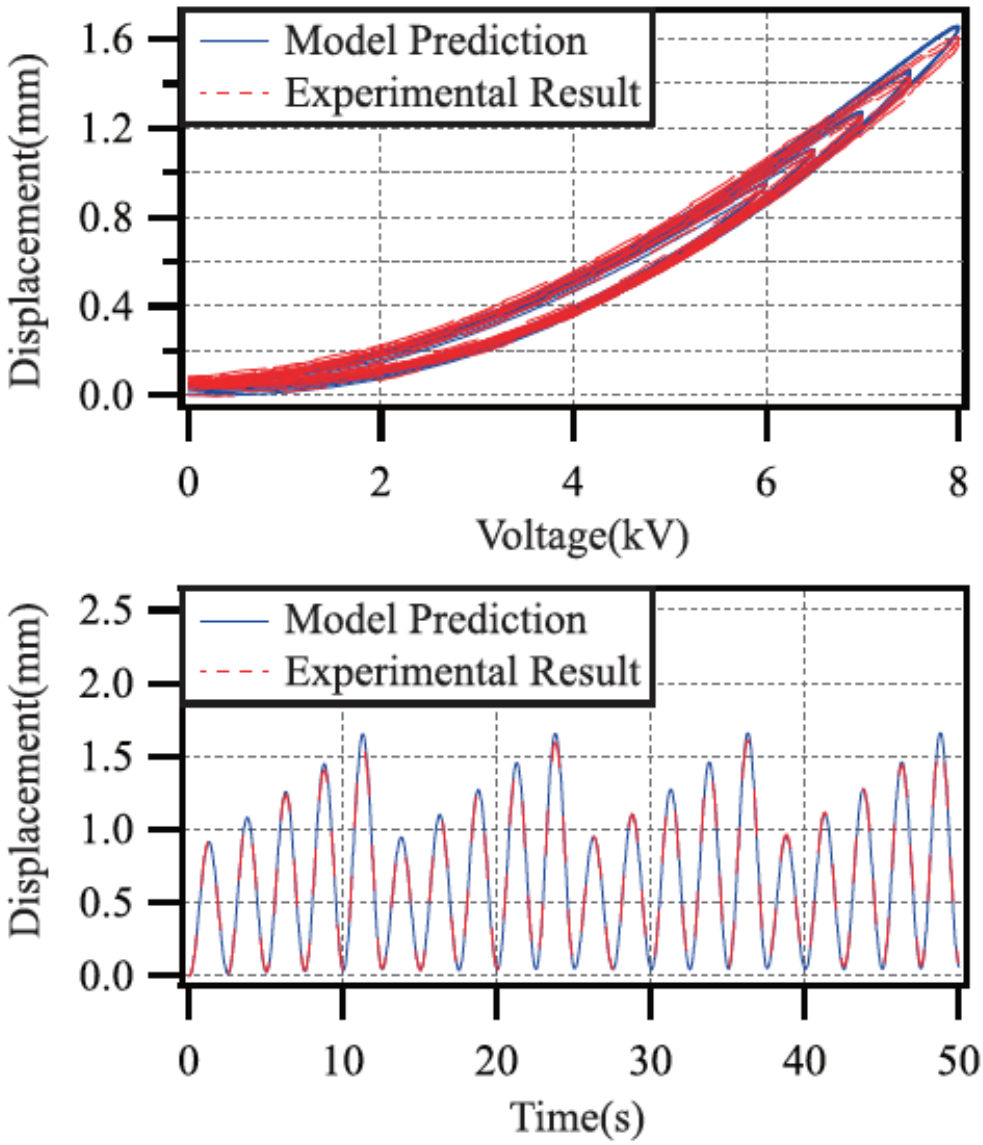

Figure 3.10: Comparisons of model prediction and experimental result with driving voltage frequency $0.4Hz$

real-time displacement data obtained from a laser sensor is employed to calculate the accelerated velocity of the weight through a third-order differentiator. Utilizing Newton's second law, the output force of the DEA is determined based on the acquired displacement and velocity data. Furthermore, the output force corresponding to the model prediction is calculated using the proposed dynamic model presented in Equation (3.24).

By employing this approach, a comprehensive comparison is conducted between

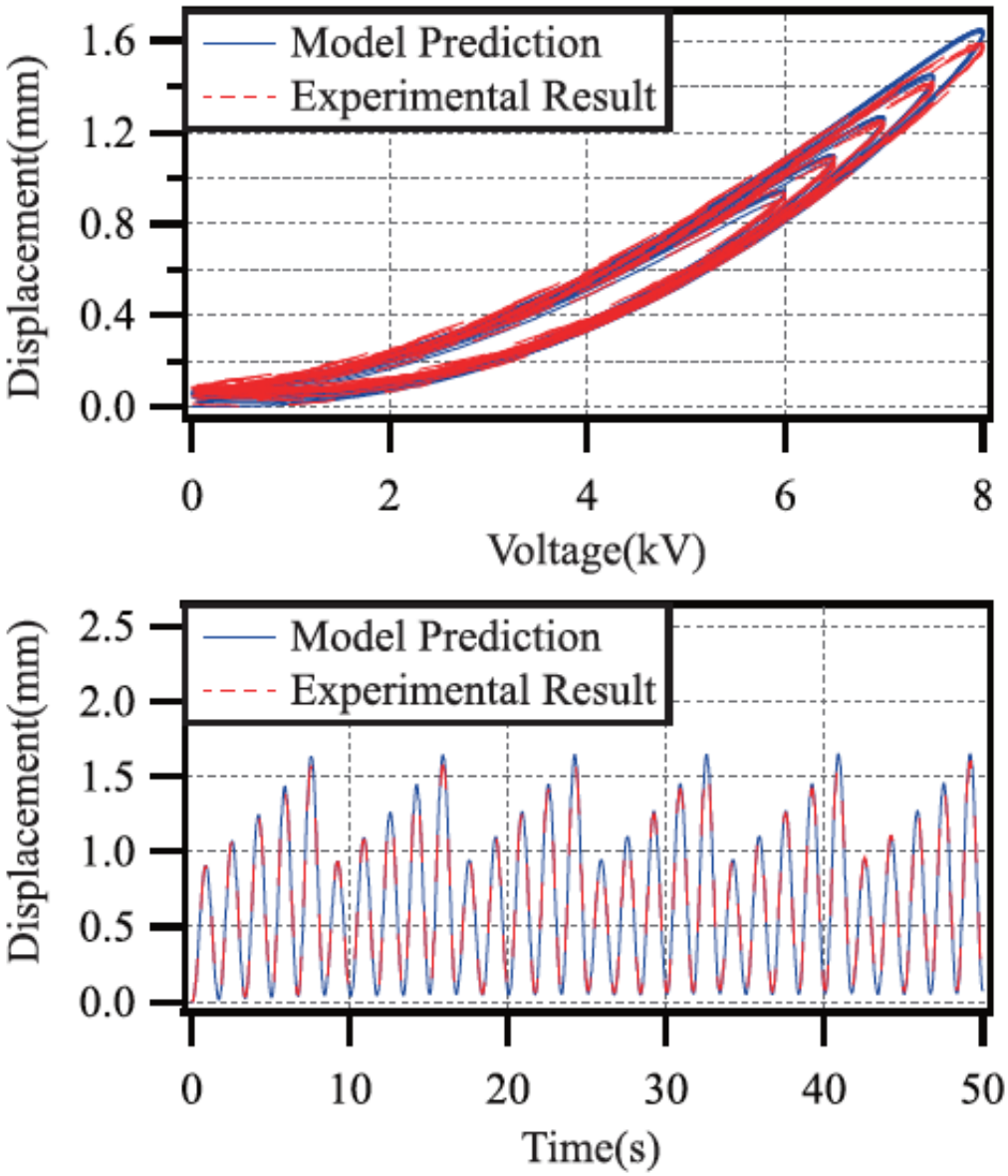

Figure 3.11: Comparisons of model prediction and experimental result with driving voltage frequency $0.6Hz$

the model predictions and the experimental results across force-versus-time, force-versus-displacement, and force-versus-voltage scenarios, as demonstrated in Figures 3.19 to 3.21. The root-mean-square error and the maximum tracking error associated with all test cases are calculated as 0.0028% and 6.0011% respectively. This further reinforces the validation and accuracy of the proposed dynamic model.

In the preceding sections, we established the validity of the model by subjecting it to driving voltages characterized by varying amplitudes and frequencies. Additionally, we conducted analyses involving force-versus-displacement and force-versus-voltage

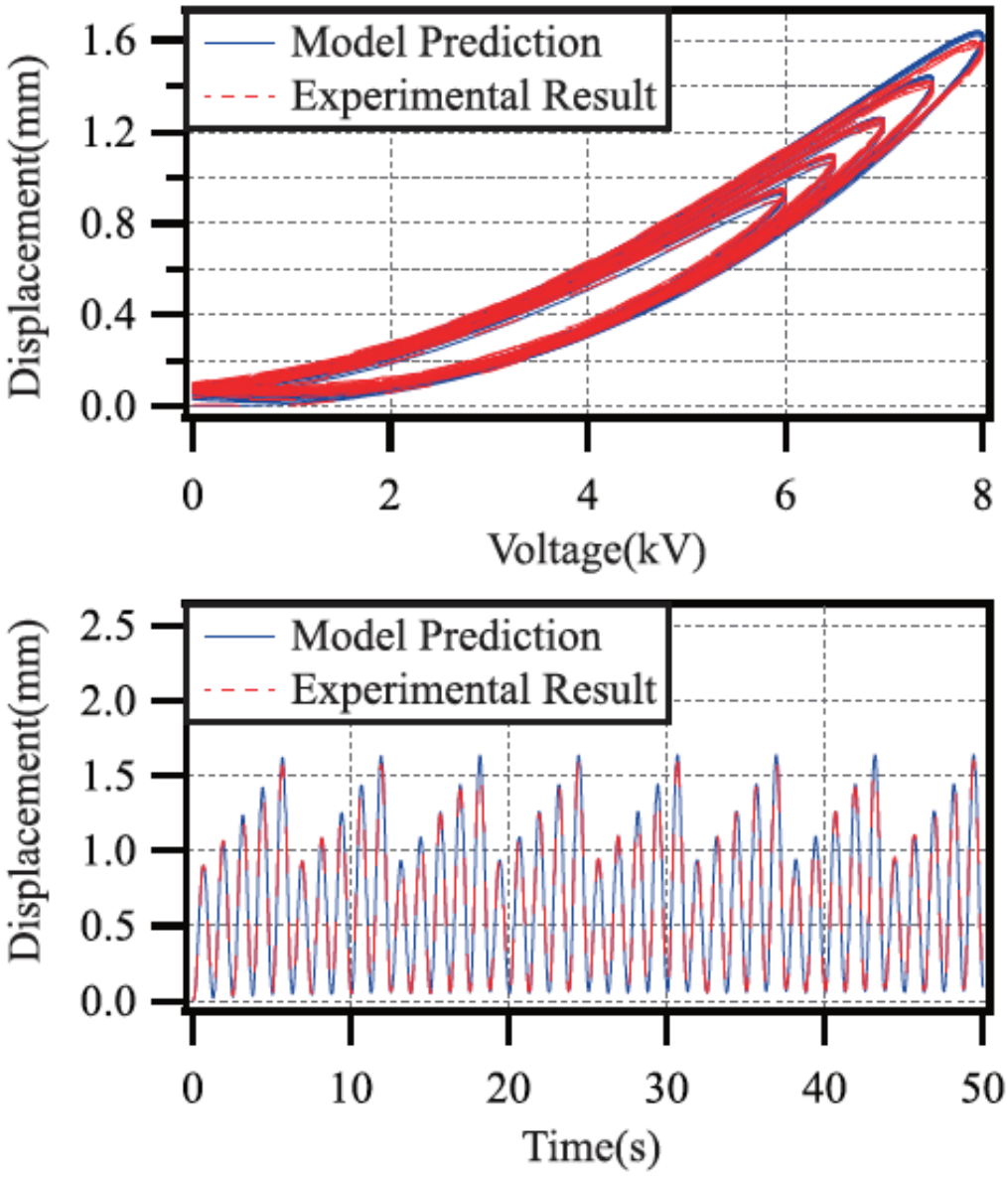

Figure 3.12: Comparisons of model prediction and experimental result with driving voltage frequency $0.8Hz$

scenarios, substantiating the reliability of the proposed dynamic model.

Subsequently, to further underscore the significance of the model, an amplitude-frequency response analysis is undertaken. Sinusoidal voltages spanning frequencies from $0.01, \mathrm{Hz}$ to $10, \mathrm{Hz}$ (with intervals of $0.01, \mathrm{Hz}$) are employed for theoretical calculations. The resulting amplitude-frequency response curve is illustrated in Figure 3.22. Notably, as the frequency of the driving voltage increases, the amplitude of the conical DEA gradually diminishes. This trend may stem from the viscoelastic

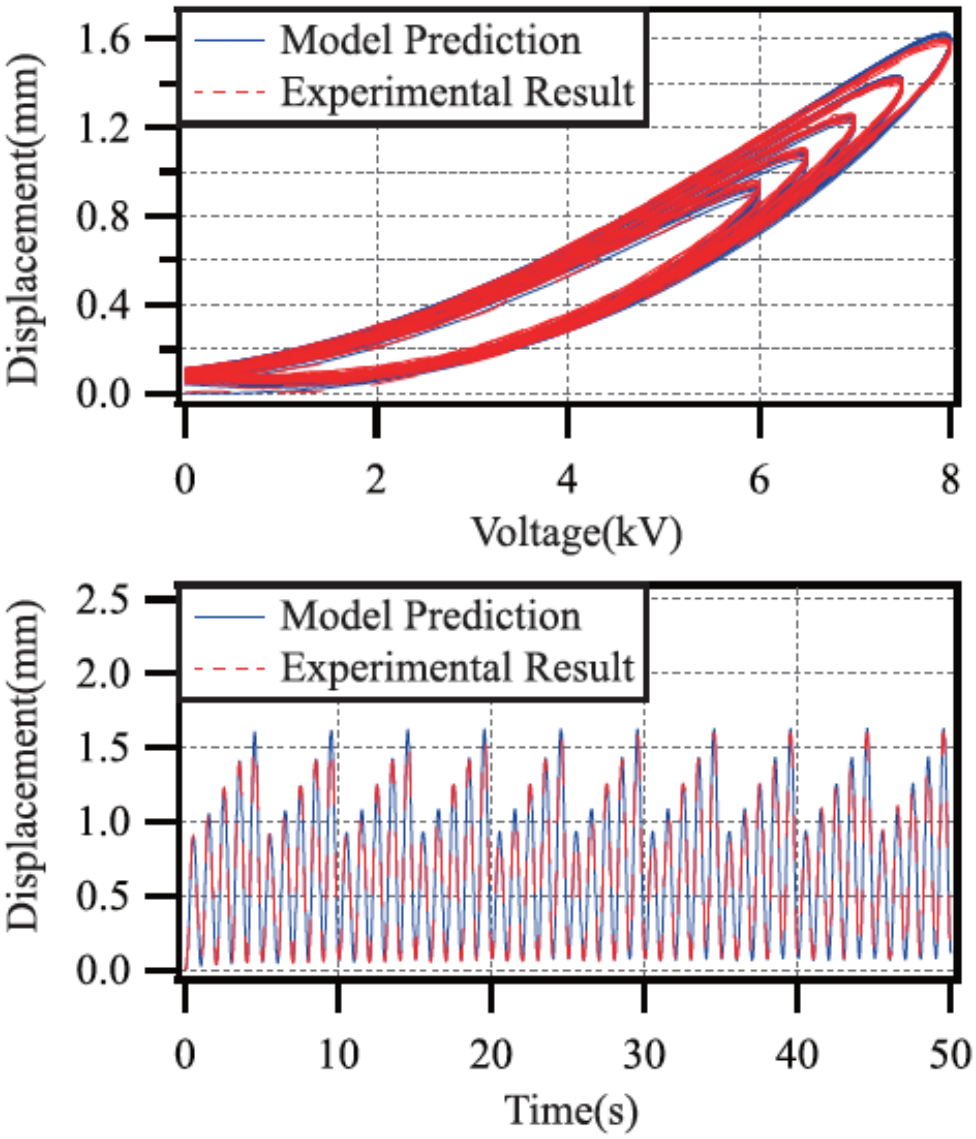

Figure 3.13: Comparisons of model prediction and experimental result with driving voltage frequency $1.0Hz$

properties inherent in the DE material [55].

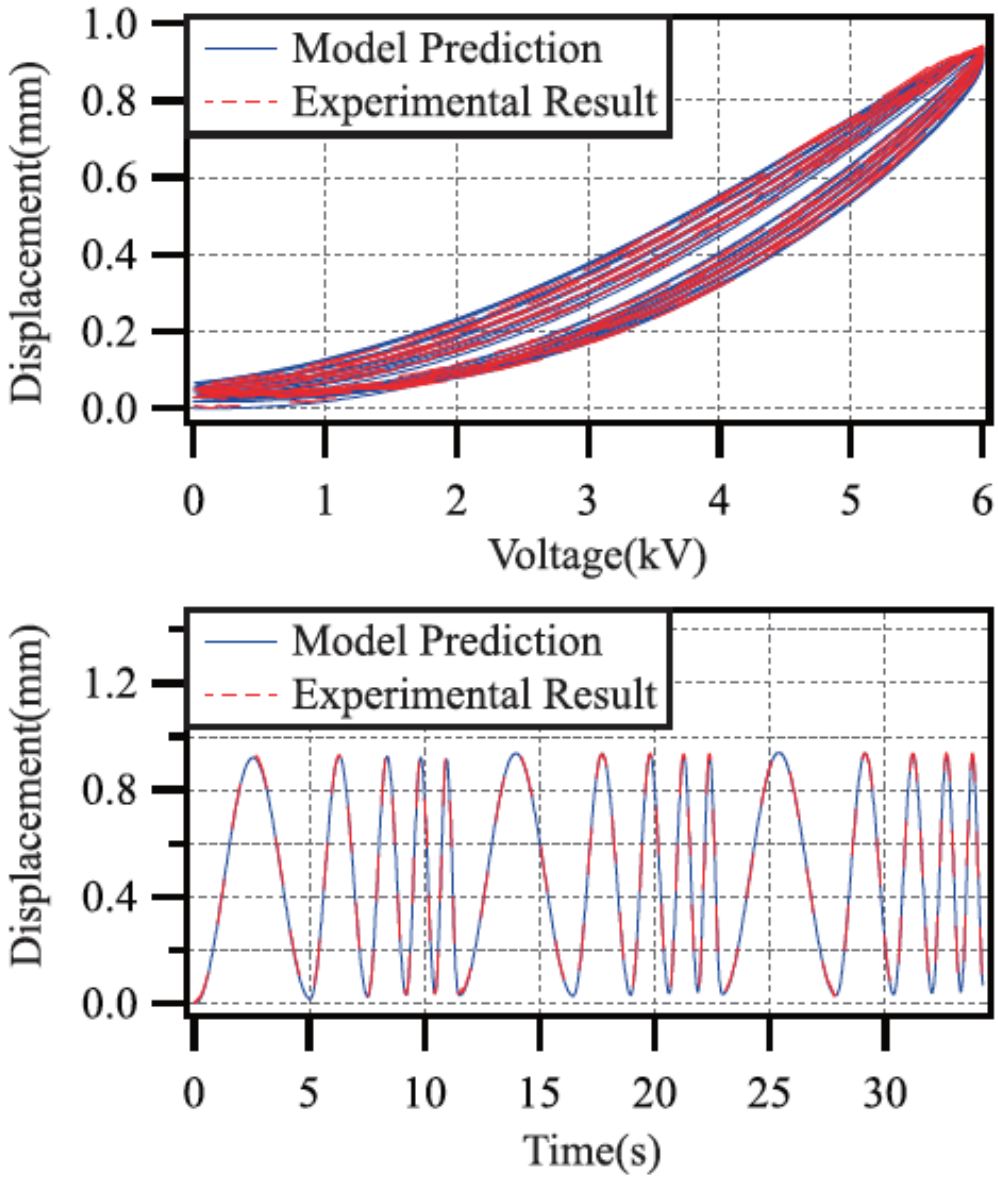

Figure 3.14: Comparisons of model prediction and experimental result with driving voltage amplitude $6.0kV$

Table 3.3: Errors of model validation with different driving voltage frequencies.

i	e_{rms}	e_m
a = 6.0	0.6047	1.7454
a = 6.5	0.7842	2.2600
a = 7.0	0.6878	1.5985
a = 7.5	1.2279	1.6069
a = 8.0	1.8889	2.5015

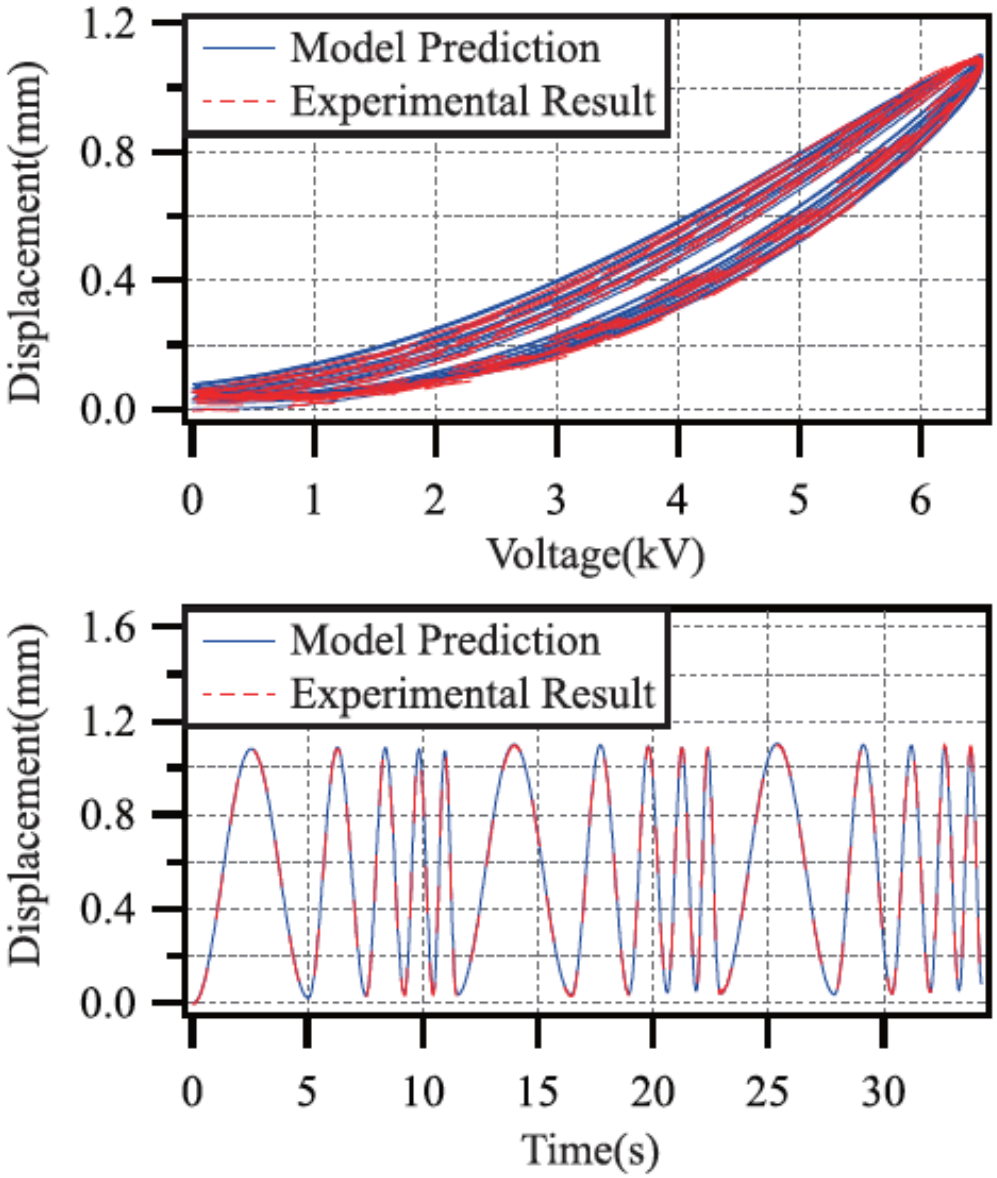

Figure 3.15: Comparisons of model prediction and experimental result with driving voltage amplitude $6.5kV$

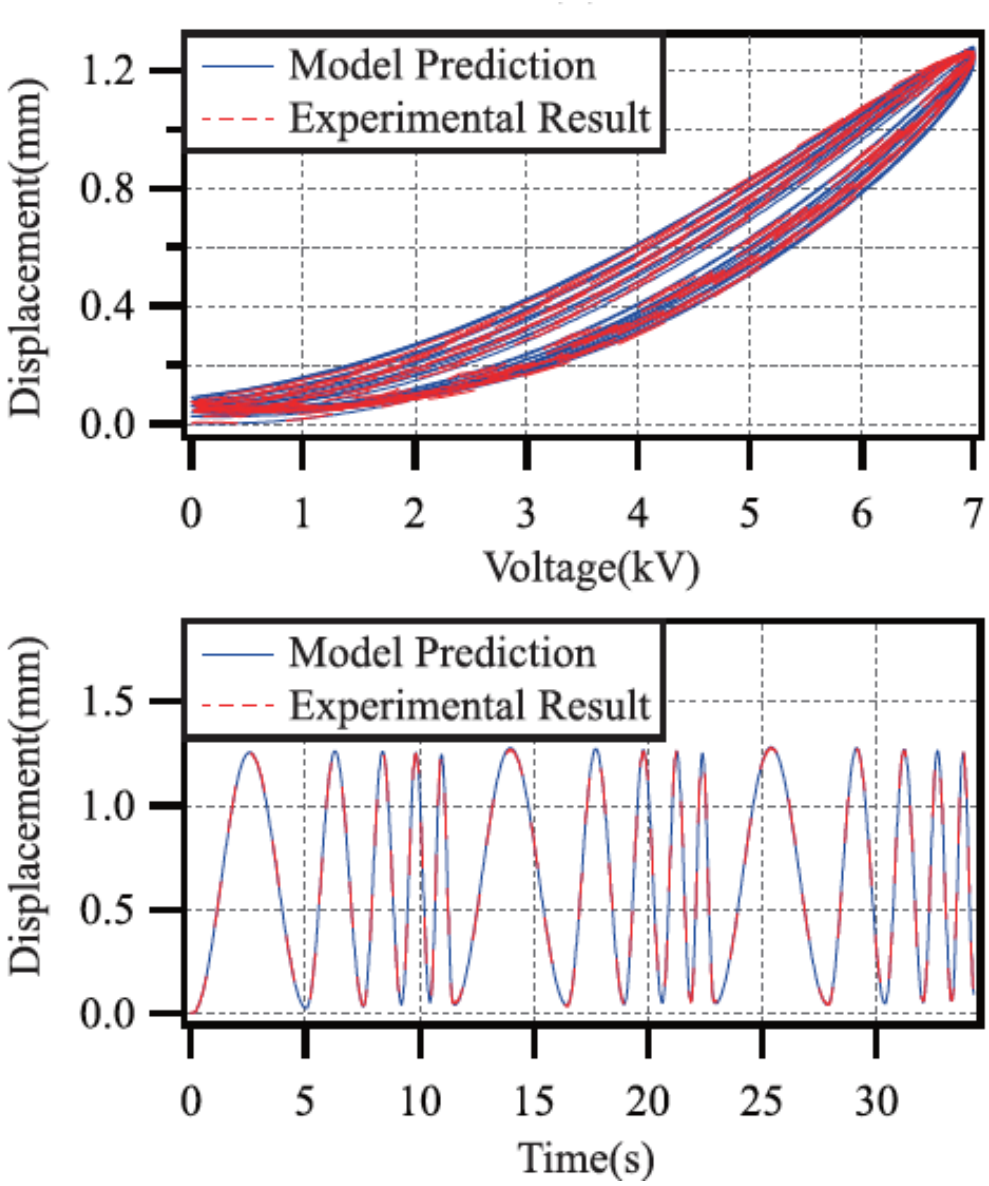

Figure 3.16: Comparisons of model prediction and experimental result with driving voltage amplitude $7.0kV$

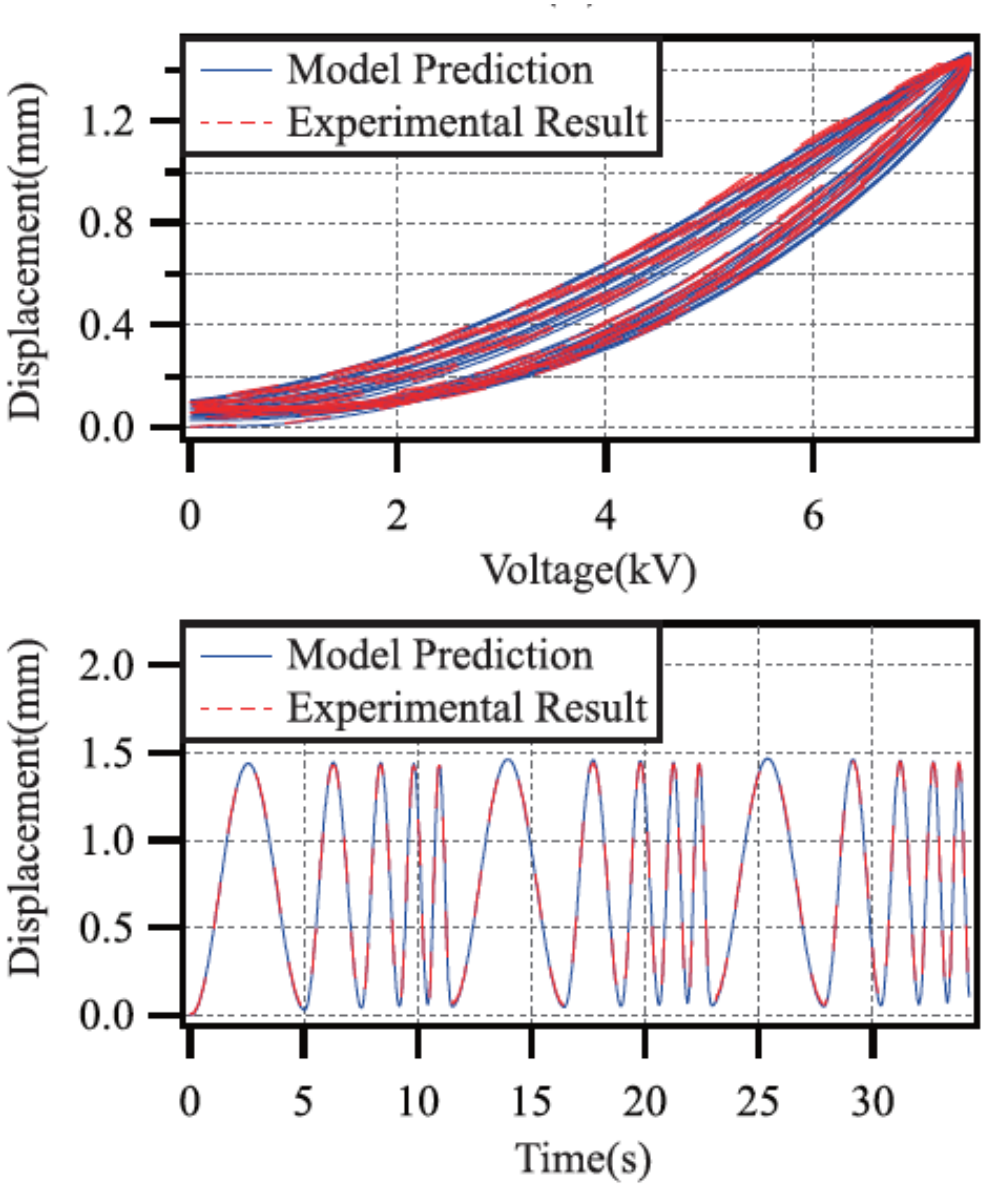

Figure 3.17: Comparisons of model prediction and experimental result with driving voltage amplitude $7.5kV$

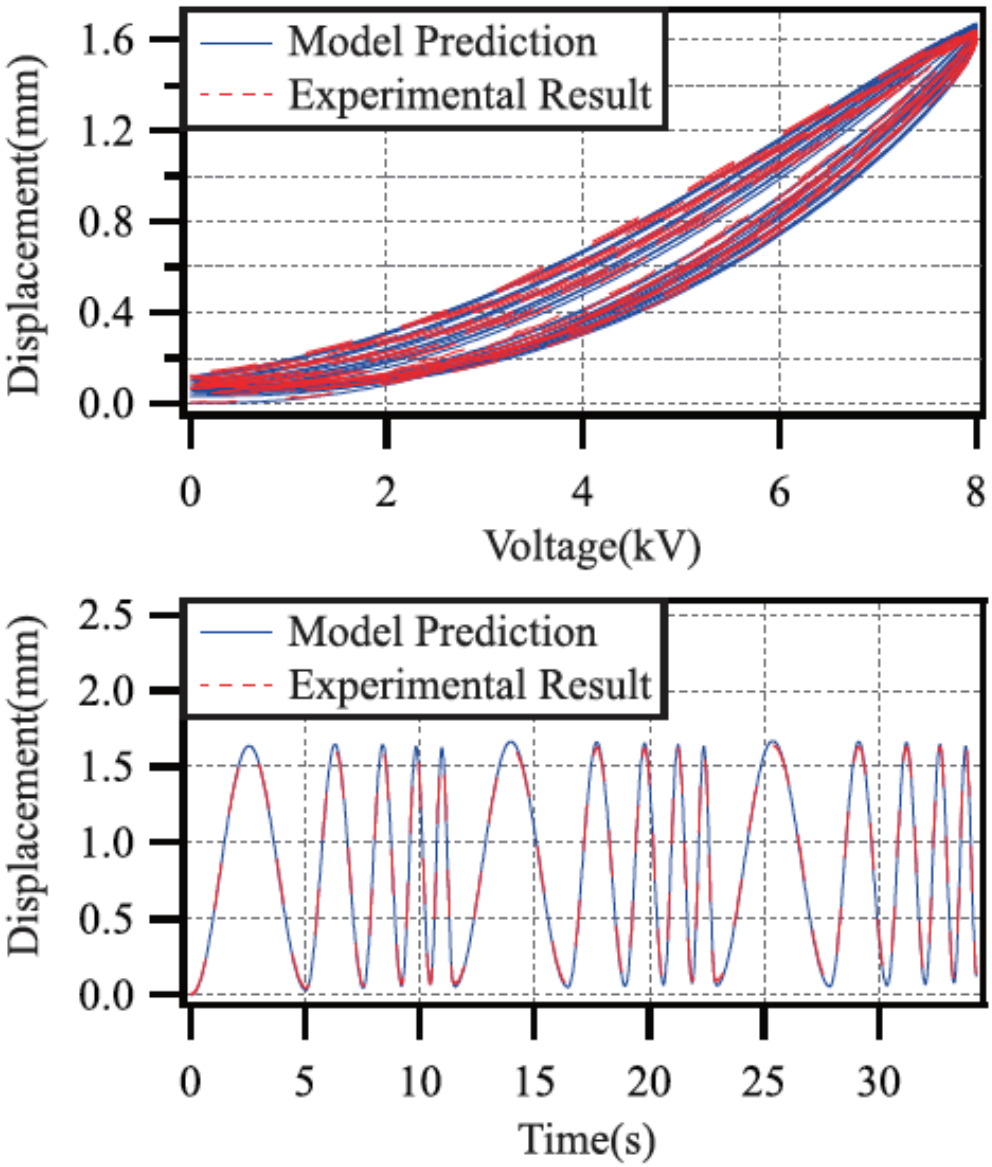

Figure 3.18: Comparisons of model prediction and experimental result with driving voltage amplitude $8.0kV$

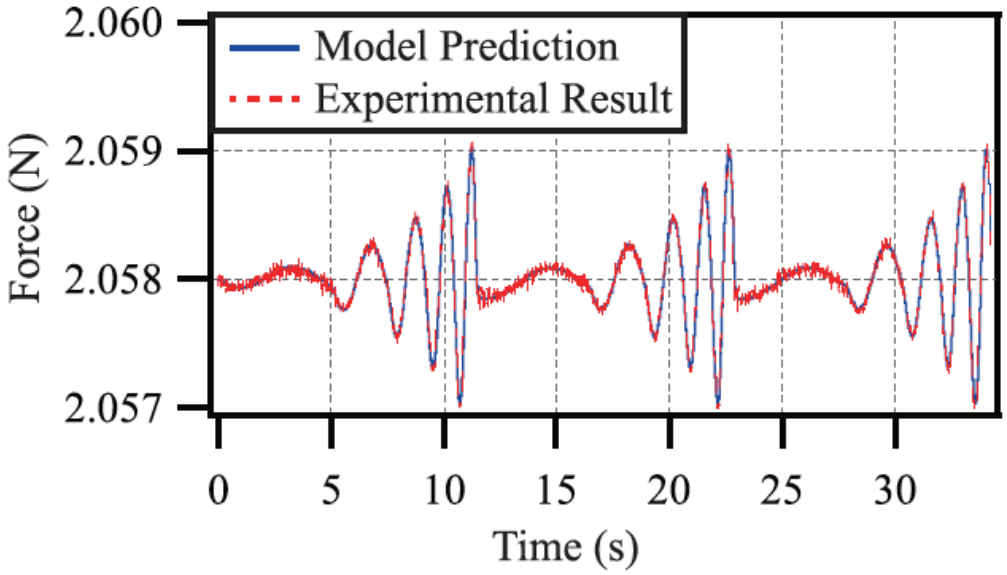

Figure 3.19: Comparisons of model prediction and experimental result corresponding to force versus time

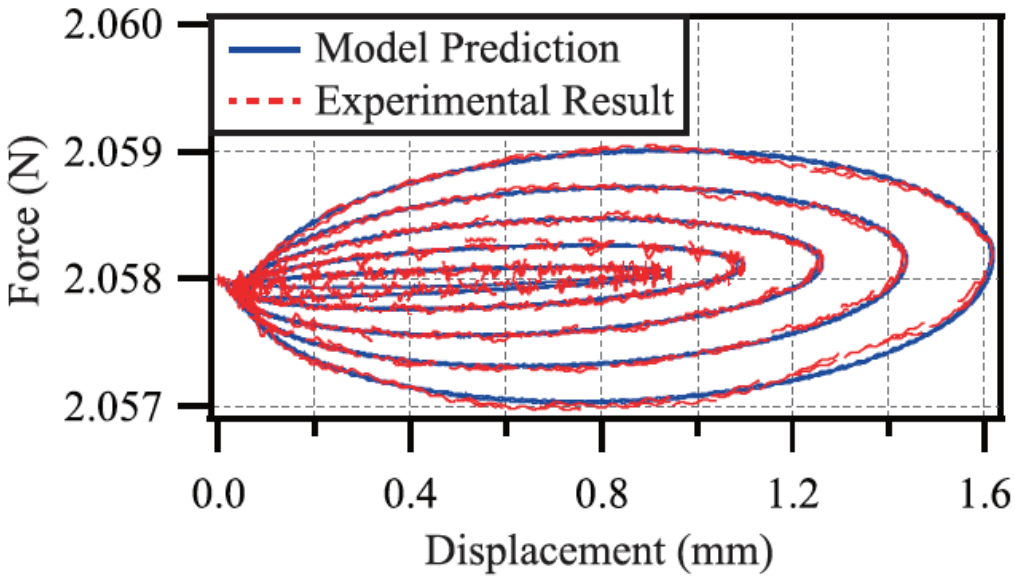

Figure 3.20: Comparisons of model prediction and experimental result corresponding to force versus displacement

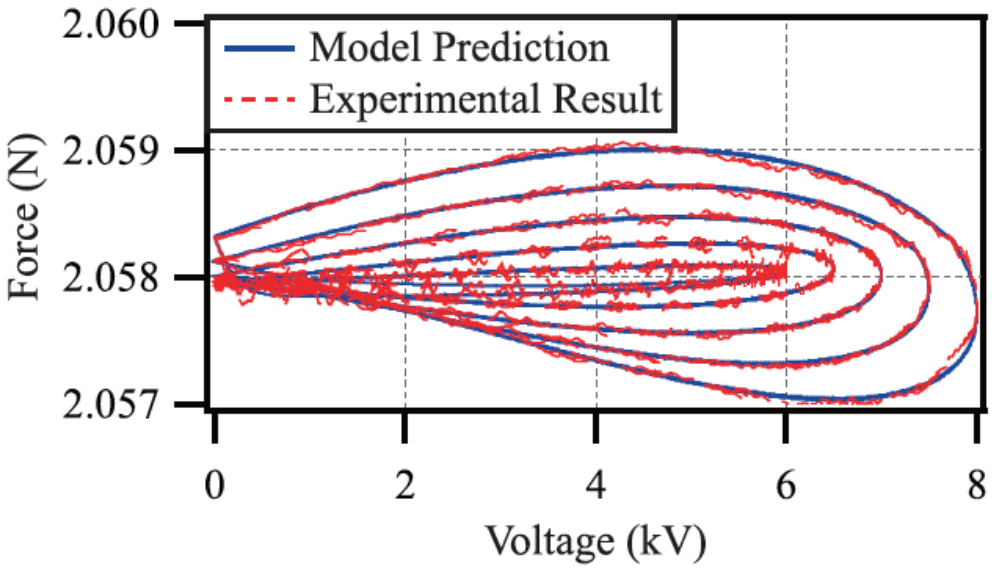

Figure 3.21: Comparisons of model prediction and experimental result corresponding to force versus voltage

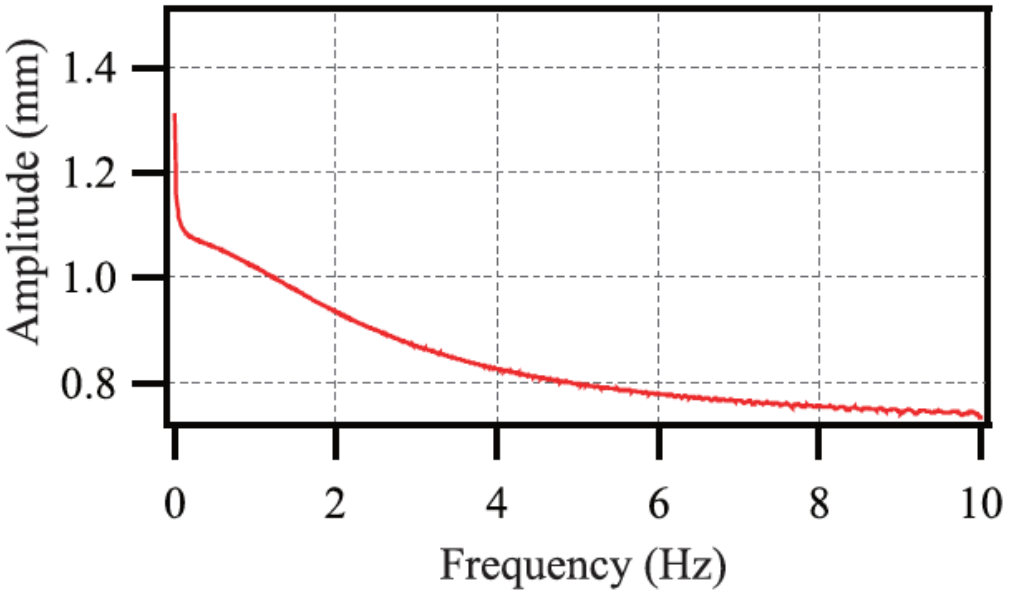

Figure 3.22: Amplitude-frequency response curve

3.3 Physics Based modeling for Planar Dielectric Elastomer Actuators

3.3.1 Model Development

In this section, we formulate a dynamic model for planar DEA, aiming to establish a comprehensive representation of the interplay between deformation and input voltage.

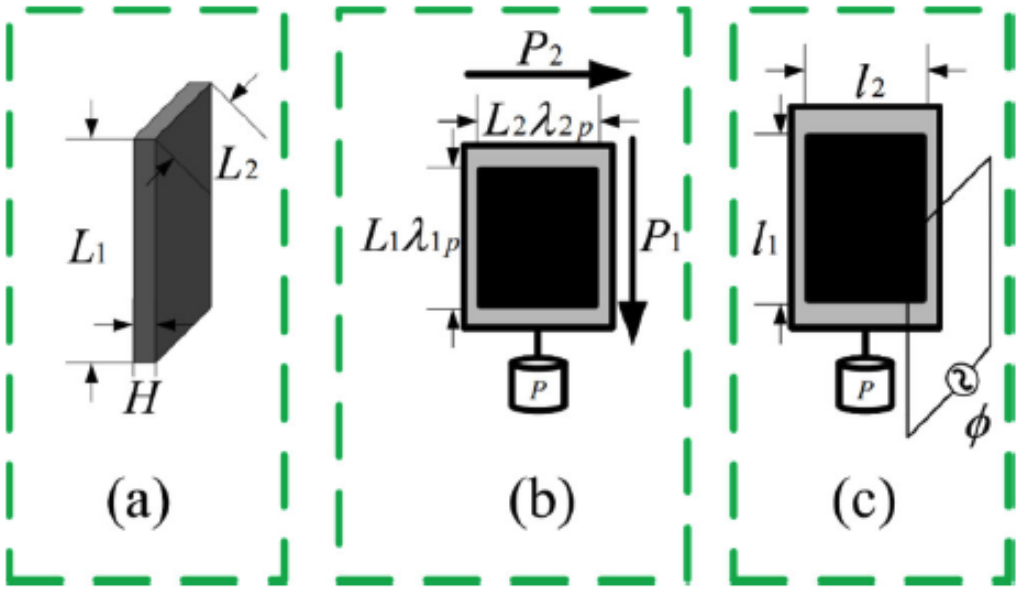

Figure 3.23: States of the DEA. (a) Initial state. (b) Pre-stretching state. (c) Electro-deformed state

Fig. 3.23 illustrates three distinct states of the Dielectric Elastomer Actuator (DEA). In the initial state shown in Fig. 3.23(a), the dimensions of the DEA, including length (L_1), width (L_2), and thickness (H), are defined. When an object with mass P is suspended beneath the DEA, it transforms into the pre-stretching state as depicted in Fig. 3.23(b). In this state, the stretches of the DEA are denoted by λ_{1p} and λ_{2p}, and the length and width are described as $\lambda_{1p}L_1$ and $\lambda_{2p}L_2$ respectively. The stresses parallel to the length and width are termed P_1 and P_2 respectively.

Upon application of voltage, the DEA enters the electro-deformed state represented in Fig. 3.23(c). Here, the dimensions of the DEA are expressed as l_1, l_2, and h for length, width, and thickness respectively. The stretches of the DEA in this state are indicated by $\lambda_1 = l_1/L_1$, $\lambda_2 = l_2/L_2$, and $\lambda_3 = h/H$. It is important to note that the DEA is assumed to be incompressible, leading to the relationship $\lambda_1\lambda_2\lambda_3 = 1$.

The true stresses parallel to the length and width directions of the Dielectric Elastomer Actuator (DEA) are defined as $\sigma_1 = P_1/(l_2 h)$ and $\sigma_2 = P_2/(l_1 h)$, respectively.

When the DEA is subjected to a voltage ϕ through its thickness, the accumulated charge on the electrode is defined as Q. The true electric field is denoted by $E = \phi/h$, and the true electric displacement is represented as $D = Q/(l_1 l_2)$.

The free energy of the Dielectric Elastomer Actuator (DEA) is denoted as G. When the dimensions parallel to the length and width directions of the DEA change by δl_1 and δl_2 respectively, the work done by the mechanical force is expressed as $P_1 \delta l_1 + P_2 \delta l_2$.

In the electro-deformed state, the change in charge is denoted as δQ, and the work done by the electric field force is represented as $\phi \delta Q$. According to the principle of nonequilibrium thermodynamics [32], the increase in free energy should not exceed the total work done, specifically:

$$\delta G = P_1 \delta l_1 + P_2 \delta l_2 + \phi \delta Q \tag{3.27}$$

The DEA can be regarded as a capacitor, allowing Q to be expressed as:

$$Q = \varepsilon \phi L_1 L_2 (\lambda_1 \lambda_2)^2 / h \tag{3.28}$$

The Helmholtz free energy density of the DEA is defined as $W = G/(L_1 L_2 H)$. Combining this with Eq. (3.27), we can obtain:

$$\delta W = \frac{\sigma_1}{\lambda_1} \delta \lambda_1 + \frac{\sigma_2}{\lambda_2} \delta \lambda_2 + 2\varepsilon \left(\frac{\phi}{H}\right)^2 (\lambda_1 \lambda_2^2 \delta \lambda_1 + \lambda_2 \lambda_1^2 \delta \lambda_2) \tag{3.29}$$

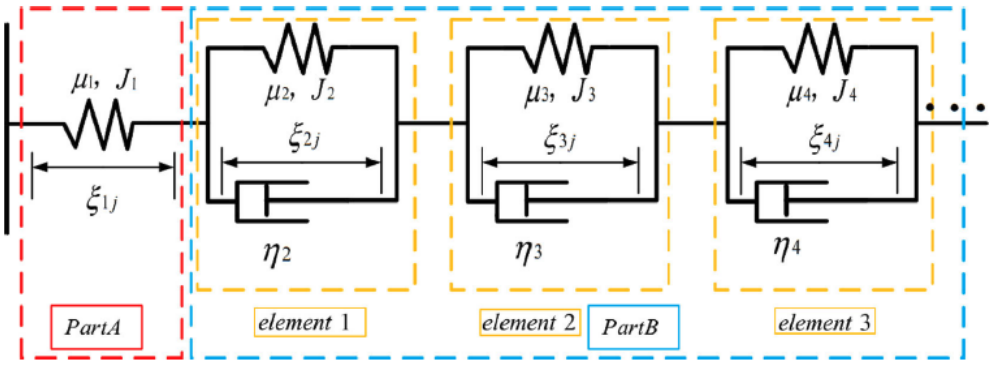

Figure 3.24: The generalized Kelvin model, which is divided into two main parts

Figure 3.24 illustrates the generalized Kelvin model, which is divided into two

parts. Part A consists of a spring, while Part B is composed of elements that include springs and dampers in parallel arrangement, designated as element 1, element 2, and so forth. The determination of the number of springs and dampers is based on experimental results and the desired level of accuracy.

The generalized Kelvin model effectively characterizes the viscoelastic behavior of the DEA. Here, ξ_{ij} represents the elastic deformation of each element, where i corresponds to the element number and j takes values of 1 or 2, denoting the vertical and horizontal directions respectively.

In each element, the spring and damper are in parallel configuration, resulting in consistent deformations between them. Since all elements are connected in series, the overall deformation of the DEA is the sum of deformations across each element. As a result, $\lambda_1 = \sum_{i=1}^{n} \xi_{i1}$ and $\lambda_2 = \sum_{i=1}^{n} \xi_{i2}$.

For the ideal DEA, W is assumed to be a function of ξ_{ij} and D, and it can be expressed as:

$$W(D, \xi 11, \xi_{12}, \xi_{21}, \xi 22, \cdots) = W_s(\xi 11, \xi_{12}, \xi_{21}, \xi 22, \cdots) + \frac{D^2}{2\varepsilon} \tag{3.30}$$

where ε represents the permittivity of the DEA, and it can be expressed as $\varepsilon = D/E$. $W_s(\xi_{11}, \xi_{12}, \xi_{21}, \xi_{22}, \cdots)$, which is the elastic energy, is relevant to the internal stretching of the DEA. The term $D^2/(2\varepsilon)$, which represents the electronic energy, is relevant to the dielectric properties of the DEA.

The Gent model is employed to describe the free energy density of the DEA. When combined with the expression of the generalized Kelvin model, the internal free energy density W_s can be expressed as:

$$W_s(\xi 11, \xi_{12}, \xi_{21}, \xi 22, \cdots) = -\sum_{i=1}^{n} \frac{\mu_i J_i}{2} ln(1 - \frac{\xi_{i1}^2 + \xi_{i2}^2 + \xi_{i1}^{-2}\xi_{i2}^{-2} - 3}{J_i}) \tag{3.31}$$

where μ_i represents the shear modulus of the ith spring, and J_i represents the deformation limit of the ith spring, as illustrated in Fig. 3.24.

Combining Eqs. (3.29)–(3.31), we can obtain:

$$\begin{cases} \sigma_1 + \varepsilon E^2 = \mu_1 \dfrac{\xi_{11}^2 - \xi_{11}^{-2}\xi_{12}^{-2}}{1 - \frac{\xi_{i1}^2 + \xi_{i2}^2 + \xi_{i1}^{-2}\xi_{i2}^{-2} - 3}{J_1}} \\ \sigma_2 + \varepsilon E^2 = \mu_1 \dfrac{\xi_{12}^2 - \xi_{11}^{-2}\xi_{12}^{-2}}{1 - \frac{\xi_{i1}^2 + \xi_{i2}^2 + \xi_{i1}^{-2}\xi_{i2}^{-2} - 3}{J_1}} \end{cases} \tag{3.32}$$

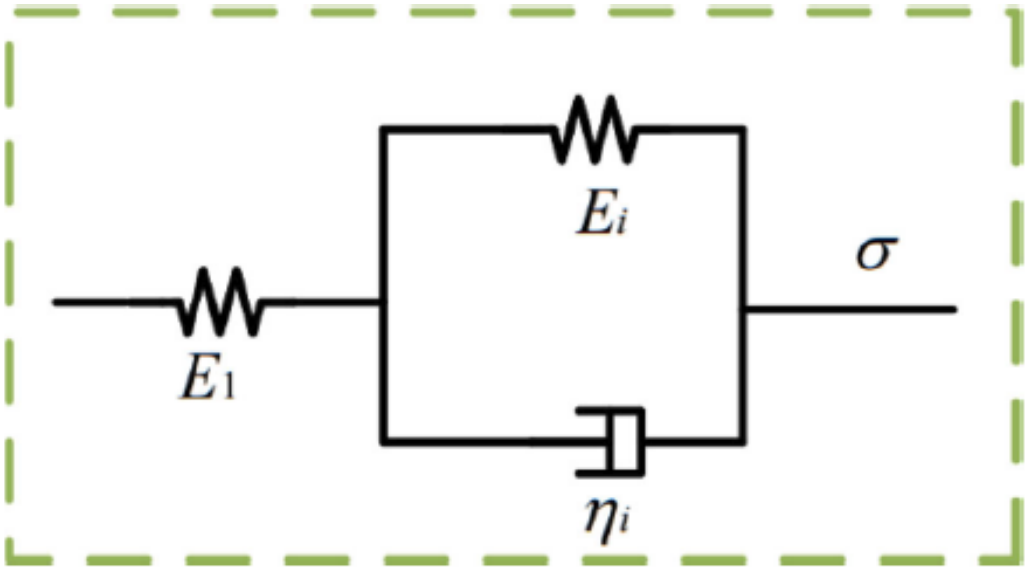

Figure 3.25: Mechanical relation diagram of a spring and damper in an element of the generalized Kelvin model

Figure 3.25 depicts the mechanical relationship of each element within the generalized Kelvin model. The viscoelastic coefficient of the damper is defined as η_i, where i denotes the damper number. By adhering to the principles of Newtonian mechanics, we derive:

$$\begin{cases} \sigma_1 = \sigma_{i1} + \eta_i \dfrac{d\xi_{i1}}{dt} \\ \sigma_2 = \sigma_{i2} + \eta_i \dfrac{d\xi_{i2}}{dt} \end{cases} \tag{3.33}$$

Since there is prestretching stress in the vertical direction but no prestretching stress in the horizontal direction, combining Eqs. (3.29)–(3.33), we obtain:

$$\begin{cases} \dfrac{d\xi_{i1}}{dt} = \dfrac{1}{\eta_i}\mu_i \dfrac{\xi_{11}^2 - \xi_{11}^{-2}\xi_{12}^{-2}}{1 - \frac{\xi_{11}^2+\xi_{12}^2+\xi_{11}^{-2}\xi_{12}^{-2}-3}{J_1}} - \dfrac{1}{\eta_i}\mu_i \dfrac{\xi_{i1}^2 - \xi_{i1}^{-2}\xi_{i2}^{-2}}{1 - \frac{\xi_{i1}^2+\xi_{i2}^2+\xi_{i1}^{-2}\xi_{i2}^{-2}-3}{J_i}} \\ \dfrac{d\xi_{i2}}{dt} = 0 \end{cases} \tag{3.34}$$

where $i(= 2, 3, 4, \cdots)$ represents the number of springs in the generalized Kelvin model. When $\phi = 0$, the DEA is only affected by the prestretching stress in the vertical direction. In this case, we have $\lambda_1 = \lambda_{1p}$, $\lambda_2 = 1$, $\xi_{i1} = \lambda_{1p}$, and $\xi_{i2} = 1$. Substituting these parameters into Eq. (3.31), we obtain:

$$\sigma_1 = \mu_1 \left(\frac{\lambda_{1p}^2 - \lambda_{1p}^{-2}}{1 - \frac{\lambda_{1p}^2 + \lambda_{1p}^{-2} - 2}{J_1}} \right) \tag{3.35}$$

Since $\sigma_1 = P_1/(l_2 h)$, the prestretching stress P_1 can be expressed as:

$$P_1 = \mu_1 L_2 H \left(\frac{\lambda_{1p}^2 - \lambda_{1p}^{-2}}{1 - \frac{\lambda_{1p}^2 + \lambda_{1p}^{-2} - 2}{J_1}} \right) \tag{3.36}$$

By substituting $\sigma_1 = P_1/(l_2 h)$ and $E = \phi/h$ into Eq. (3.32), we can derive the relationship between P_1 and ϕ, as well as ξ_{i1} and ξ_{i2}, which can be expressed as:

$$P_1 = l_2 h \left(\mu_1 \frac{\xi_{11}^2 - \xi_{11}^{-2}\xi_{12}^{-2}}{1 - \frac{\xi_{11}^2 + \xi_{12}^2 + \xi_{11}^{-2}\xi_{12}^{-2} - 3}{J_1}} - \varepsilon (\frac{\phi}{h})^2 \right) \tag{3.37}$$

Given that the volume of the DEA remains constant and there is no deformation in the horizontal direction, we can deduce:

$$\begin{cases} l_1 l_2 h = L_1 L_2 H \\ l_1 = \dfrac{L_1}{n} \displaystyle\sum_{i=1}^{n} \xi_{i1} \\ l_2 = L_2 \end{cases} \tag{3.38}$$

Combining Eqs. (3.37) and (3.38), we obtain:

$$P_1 = L_2 \frac{nH}{\sum_{i=1}^{n} \xi_{i1}} \left(\mu_1 \frac{\xi_{11}^2 - \xi_{11}^{-2}\xi_{12}^{-2}}{1 - \frac{\xi_{11}^2 + \xi_{12}^2 + \xi_{11}^{-2}\xi_{12}^{-2} - 3}{J_1}} - \varepsilon \left(\frac{\phi \sum_{i=1}^{n} \xi_{i1}}{nH} \right)^2 \right) \tag{3.39}$$

When we differentiate both sides of Eq. (3.39) with respect to time, we obtain:

$$\frac{dP_1}{dt} = \frac{\partial P_1}{\partial \phi} \frac{d\phi}{dt} + \sum_{i=1}^{n} \frac{\partial P_1}{\partial \xi_{i1}} \frac{d\xi_{i1}}{dt} + \sum_{i=1}^{n} \frac{\partial P_1}{\partial \xi_{i2}} \frac{d\xi_{i2}}{dt} \tag{3.40}$$

Considering the fact that P_1 given by Eq. (3.40) is constant, we have $dP_1/dt = 0$. Additionally, since the horizontal stretch of the DEA does not change with time, we obtain $d\xi_{i2}/dt = 0$. Therefore, Eq. (3.40) can be reformulated as:

$$\frac{\xi_{11}}{dt} = -\left(\frac{\partial P_1}{\partial \phi} \frac{d\phi}{dt} + \sum_{i=1}^{n} \frac{\partial P_1}{\partial \xi_{i1}} \frac{d\xi_{i1}}{dt} \right) / \frac{\partial P_1}{\partial \xi_{11}} \tag{3.41}$$

By combining Eqs. (3.34) and (3.41), we can derive the dynamic model of the DEA, which can be expressed in a rearranged form as Eq. (3.42).

$$
\begin{cases}
\dfrac{\xi_{11}}{dt} = -\left(\dfrac{\partial P_1}{\partial \phi}\dfrac{d\phi}{dt} + \displaystyle\sum_{i=1}^{n}\dfrac{\partial P_1}{\partial \xi_{i1}}\dfrac{d\xi_{i1}}{dt}\right) / \dfrac{\partial P_1}{\partial \xi_{11}} \\
\dfrac{d\xi_{12}}{dt} = 0 \\
\dfrac{d\xi_{i1}}{dt} = \dfrac{1}{\eta_i}\mu_i \dfrac{\xi_{11}^2 - \xi_{11}^{-2}\xi_{12}^{-2}}{1 - \frac{\xi_{11}^2+\xi_{12}^2+\xi_{11}^{-2}\xi_{12}^{-2}-3}{J_1}} - \dfrac{1}{\eta_i}\mu_i \dfrac{\xi_{i1}^2 - \xi_{i1}^{-2}\xi_{i2}^{-2}}{1 - \frac{\xi_{i1}^2+\xi_{i2}^2+\xi_{i1}^{-2}\xi_{i2}^{-2}-3}{J_i}} \\
\dfrac{d\xi_{i2}}{dt} = 0
\end{cases}
\tag{3.42}
$$

3.3.2 Actuation Voltages

To determine the parameters of the developed model, it is essential to introduce the driving voltage applied in the experiment. We will utilize the actuation signals for conical DEAs, as described in Eq. (3.25).

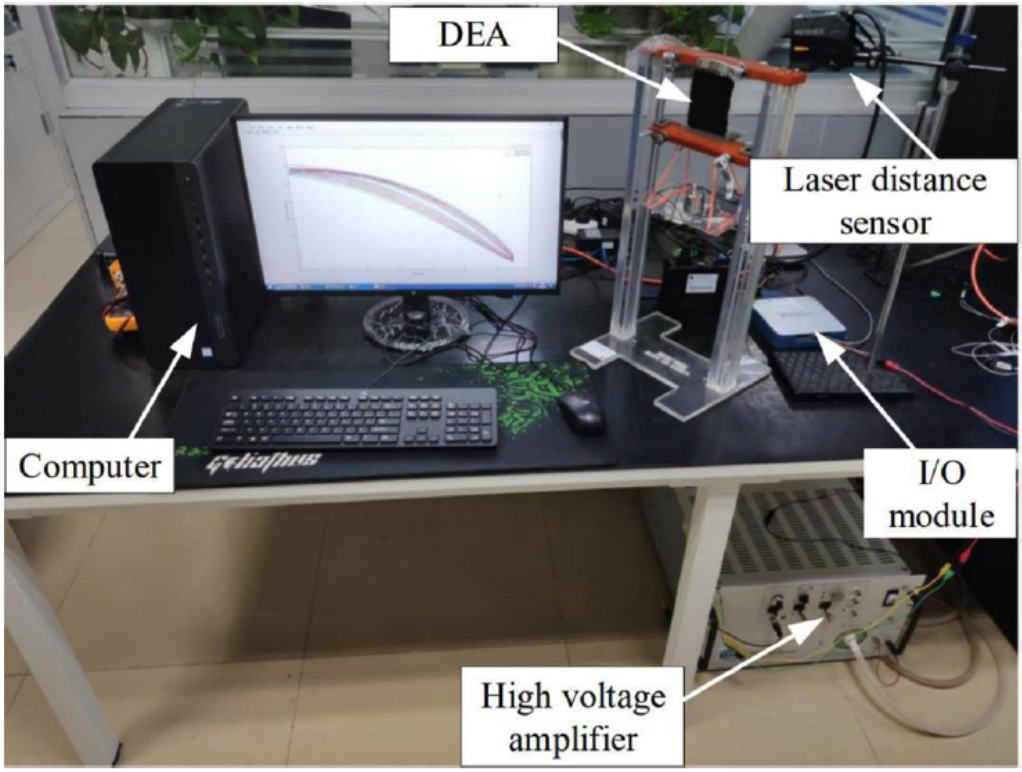

Figure 3.26: Picture of experimental platform for planar DEA, which mainly includes computer, high voltage amplifier, laser distance sensor, I/O module and planar DEA.

3.3.3 Parameters Identification

In this section, the parameters of the proposed dynamic model are determined based on experimental results. The amplitudes of the driving voltage are selected as $a_i = 5.5 + 0.5i$ kV, and the frequencies are chosen to be $f_i = 0.2i$ Hz, mirroring those used in conical DEAs. Consequently, the driving voltage encompasses various amplitudes and frequencies within a single period. To quantify the accuracy of the model, we employ the root-mean-square error and the maximum modeling error, defined as per Eq. (3.26), for the sake of accuracy description.

The differential evolutionary algorithm, as depicted in Figure 3.27, is employed for the identification of parameters in the dynamic model given by Eq. (3.42). The hyperparameters of the differential evolutionary algorithm are defined as follows: the search ranges are set as $\Omega_1 \in (10^3, 9\times10^4)$, $\Omega_2 \in (10^3, 2\times10^4)$, and $\Omega_3 \in (10^3, 3\times10^4)$. The maximum number of evolution generations, denoted by G, is set to be 150. The constant d is set at 0.001. The mutation rate p_m is 0.6, and the crossover rate p_c is 0.9. Moreover, the permittivity of the DEA, denoted as e, is set to be $4.7\varepsilon_0$, where ε_0 is the permittivity of vacuum. The geometrical parameters of the DEA are listed in Table 3.4.

Table 3.4: Geometry parameters of DEA for experiment platform

Parameter	value
L_1	0.075 m
L_2	0.072 m
H	0.001 m
P	200 g
$\lambda_{1p}L_2$	0.082 m
$\lambda_{1p}L_2$	0.072 m

Considering both numerical accuracy and computational load, we opt for the 3-links generalized Kelvin model to effectively describe the viscoelastic characteristics of the DEA. This choice facilitates a comparison between the model's prediction output and the experimental results, as depicted in Figure 3.28. The outcomes of the parameter identification process are presented in Table 3.5.

3.3.4 Model Validation

In this section, we establish the generalization of the dynamic model by conducting two separate sets of experiments. In the first set of trials, we validate the model's

Algorithm: *differential evolutionary algorithm*

1 **begin**
2 Define the search ranges of variables $\mu_i(i=1,2,...,n)$, $J_i(i=1,2,...n)$ and $\eta_i(i=2,3,...n)$ as Ω_1, Ω_2 and Ω_3, respectively. Then, initialize $g=0$.
3 According to Ω_1, Ω_2 and Ω_3, randomly initialize the initial population as $\chi_k(0)(k=1,2,\ldots,N)$, where $\chi_k(0)=\{\tilde{\mu}_i^k(0),\tilde{J}_i^k(0),\tilde{\eta}_i^k(0)\}$.
4 **For** $g=0:G$ **do**
5 Substituting $\chi_k(g)$ into (19). Then, call **ode15s** solver to get the $\tilde{\xi}_{i1}^k(g)$ and $\tilde{\xi}_{i2}^k(g)$ by solving (19).
6 According to the experimental data and $\tilde{\xi}_{i1}^k(g)$, $\tilde{\xi}_{i2}^k(g)$, calculate (21).
7 **If** $ems<\delta$ (δ is a small positive constant), **then**
8 The parameters in dynamic model (19) are obtained. That is, $\mu_i=\tilde{\mu}_i^k(g)$, $J_i=\tilde{J}_i^k(g)$ and $\eta_i=\tilde{\eta}_i^k(g)$.
9 **Break**;
10 **End If**
11 According to the mutation rate p_m and the crossover rate p_c, update $\chi_k(g)$ by executing mutation operation, crossover operation and selection operation in turn.
12 **End For**

Figure 3.27: Differential Evolution algorithm used for identification

Table 3.5: Parameters of the planar DEA model.

i	$\mu_i(kPa)$	J_i	η_i
i=1	48637.812	9980.487	N/A
i=2	41184.378	4830.083	16392.456
i=3	58273.732	9768.832	19795.386

performance across a range of driving voltage amplitudes. Subsequently, in the second set of experiments, we assess the model's accuracy across a variety of driving voltage frequencies.

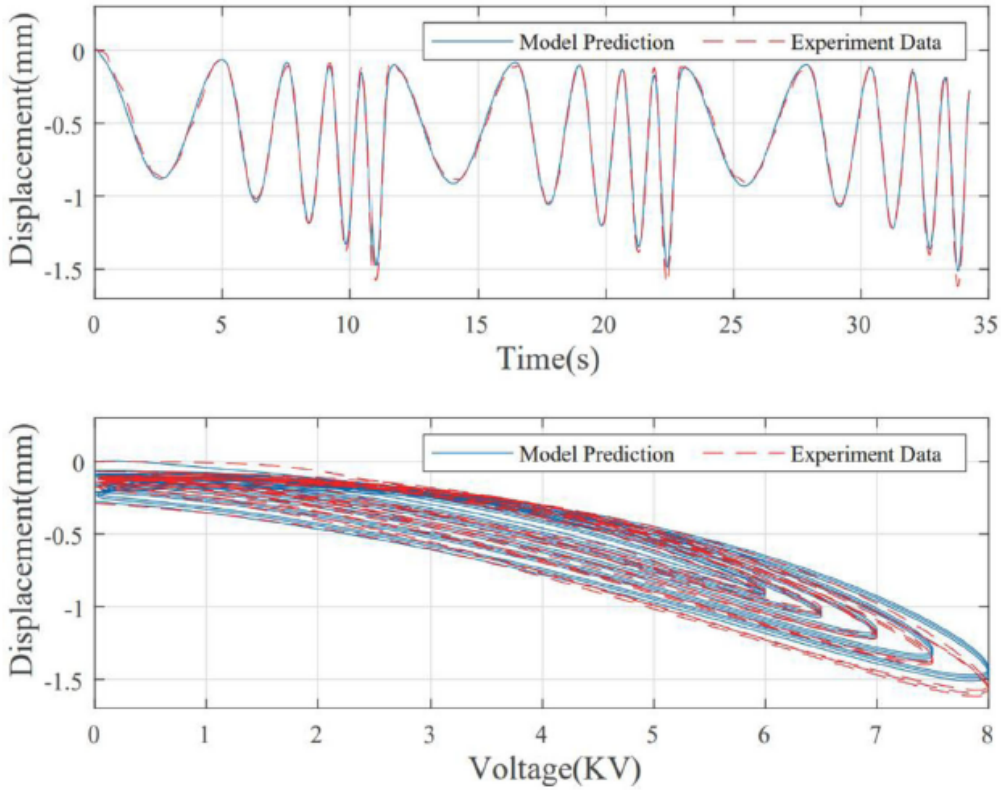

Figure 3.28: Comparison of model output and experimental result with different amplitudes and frequencies.

Model validation with different driving voltage amplitudes

The driving voltage amplitudes are specified as $a_i = 5.5 + 0.5i$ kV, where $i = (1, 2, \ldots, 5)$. Moreover, the frequencies are set as $f_i = 0.2i$ Hz, corresponding to $i = (1, 2, \ldots, 5)$. Consequently, each experimental test involves a driving voltage with varying amplitudes while maintaining a constant frequency.

At frequency values of 0.2 Hz, 0.6 Hz, and 1.0 Hz, the disparities between the model's predicted output and the experimental results are depicted in Figures 3.29–3.31, respectively. Furthermore, Table 3.6 provides an overview of the modeling errors for all the conducted test experiments.

Based on the aforementioned outcomes, it is evident that the root mean-square error of the modeling in each test experiment remains below 8.3%. With the exception of the first dataset, the highest modeling error among all experiments is under 6.9%. Notably, the maximum modeling error becomes more pronounced when the driving voltage frequency is set at 0.2 Hz. This disparity can be attributed to heightened susceptibility to external disturbances in experimental data collection at such low

Table 3.6: Modeling errors across various driving voltage amplitudes

f	e_{rms}	e_m
$f = 0.2Hz$	5.7994%	6.8414%
$f = 0.4Hz$	8.243%	2.6210%
$f = 0.6Hz$	3.5799%	2.4219%
$f = 0.6Hz$	4.9002%	2.6675%
$f = 1.0Hz$	4.9401%	2.3505%

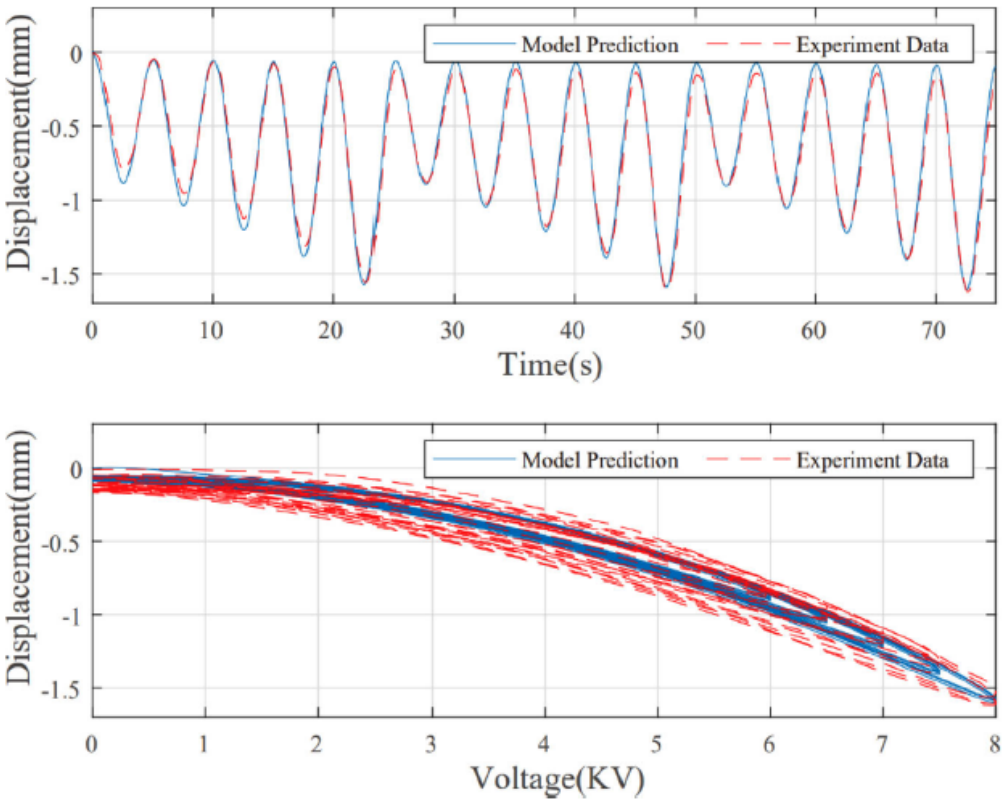

Figure 3.29: Comparison between model output and experimental results at a driving voltage frequency of 0.2 Hz

driving voltage frequencies. Nevertheless, it is crucial to acknowledge that even in the case of this elevated maximum modeling error, the value remains well within permissible limits. Consequently, the proposed dynamic model for the DEA showcases commendable generalization capabilities.

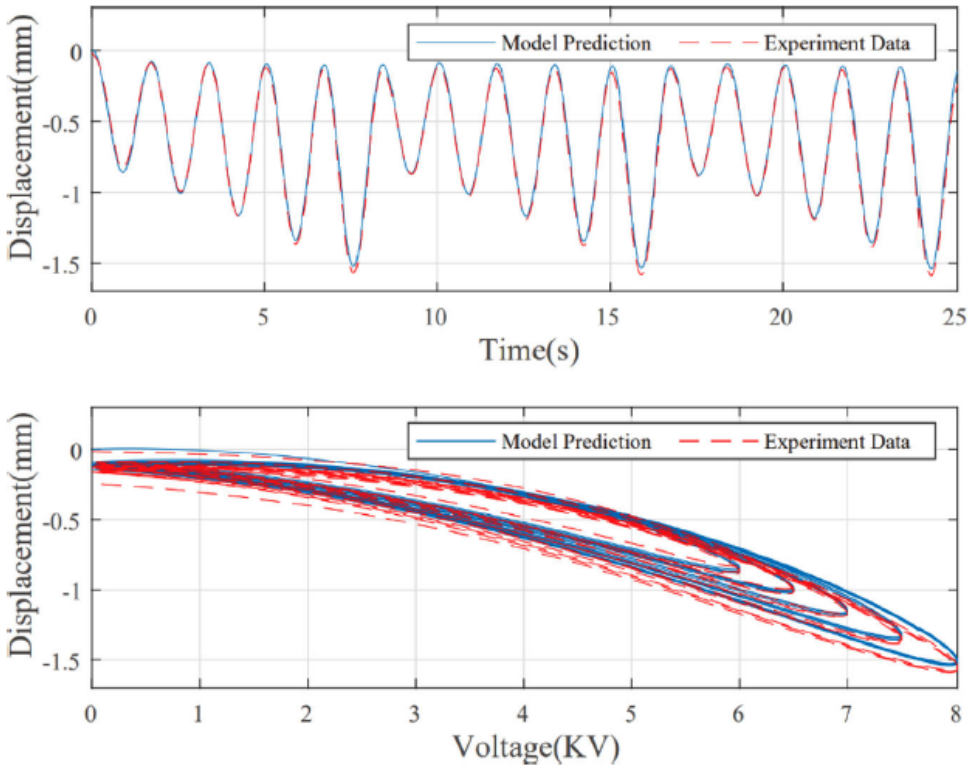

Figure 3.30: Comparison between model output and experimental results at a driving voltage frequency of 0.6 Hz

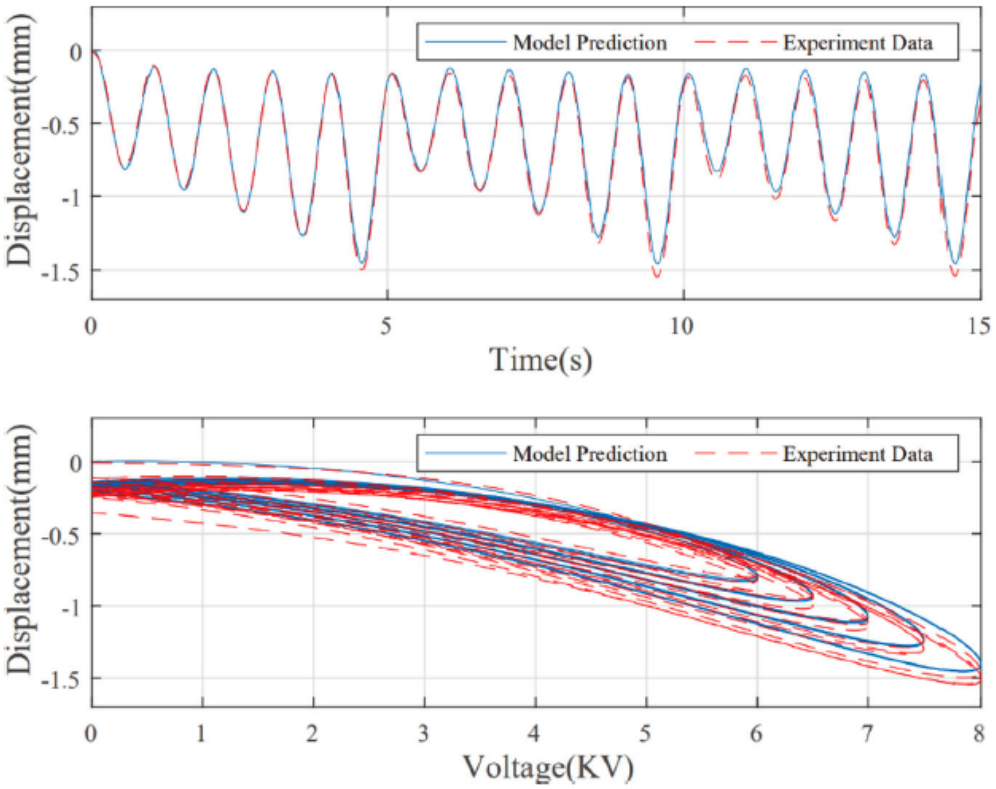

Figure 3.31: Comparison between model output and experimental results at a driving voltage frequency of 1.0 Hz

Validation of the model across varied driving voltage frequencies

The driving voltage amplitudes are established as $a_i = 5.5 + 0.5i$ kV, where $i = (1, 2, \cdots, 5)$. Simultaneously, the frequencies are configured as $f_i = 0.2i$ Hz. Consequently, each test experiment is characterized by driving voltage frequencies of diverse values while maintaining a consistent amplitude.

At amplitudes of 6.0 kV, 7.0 kV, and 8.0 kV, the contrasts between the model's predicted output and the experimental results are depicted in Figs. 3.32-3.34, respectively. Furthermore, Table 3.7 provides an overview of the modeling errors across all test experiments.

Table 3.7: Modeling errors across various driving voltage amplitudes

a	e_{rms}	e_m
$a = 6.0kV$	3.2135%	7.9316%
$a = 6.5kV$	3.1338%	6.9211%
$a = 7.0kV$	3.9176%	7.1493%
$a = 7.5kV$	6.7447%	5.6465%
$a = 8.0kVz$	8.3204%	4.7142%

The root mean square error of the modeling in each test experiment remains below 8.5%, while the highest modeling error among all experiments remains under 8.0%. This reaffirms the broader applicability and effectiveness of the proposed dynamic model.

3.4 Concluding Remarks

Within this chapter, the focus is directed towards two distinct types of Dielectric Elastomer Actuators (DEAs): conical DEAs and planar DEAs. For DEAs, a dynamic model is introduced, underpinned by the framework of nonequilibrium thermodynamics. The chapter begins by elucidating three discrete states inherent to the DEA, followed by a comprehensive analysis of its deformation mechanism.

The subsequent approach involves the implementation of infinitesimal elements possessing both conical and planar geometries, adapted to the respective coordinate systems. This adaptation enables the quantification of the work executed by the inertial force. To effectively encapsulate the elastic energy and viscoelastic attributes of the DEA, the Gent model and the rheological model are harnessed, respectively.

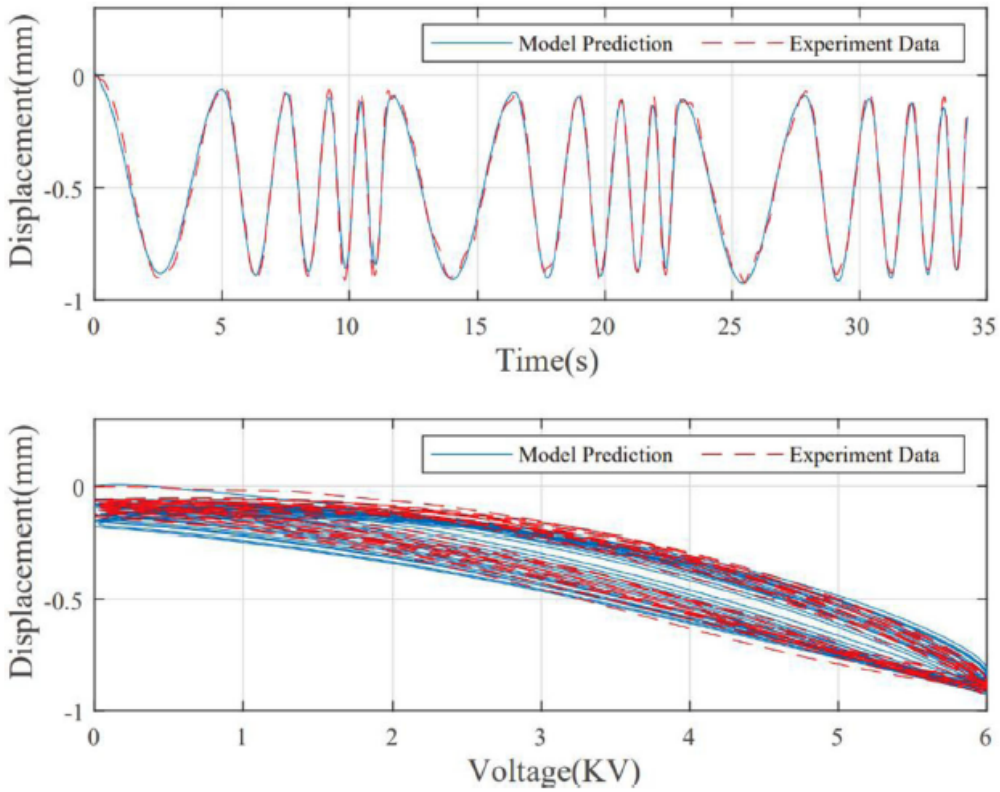

Figure 3.32: Comparison between model output and experimental results at a driving voltage amplitude 6.0 kV

Further advancement entails the identification of unspecified parameters intrinsic to the dynamic model of the DEA, facilitated by the employment of the differential evolution algorithm. Crucially, the chapter culminates in a meticulous comparison between experimental findings and model predictions, reaffirming the efficacy of the proposed dynamic model. This model adeptly captures the inherent complexities, encompassing nonlinearity, intricate electromechanical interactions, and the evolving viscoelastic nature characteristic of DEAs.

Furthermore, empirical observations underscore the DEA's manifest hysteresis tendencies, creep behavior, and even rate-dependent hysteresis occurrences during experimental procedures. The proposed model aptly accommodates these behaviors, underscoring its accuracy in simulating a spectrum of dynamic responses. As such, the dynamic model significantly contributes to the comprehensive comprehension of the intricate motion characteristics exhibited by DEAs.

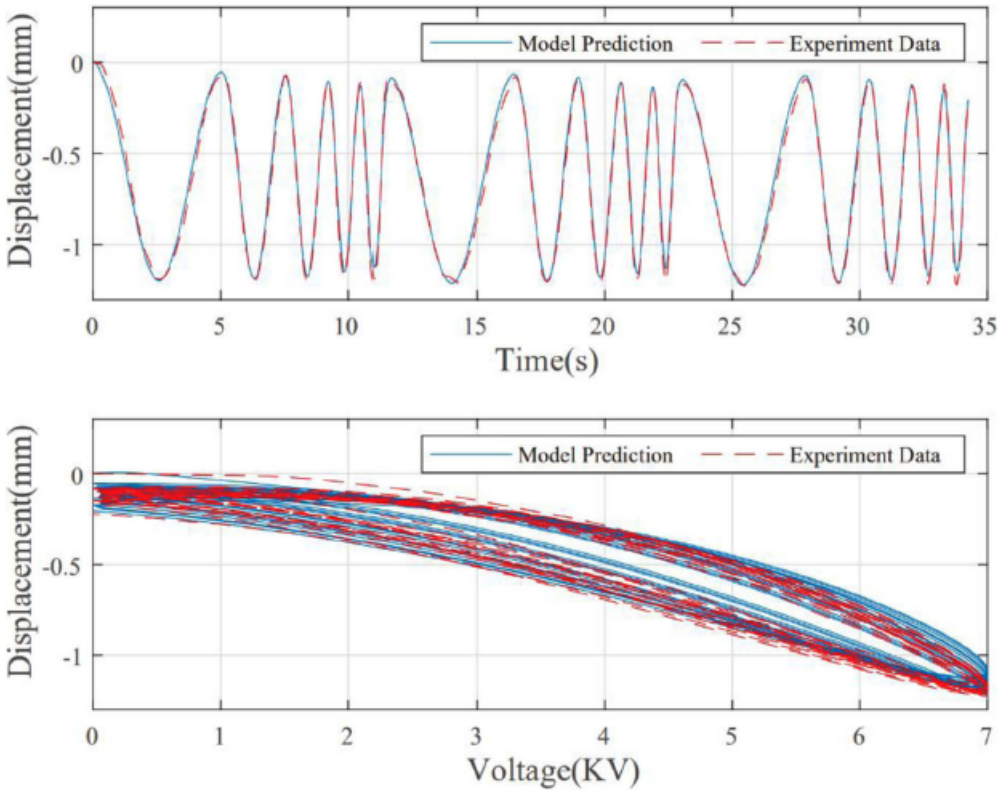

Figure 3.33: Comparison between model output and experimental results at a driving voltage amplitude 7.0 kV

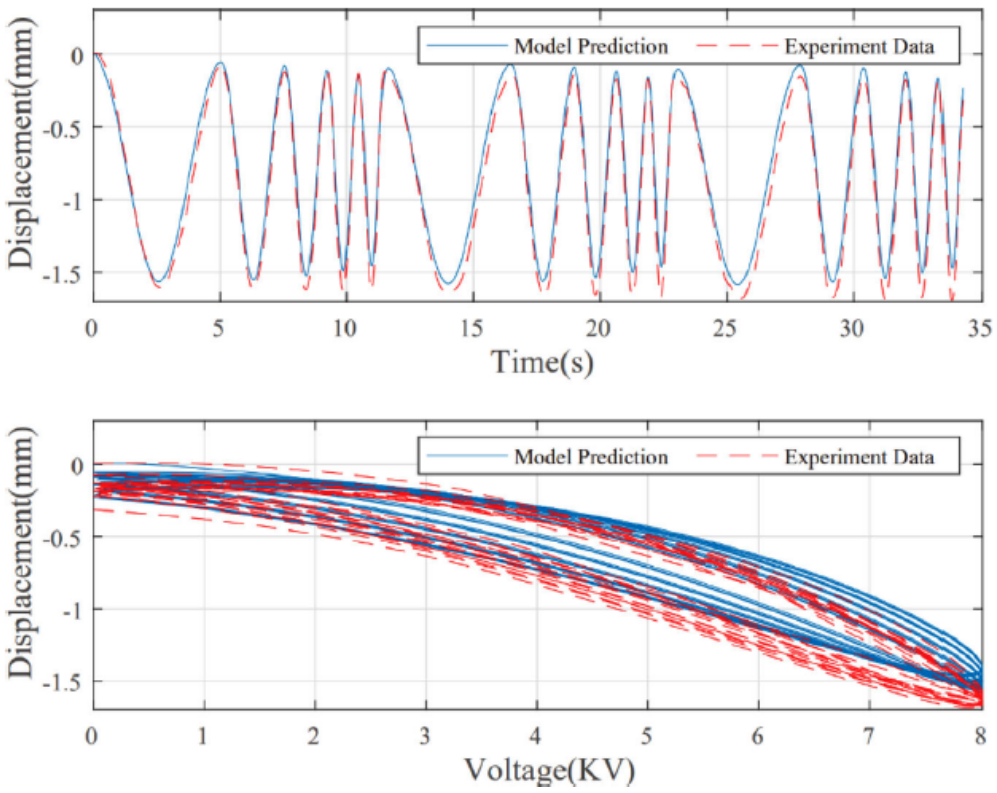

Figure 3.34: Comparison between model output and experimental results at a driving voltage amplitude 8.0 kV

Chapter 4

Data-in-Loop Modeling for Dielectric Elastomer Actuators

4.1 Introduction

The two physics-based models introduced in Chapter 3 effectively encapsulate the intricate behaviors exhibited by DEAs. Nevertheless, these models need the detailed geometric specifications of the DEAs. In real-world applications, DEAs frequently assume diverse shapes and dimensions. Developing bespoke models for each individual actuator is impractical. Consequently, this chapter embarks on a novel approach, drawing inspiration from analogous smart material-based actuators. Herein, a data-in-loop model for DEAs is conceptualized. Notably, this model operates independently of geometric specifics, making it adept at capturing the nuanced nonlinear behaviors inherent to DEAs, even encompassing intricate multi-dimensional dependencies.

4.2 Data-in-Loop Dynamic Model of DEAs

The dynamic model of DEA is proposed in this section, which includes the electrical part, the mechanical part and the electromechanical coupling part.

4.2.1 Electrical Modeling

Following the research results developed in [3], the electrical model of the DEA is built, whose schematic diagram is shown in Fig. 4.1. In Fig. 4.1, q, q_s, q_r, q_c and q_p are the charge of each branch; R_0 is the sum of the external circuit resistance and

the electrode resistance. Considering the DE material is not completely insulated, we use R_L to represent the resistance of the DEA, thereupon $\dot{q}_r$ is the leak current of the DEA. C represents the capacitance of the DEA. M is a virtual driver, which will be introduced in the following subsection; V_A is the voltage across the virtual driver.

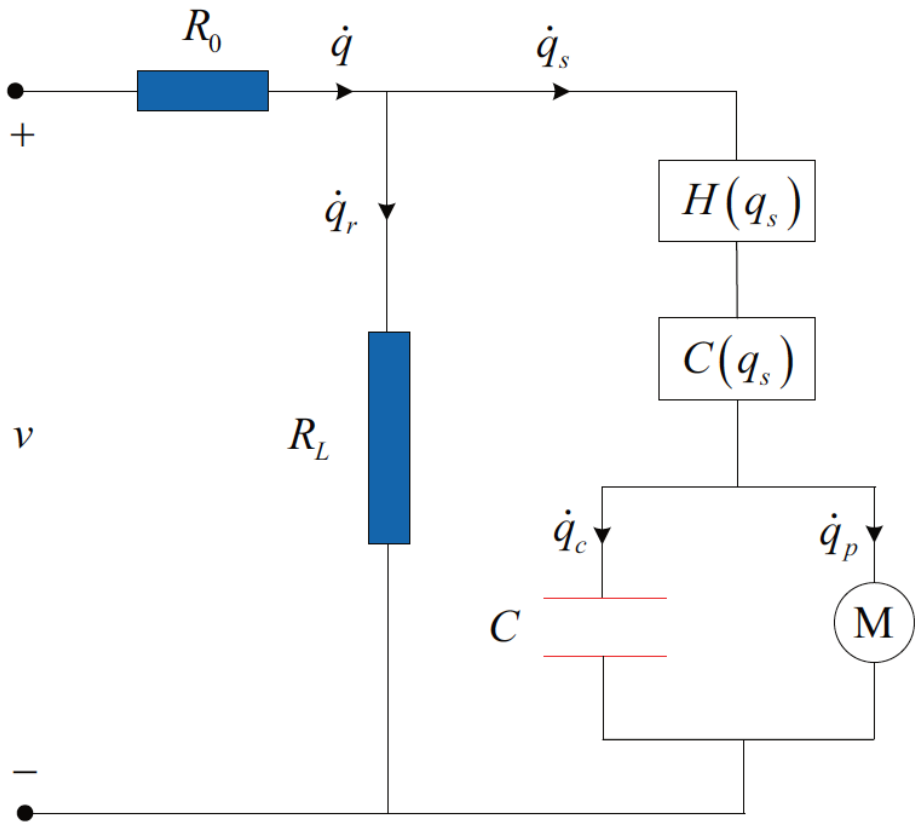

Figure 4.1: Schematic diagram of electrical model

Considering that the complex electrical characteristics of the DEA are different to be described by using the combination of basic electrical components, inspired by the phenomenological modeling method, we add a hysteresis module $H(q_s)$ and a creep module $C(q_s)$ (they will be demonstrated in detail below) to improve the generalization ability and the performance of the model. When these modules are not considered, the proposed electrical model can be reduced to that of [3].

According to Fig. 4.1, the complete electrical equations of the DEA can be expressed as:

$$\begin{cases} R_0\dot{q} + H(q_s) + C(q_s) + \dfrac{q_s - q_p}{C} = v \\ \dot{q} - \dot{q}_s = \dfrac{v - R_0\dot{q}}{R_L} \end{cases} \tag{4.1}$$

which is,

$$\frac{R_0 R_L}{R_0 + R_L}\dot{q}_s + H\left(q_s\right) + C\left(q_s\right) + \frac{q_s - q_p}{C} = \frac{R_L}{R_0 + R_L}v \tag{4.2}$$

4.2.2 Mechanical Modeling

Also following the research results developed in [3], the mechanical model of the DEA is mainly to match its viscoelastic characteristic. In general, there are two famous viscoelastic models, that is, generalized Maxwell model and generalized Kelvin model. Both models use the combination of springs and dampers to describe the viscoelastic behavior, but their combining forms are different. The generalized Maxwell model is shown in Fig. 4.2(a) and the generalized Kelvin model is shown in Fig. 4.2(b).

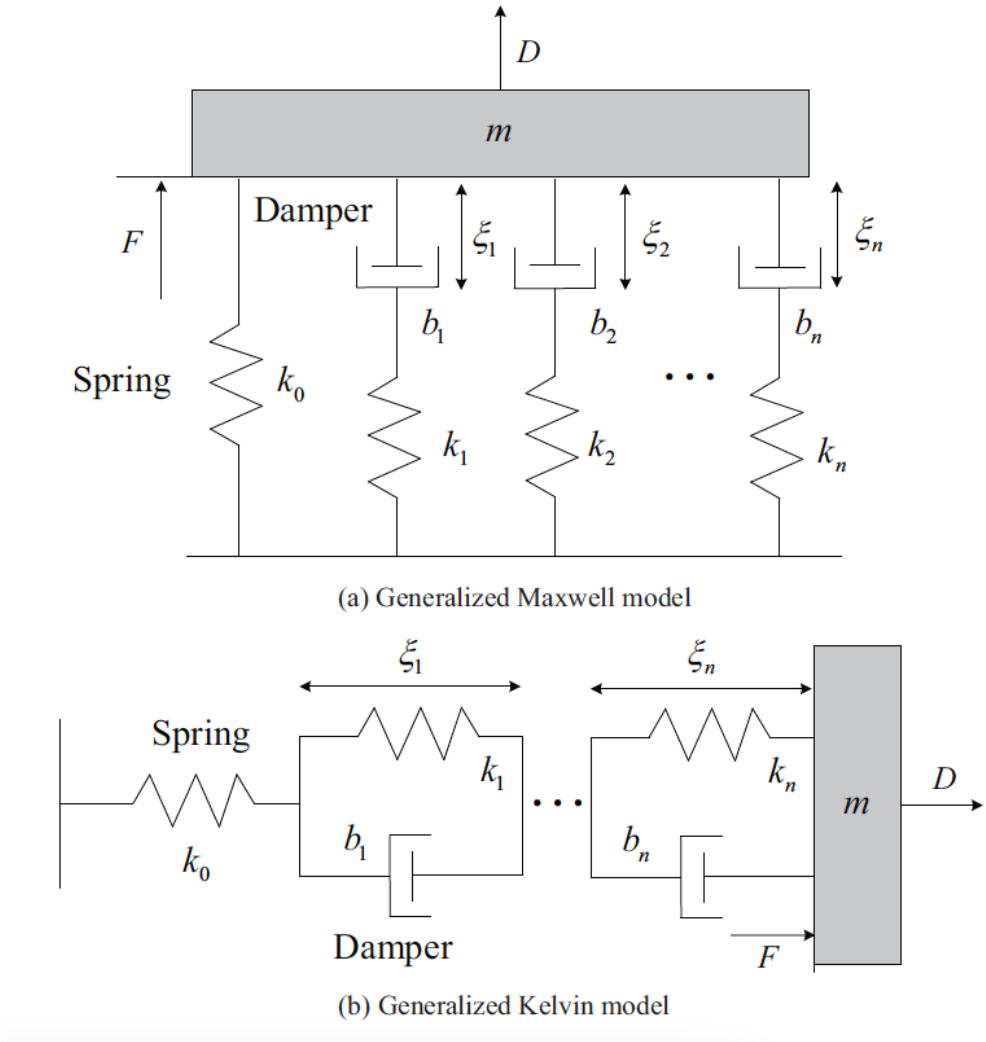

Figure 4.2: Schematic diagram of viscoelastic model

According to Newton's laws of the motion, the dynamic model of the generalized

Maxwell model is

$$\begin{cases} m\ddot{D} = F - k_0 D - \sum_{i=1}^{n} b_i \varepsilon_i \\ b_i \dot{\varepsilon}_i = k_i \left(D - \varepsilon_i \right) \quad (i = 1, 2, \ldots, n) \end{cases} \tag{4.3}$$

where F is the force; k_i is the stiffness factor of each spring; b_i is the damping factor of each damper; ξ_i is the deformation of each damper; m is the weight of the external load.

Moreover, the dynamic model of the generalized Kelvin model can be formulated as

$$\begin{cases} m\ddot{D} = F - k_0 \left(D - \sum_{i=1}^{n} \varepsilon_i \right) \\ b_i \dot{\varepsilon}_i = F - k_i \varepsilon_i \quad (i = 1, 2, \ldots, n) \end{cases} \tag{4.4}$$

4.2.3 Electromechanical Coupling

When the generalized Maxwell model is chosen, the schematic diagram of the electromechanical coupling of the DEA is shown in Fig. 4.3. Meanwhile, the following equations are established.

$$\begin{cases} F = T_{em} V_A \\ q_p = T_{em} D \\ V_A = \dfrac{q_s - T_{em} D}{C} \end{cases} \tag{4.5}$$

where T_{em} is the electromechanical coupling coefficient of the DEA.

The electromechanical coupling shows that the voltage V_A determines the force F and then makes the DEA deform. On the contrary, the displacement of the DEA D has the certain influence on the voltage V_A. So, the electromechanical coupling of the DEA is a bidirectional coupling. By combining (4.2), (4.3) and (4.5), the dynamic model of the DEA can be obtained.

Remark 1. In [3], Maxwell stress is employed to realize the electromechanical coupling of the DEA, whose formula is

$$p = \varepsilon_0 \varepsilon_r \left(\frac{U}{d} \right)^2 \tag{4.6}$$

where p is Maxwell stress; ε_0 is the permittivity of the vacuum; ε_r is the relative permittivity of the DE material; U is the voltage across the DE material; d is the thickness of the DE material.

However, the formula of Maxwell stress is nonlinear, which involves the calculation

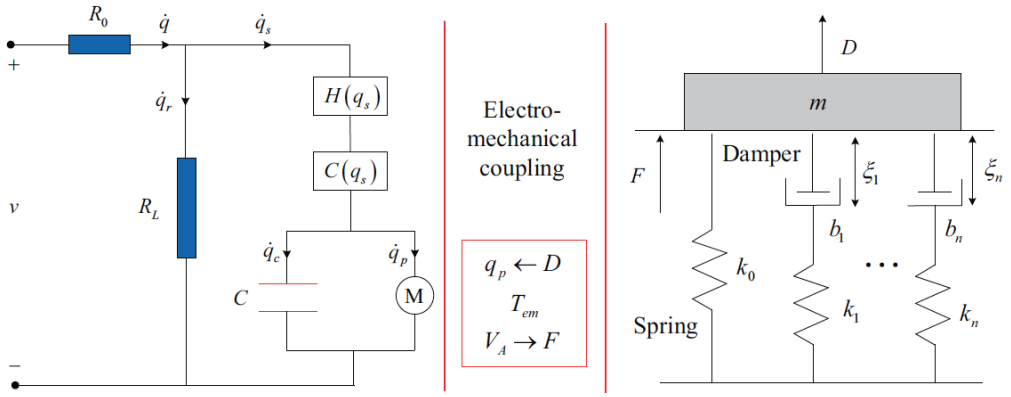

Figure 4.3: Schematic diagram of electromechanical coupling

of the square. Such nonlinear calculation may cause the dynamic model of the DEA become complicated and bring the difficulty to the controller design of the DEA. Thus, we employ the virtual driver with the linear relationship to simplify the dynamic model of the DEA.

4.3 Creep Block

In this section, the creep model based on the mathematical operator is proposed to describe the creep behavior of the DEA [56]. The expression of the creep operator is:

$$\frac{1}{\lambda_i}\dot{y}_i^c(t) + y_i^c(t) = v(t) \tag{4.7}$$

where $\lambda_i > 0$ is the characteristic parameter; $y_i^c(t)$ is the output of the creep operator. Fig. 4.4 shows the input-output relationship of creep operator (4.7).

When the sampling time is T, the digital form of the creep operator (4.7) can be expressed as

$$y_i^c(k) = e^{-\lambda_i T} y_i^c(k-1) + \left(1 - e^{-\lambda_i T}\right) v(k-1) \tag{4.8}$$

Thus, the creep model of the DEA can be formulated to be

$$C(v) = \sum_{i=1}^{n_C} c_i y_i^c[v](t) \tag{4.9}$$

where n_C is the number of the creep operator; c_i is the weighted constant for $y_i^c(t)$.

Since the creep model (4.9) is written as a weighted superposition of many elementary creep operators (4.8) in the time domain, it is convenient to construct an inverse compensator together with the hysteresis compensator based on the P-I

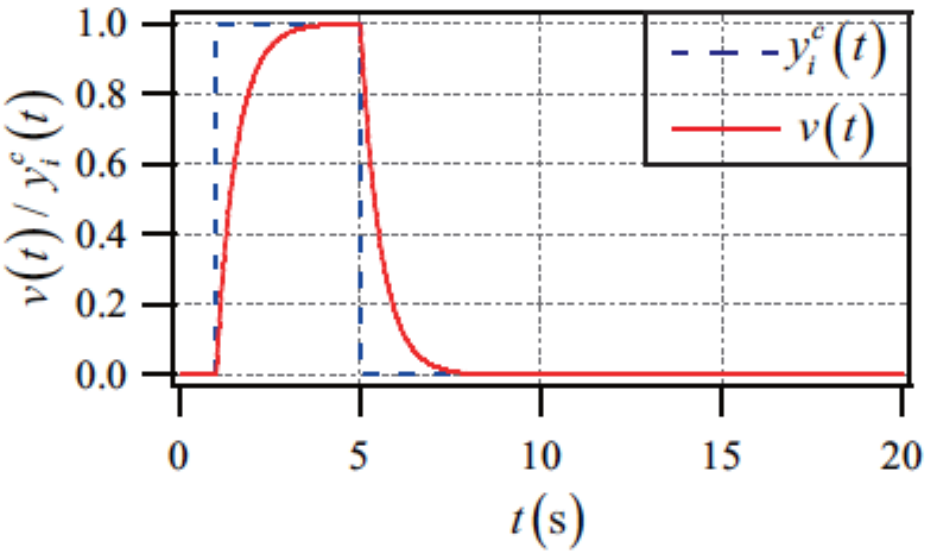

Figure 4.4: Input-output relationship of creep operator (4.7

hysteresis model.

4.4 Hysteresis Block

4.4.1 Introduction to Hysteresis Nonlinearities Models

Hysteresis nonlinearities manifest prominently in actuators founded on smart materials. These nonlinear phenomena present substantial challenges for controller design, as the intrinsic nonlinearity becomes intertwined with the controlled system, leading to unobservable outcomes arising from these nonlinear behaviors. In order to alleviate the constraints imposed by hysteresis nonlinearities, the integration of accurate hysteresis models becomes indispensable.

In the existing body of literature, hysteresis models have been broadly classified into two primary categories: operator-based hysteresis models and differential equation-based hysteresis models, as illustrated in Figure 4.5. Operator-based hysteresis models, which encompass the Preisach model [57], the Prandtl-Ishlinskii (PI) model [58], and the Krasnosel'skii-Pokrovkii (KP) model [59], are formulated by aggregating weighted elementary operators like relay operators, play operators, and KP kernels. These models based on operators demonstrate noteworthy predictive capabilities concerning hysteresis phenomena. Nonetheless, the accuracy of these models is directly tied to the quantity of integrated elementary operators. An

increased number of operators leads to a substantial rise in computational complexity.

On the contrary, the differential equation-based hysteresis models exhibit finite dimensions, thereby requiring a confined set of parameters to govern the magnitude and overall configuration of the hysteresis curve. As a result, these models mitigate the computational intricacies that emerge during the model identification phase. However, the constrained count of model parameters can contribute to significant estimation inaccuracies. In the subsequent sections, we present a succinct overview of both the operator-based hysteresis models and the differential equation-based hysteresis models..

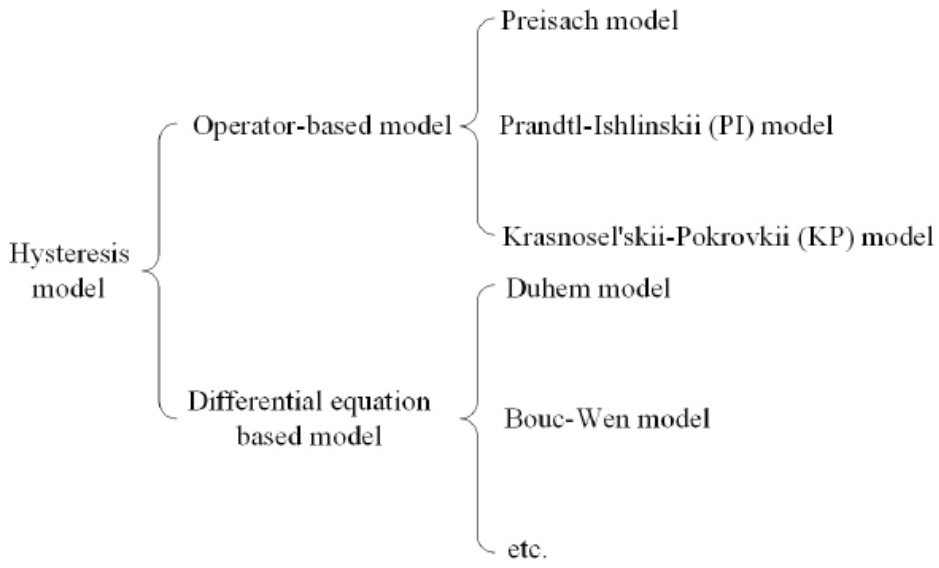

Figure 4.5: Schematic diagram of electrical model

As depicted in Figure 4.5, the prevalent hysteresis models can be categorized into three classes: differential equation-based models, operator-based models, and alternative hysteresis models. This classification is determined by the mathematical methodologies employed within the models. As depicted in Figure 4.5, the prevalent hysteresis models can be categorized into three classes: differential equation-based models, operator-based models, and alternative hysteresis models. This classification is determined by the mathematical methodologies employed within the models.

Differential-equation-based Models

The category of differential equation-based models describes hysteresis nonlinearities through the utilization of differential equations [60]. Among the prominent

representatives of these differential equation-based hysteresis models are the Duhem model, Bouc-Wen model, and Backlash-like model.

Duhem Model: The Duhem model, introduced to characterize magnetic hysteresis nonlinearities [61], portrays the hysteresis phenomenon through an analogy to a mass-spring-damper system. This model can also effectively capture hysteresis in other smart materials. Within the Duhem model framework, the input denoted as v and the corresponding output denoted as w of the hysteresis effect can be expressed as [61]:

$$\dot{w}(t) = f_1(w(t), v(t))\dot{v}_+(t) - f_2(w(t), v(t))\dot{v}_-(t) \tag{4.10}$$

where

$$\begin{cases} v_+ = \frac{|v|+v}{2} \\ v_- = \frac{|v|-v}{2} \end{cases} \tag{4.11}$$

Here, f_1 and f_2 represent the shape functions associated with both the input and output of the hysteresis phenomenon.

Bouc-Wen model: The Bouc-Wen model constitutes a semi-physical extension rooted in the Duhem model (4.10). It was initially introduced by Bouc and subsequently extended by Wen [62]. Within the Bouc-Wen model framework, the hysteresis input denoted as v and the corresponding output denoted as w are formulated as follows:

$$\dot{w} = A\dot{v} - \beta\dot{v}|w|^n - \alpha|\dot{v}||w|^{n-1}w \tag{4.12}$$

where A, α, and β are shape parameters [62].

Backlash-like model: In order to introduce the backlash-like model, it is necessary to present a simplified version of the Duhem model.

$$\frac{dw}{dt} + a|\frac{dv}{dt}|g(v, w) = b\frac{dv}{dt} \tag{4.13}$$

Building upon the foundation of the simplified Duhem model (4.13), a backlash-like model was introduced [63], delineating the hysteresis nonlinearities in the following manner:

$$\frac{dw}{dt} = \alpha|\frac{dv}{dt}|[cv - w] + B_1\frac{dv}{dt} \tag{4.14}$$

where the parameters α, c, and B_1 assume roles as shape parameters. Notably, an explicit solution was furnished in [63], presented as follows:

$$w(t) = cv(t) + d(v(t)) \tag{4.15}$$

Through the utilization of this model, conventional robust controllers can be effectively employed to counteract the hysteresis nonlinearities, obviating the need to construct an inverse model of the hysteresis phenomenon.

In summary, differential equation-based models offer a means to represent hysteresis nonlinearities through first-order differential equations. Nevertheless, obtaining analytical solutions for these equations is challenging, and the development of an inverse compensator for hysteresis nonlinearities grounded in differential equation-based hysteresis models remains elusive.

Operator-based models

Operator-based hysteresis models constitute a category of models that describe hysteresis nonlinearities by means of the integration of hysteresis operators [64]. Presently, they stand as the most prevalent hysteresis models in industrial applications, particularly within the realm of smart material actuators. Based on the specific hysteresis operators employed, the operator-based models encompass the Preisach model [65], Krasnoselskii-Pokrovskii (KP) model [64], and Prandtl-Ishlinskii (PI) model [58].

Preisach Model: The Preisach model is a hysteresis model that relies on the utilization of a relay operator. As illustrated in Figure 4.6, the relay operator $\hat{\gamma}_{\alpha\beta}[v(t)]$ is defined by two thresholds $\alpha > \beta$ and two output states, +1 and -1. The output $w(t)$ remains constant until the input value $v(t)$ crosses either the lower threshold α from below or the upper threshold β from above.

The Preisach model provides a depiction of hysteresis according to [64]: The Preisach model provides a depiction of hysteresis according to [64]:

$$w(t) = P[v](t) = \int\int_{\beta\leq\alpha} \mu(\alpha,\beta)\hat{\gamma}_{\alpha\beta}[v(t)]d\alpha d\beta \tag{4.16}$$

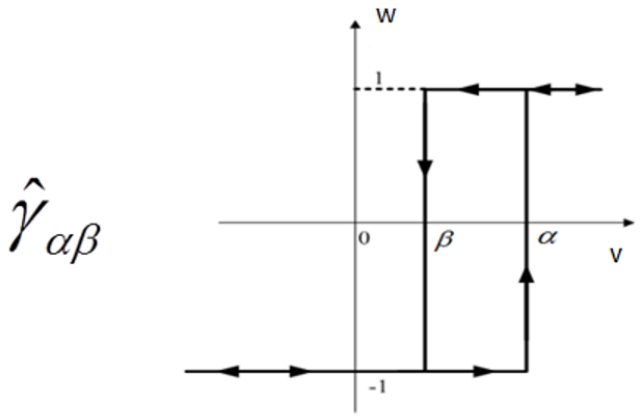

Figure 4.6: Relay Operator

where $\mu(\alpha, \beta)$ is referred to as the weight function or density function, as illustrated in Figure 4.7.

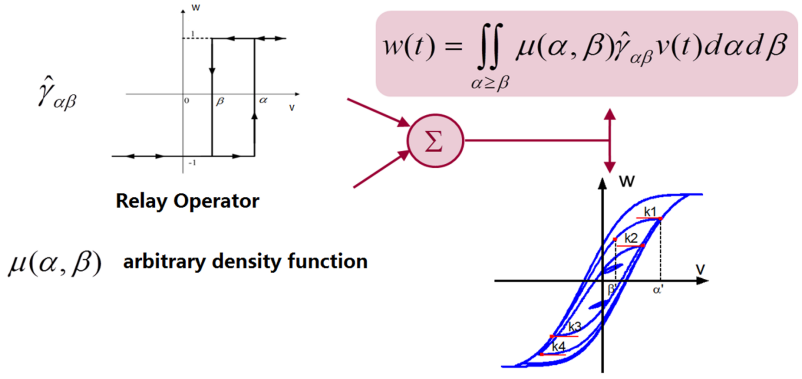

Figure 4.7: Preisach Model

Owing to the presence of the double integral, both parameter identification and the construction of an inverse model pose considerable challenges. Moreover, the inclusion of the control signal v within the integral further complicates the process of controller design.

Krasnoselskii-Pokrovskii (KP) Model: Much like the Preisach model, the Krasnoselskii-Pokrovskii (KP) model is also rooted in the KP operator $k_p[v, \xi(\rho)]$, which can be regarded as an extension of the relay operator [64]. Illustrated in Figure 4.8, the KP model is likewise represented as a double integral of the corresponding

KP operator:

$$w(t) = \Lambda[v](t) = \int\int_{\rho_2 \geq \rho_1} \mu(\rho_2, \rho_1) k_p[v, \xi(\rho)](t) d\rho_2 d\rho_1 \tag{4.17}$$

where $\mu(\rho_2, \rho_1)$ denotes the density function with $\rho = (\rho_2, \rho_1)$. Owing to its resemblance to the Preisach model, the KP model also shares characteristics such as non-invertibility and the inclusion of the control signal within the integral, among others.

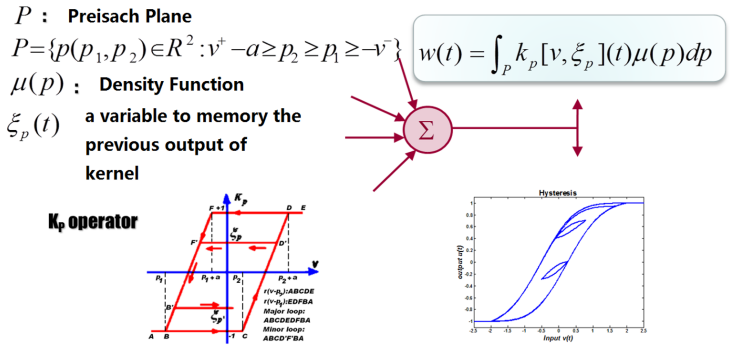

Figure 4.8: Krasnoselskii-Pokrovskii (KP) model

Prandtl-Ishlinskii PI Model: The Prandtl-Ishlinskii (PI) model is constructed by integrating play operators $F_r[v]$ or stop operators $E_r[v]$ [66]. Utilizing the play operator as an illustration, as portrayed in Fig. 4.9, the output of the play operator can be delineated as follows:

$$\begin{cases} w(0) = F_r[v](0) = f_r(v(0), 0) \\ w(t) = F_r[v](t) = f_r(v(t), w(t_i)), \quad for\ t_i < t \leq t_{i+1},\ 0 \leq i \leq N-1 \end{cases} \tag{4.18}$$

with

$$f_r(v, w) = max\{v - r, min\{v + r, w\}\} \tag{4.19}$$

where $0 = t_0 < t_1 < \ldots < t_N = t_E$ constitutes a partition of the interval $[0, t_E]$, characterized by the property that the function v maintains monotonicity within each of the subintervals $[t_i, t_{i+1}]$ [58].

Hence, the Prandtl-Ishlinskii (PI) model grounded in the play operator can be formulated as follows:

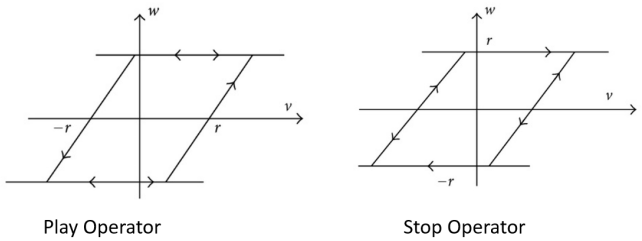

Figure 4.9: Play operator and stop operator

$$w(t) = \Pi[v](t) = p_0 v(t) + \int_0^R p(r) F_r[v](t) dr \tag{4.20}$$

In this equation, $p(r)$ represents the density function, and p_0 stands as a positive parameter.

An inherent advantage of the PI model lies in its avoidance of the non-differentiable relay operator, rendering the PI model invertible. In a study by Krejci [45], an analytical inverse of the PI model was presented. Nonetheless, the PI model is confined to describing symmetric and rate-independent hysteresis phenomena. Ongoing research endeavors focus on expanding the capabilities of the PI model to encompass more complex hysteresis while maintaining its invertibility. Given that this thesis addresses the modified generalized PI model, comprehensive discussions regarding the properties of the PI model and its extensions will be expounded upon in the ensuing chapter.

Other Hysteresis Models

In addition to the differential equation-based and operator-based models, there exist various other phenomenological hysteresis models. Many of these models anticipate hysteresis nonlinearities using intelligent algorithms like Neural Networks [67] and Support Vector Machines [68]. These models can effectively capture hysteresis behaviors in certain specialized domains without resorting to first-order differential equations or hysteresis operators. However, these models haven't achieved the same level of popularity as the differential equation-based and operator-based models.

4.4.2 Hysteresis Structure Selection

Certainly, various models have been developed to capture the hysteresis behavior in nonlinear systems, including the Krasnosel'skii-Pokrovkii model, Bouc-Wen model, Duhem model, Preisach model, and the classical PI model. Among these, the classical PI model stands out for its simple structure and analytical reversibility. Consequently, the PI model is chosen in this study to depict the hysteresis behavior of the DE (Dielectric Elastomer) actuator.

Building upon the classical P-I model, an asymmetric hysteresis model denoted as H_a is formulated to characterize the asymmetric hysteresis nonlinearity inherent in the DE actuator [46]. The formulation of this model is as follows:

$$H_a[v](t) = Q + H_{PI} \tag{4.21}$$

The expression $Q = g_1 v^5(t) + g_2 v^3(t) + g_3 v(t) + g_4 \sqrt[3]{v(t)}$ consists of constant ratios g_1, g_2, g_3, and g_4. Recognizing that the classical P-I model is solely capable of portraying symmetric hysteresis behavior [69], the term Q is introduced to modify the classical P-I model, thereby establishing a novel model capable of representing asymmetric hysteresis nonlinearity. The PI model $H_{PI} = \sum_{i=1}^{n_H} p_i F_{ori} v$ encompasses density coefficients p_i pertaining to $F_{ori}v$, where n_H denotes the count of $F_{ori}v$. Given the positive excitation nature of the DE (Dielectric Elastomer) actuator, the one-sided play operators $F_{ori}v$ featuring thresholds $ori > 0$ are employed [69]. This can be mathematically expressed as:

$$\begin{cases} F_{ori}[v](0) = max\{v(0) - or_i, min\{v(0), 0\}\} \\ F_{ori}[v](t) = max\{v(t) - or_i, min\{v(0), f_{or}[v](t-T)\}\} \end{cases} \tag{4.22}$$

where T represents the sampling time. The characteristics of the one-sided play operator are depicted in Figure 4.10.

4.5 Mechanical Part

In this particular implementation, the simplified Kelvin-Voigt model, depicted in Figure 4.11, can be considered a specific instance of the generalized Kelvin model.

Similar to the conventional spring-damper-mass system, the dynamic equations governing the chosen mechanical component can be expressed as follows:

$$m\ddot{D} + b\dot{D} + kD = F \tag{4.23}$$

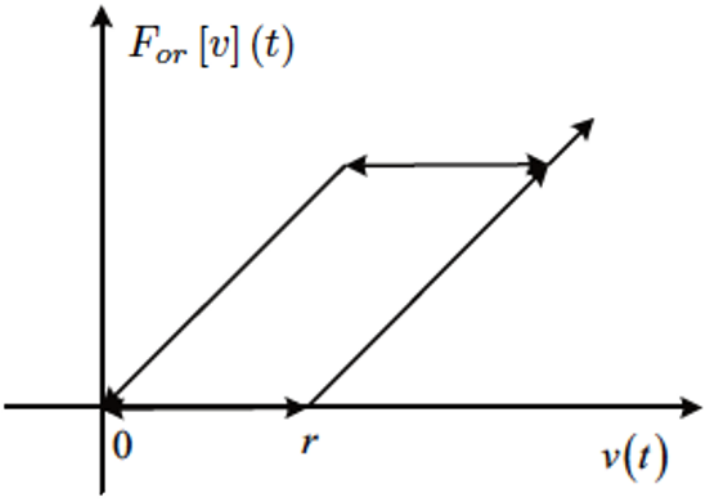

Figure 4.10: Oneside play operator

By combining this equation with the coupling effect characterized by $F = T_{em}V_A$ and $\dot{V}_A = \dot{q}_p/C$, the mechanical and coupling components can be formulated as the following linear equation:

$$\alpha_0 \dddot{+} \alpha_1 \ddot{D} + \alpha_2 \dot{D} + \alpha_3 D = \beta_0 \dot{q}_p = beta_0 HC(t) \tag{4.24}$$

where $HC(t)$ is the output of the nonlinear blocks.

4.6 Parameter Identification

Through the selections detailed in Sections 4.3 to 4.5, the all-encompassing model can be depicted as illustrated in Figure 4.12. The inclusion of a first-order creep structure and an asymmetric PI hysteresis structure were implemented for the nonlinear blocks within the model.

Once more, we employ multi-frequency multi-amplitude voltage signals for the purpose of identification, mirroring the signal employed in Equation (3.25).

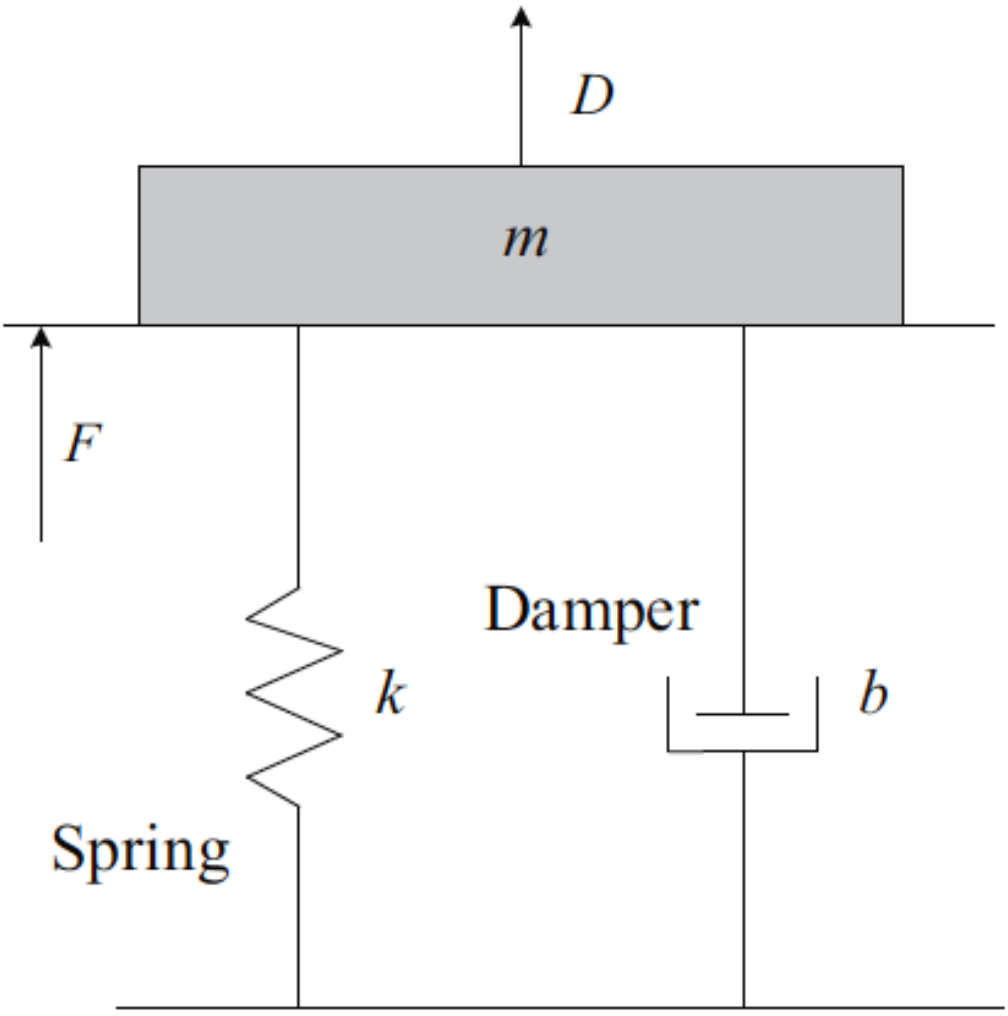

Figure 4.11: Simplified Kelvin-Voigt model

$$
\begin{cases}
t_m = rem(t, \sum_{1}^{5} \frac{1}{f_i}) & \\
v(t_m) = a_1 sin(f_1 \pi t_m), & 0 \le t_m \le 1/f_1 \\
v(t_m) = a_2 sin(f_2 \pi t_m - f_2 \pi / f_1), & f_1 \le t_m \le \sum_{1}^{2} 1/f_i \\
v(t_m) = a_3 sin(f_3 \pi t_m - f_3 \pi \sum_{1}^{2} 1/f_i), & \sum_{1}^{2} 1/f_i \le t_m \le \sum_{1}^{3} 1/f_i \\
v(t_m) = a_4 sin(f_4 \pi t_m - f_4 \pi \sum_{1}^{3} 1/f_i), & \sum_{1}^{3} 1/f_i \le t_m \le \sum_{1}^{4} 1/f_i \\
v(t_m) = a_5 sin(f_5 \pi t_m - f_5 \pi \sum_{1}^{4} 1/f_i), & \sum_{1}^{4} 1/f_i \le t_m \le \sum_{1}^{5} 1/f_i
\end{cases}
\tag{4.25}
$$

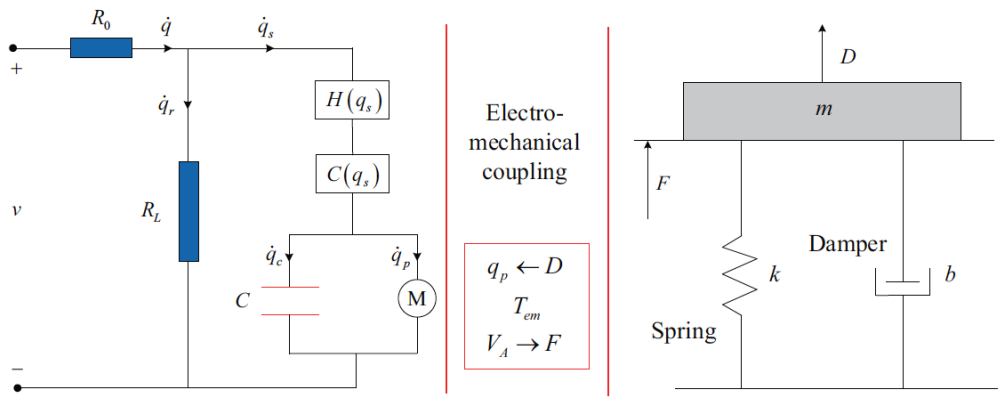

Figure 4.12: Selected DEAs model

Once again, the differential evolutionary algorithm is utilized for parameter identification in the dynamic model. In Equation (4.9), the count of creep operators n_C is set as 3, while the count of one-sided play operators n_H is established at 10. Additionally, the root-mean-square error e_{rms} and the maximum tracking error e_m are introduced as evaluation metrics. Concerning the mechanical part of the identified parameters, $\beta_0 = 3.5692 \times 10^8$, $\alpha_0 = 1$, $\alpha_1 = 37.3570$, $\alpha_2 = 9.1934 \times 10^6$, and $\alpha_3 = 3.4330 \times 10^8$. Further details about the identified parameters can be found in Table 4.1.

Table 4.1: Identified parameters of the data-in-loop model.

i	or_i	p_i	g_i	λ_i	c_i
1	0	0.6859	-5×10^6	4.4731	-0.0085
2	1	0.0419	0.0020	0.0177	-1.0420
3	2	0.0041	-0.6821	0.0177	1.0507
4	3	1×10^4	0.0206		
5	4	2×10^7			
6	5	1×10^7			
7	6	0.0042			
8	7	0.0209			
9	8	0.9654			
10	9	0.4391			

4.7 Model Validation

The effectiveness of the proposed dynamic model for the DE actuator's generalization capability is substantiated through a series of ten comprehensive test experiments.

In the initial five test groups, the driving voltage exhibits varying amplitudes but remains consistent in frequency. Conversely, the subsequent five test groups involve a driving voltage with diverse frequencies while maintaining a consistent amplitude.

The comparative analysis between the model-generated outputs and the empirical data is presented in Figs. 4.13–4.22, wherein the discernible modeling errors are visually depicted. These test results unequivocally affirm the dynamic model's adeptness in accurately characterizing the DE actuator's asymmetric hysteresis, creep phenomenon, and even its rate-dependent hysteresis tendencies.

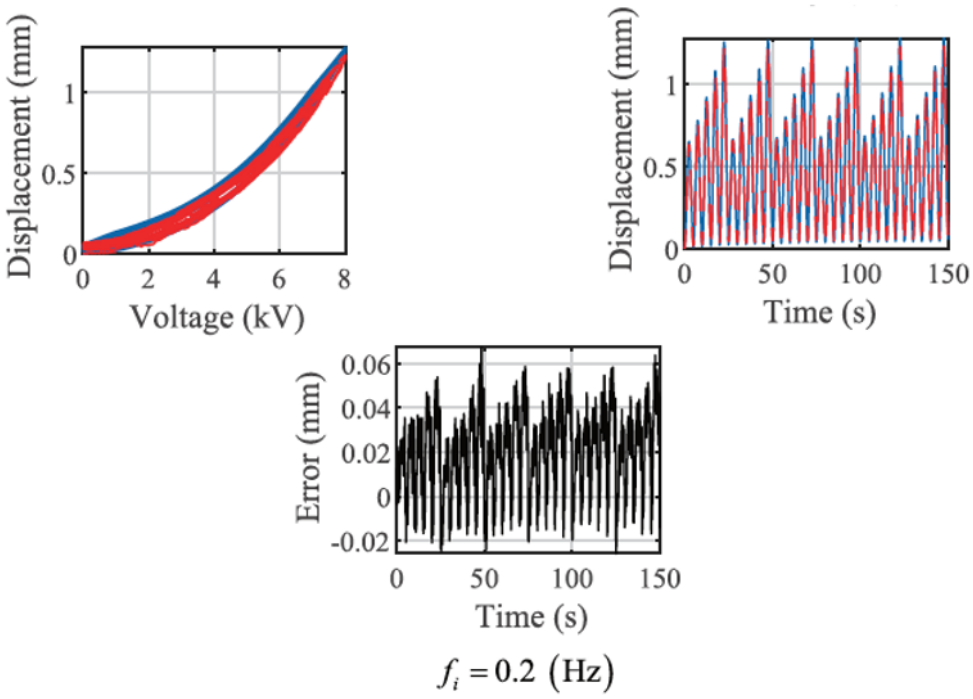

Figure 4.13: Model validation with driving voltage frequency $0.2Hz$

4.8 Concluding Remarks

This chapter presents a dynamic model for Dielectric Elastomer Actuators (DEAs) leveraging a data-in-loop modeling approach. The formulation integrates considerations of DEA structures, along with the introduction of data-in-loop creep and hysteresis blocks. As a result, the dynamic model effectively encompasses asymmetric hysteresis, creep phenomena, as well as both rate-dependent and stress-dependent hysteresis behaviors, concurrently capturing the multifaceted responses of the DEA.

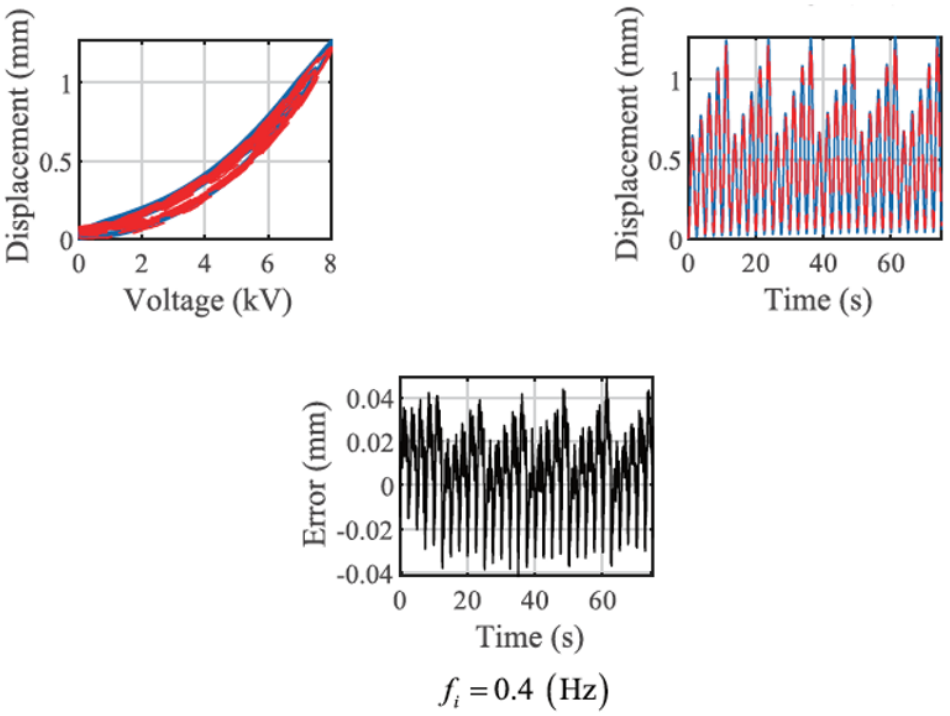

Figure 4.14: Model validation with driving voltage frequency $0.4Hz$

The comparison between empirical experimental results and model-generated outputs underscores the commendable alignment between the dynamic model and the DEA's actual behaviors. The model's composition involves the integration of two nonlinear blocks and a simplified linear system, facilitated by the judicious selection of these aforementioned blocks. Consequently, this dynamic model can be viewed as an initial stride toward formulating a comprehensive control framework. Notably, depending on specific applications, it also furnishes a robust foundation for diverse controller design endeavors.

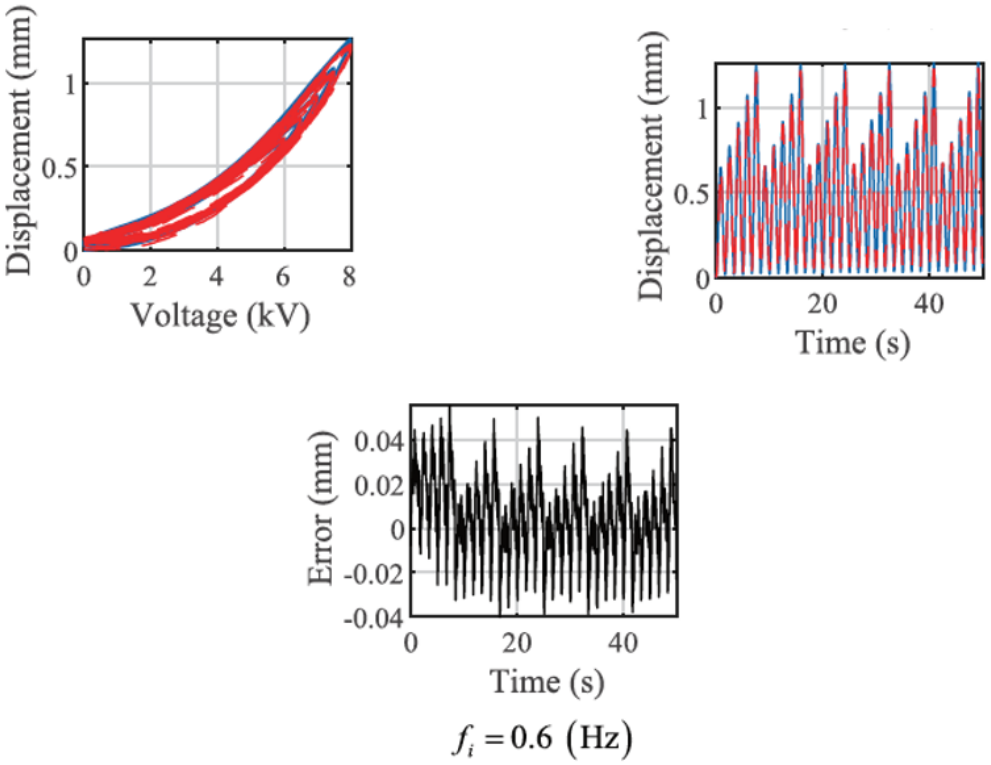

Figure 4.15: Model validation with driving voltage frequency $0.6Hz$

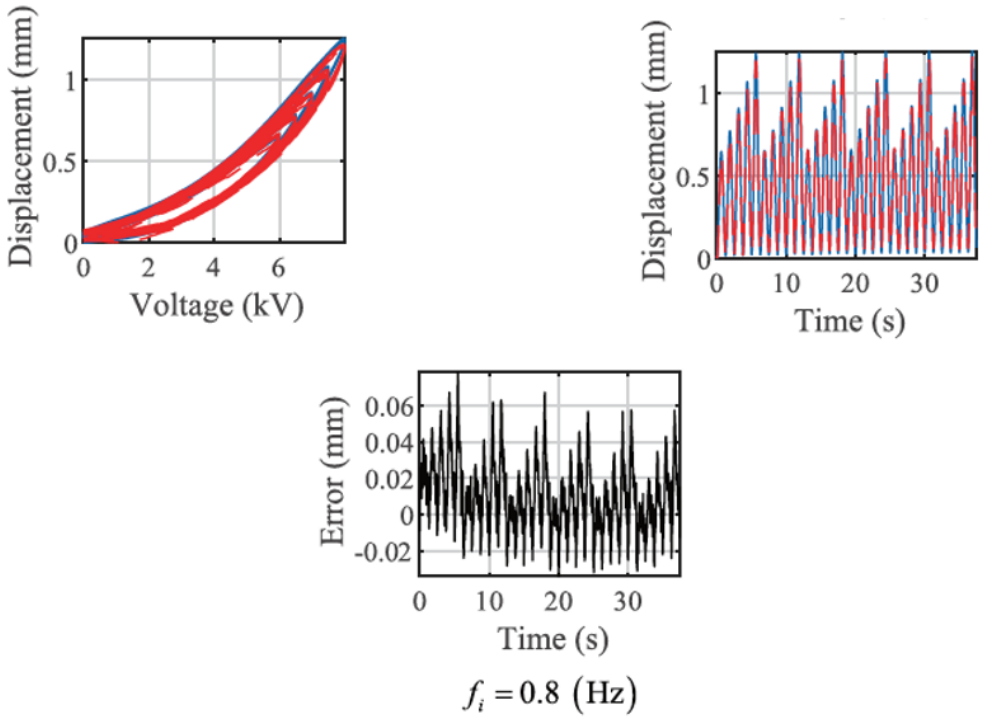

Figure 4.16: Model validation with driving voltage frequency $0.8Hz$

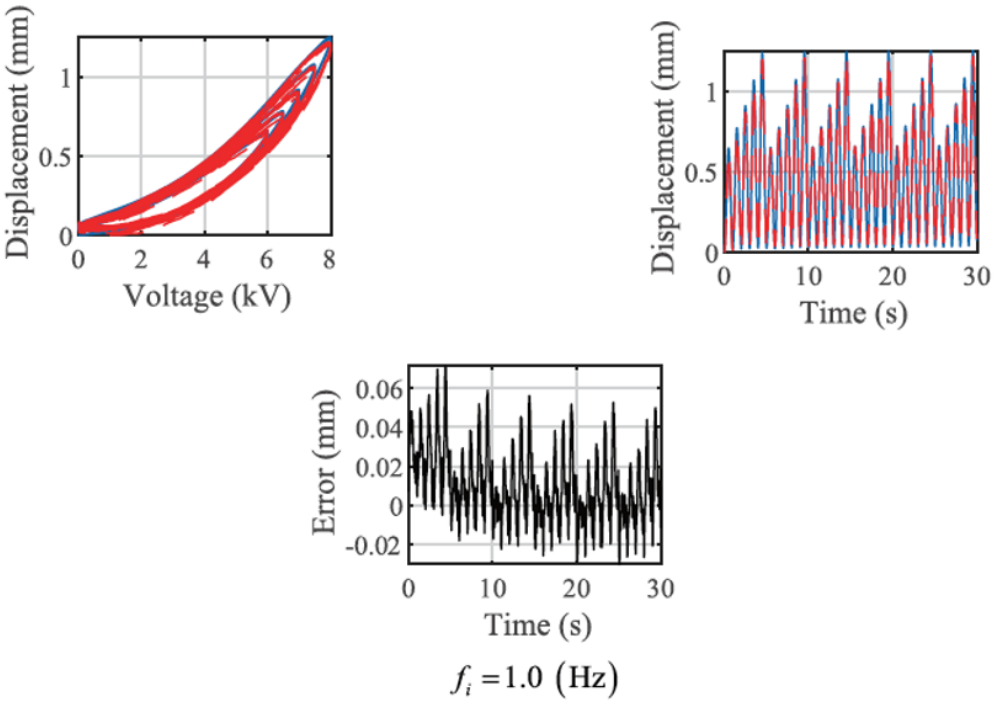

Figure 4.17: Model validation with driving voltage frequency $1.0Hz$

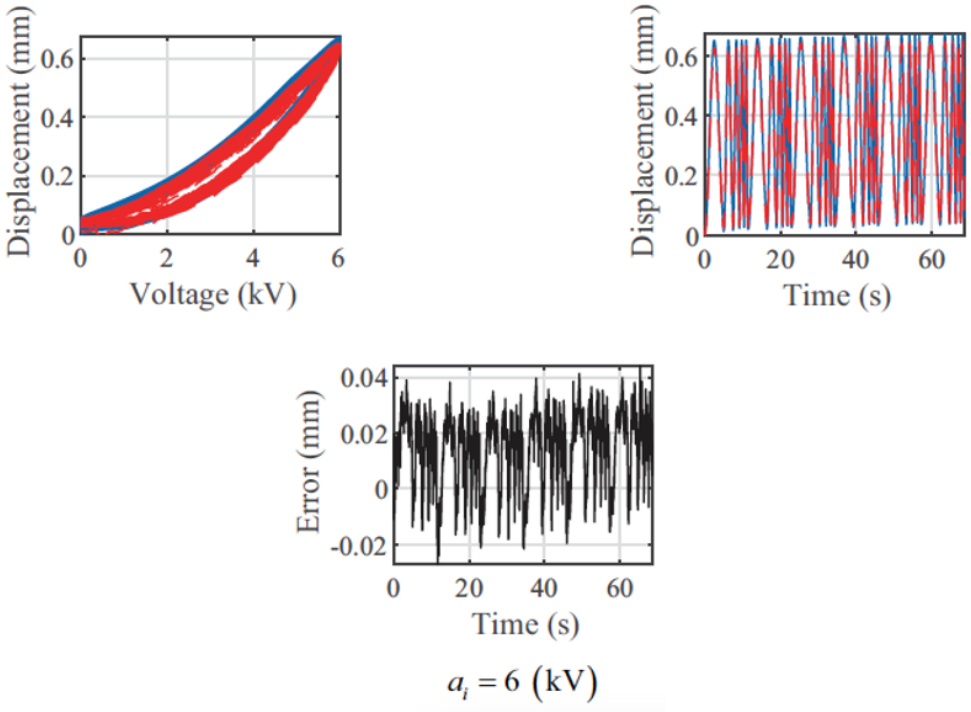

Figure 4.18: Model validation with driving voltage amplitude 6.0 kV

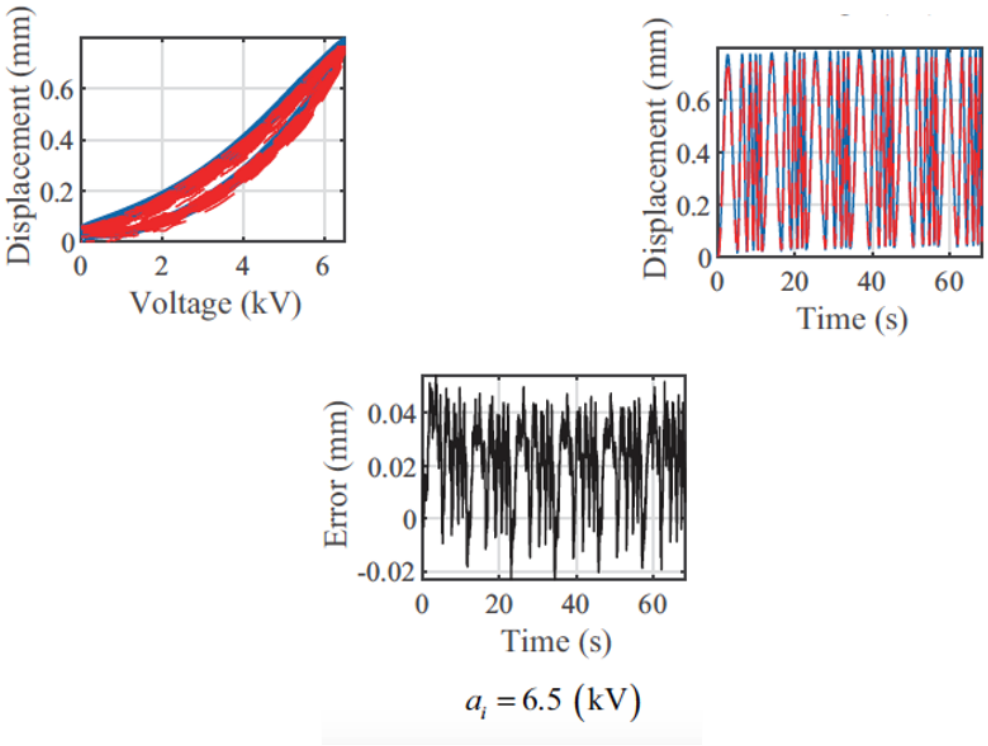

Figure 4.19: Model validation with driving voltage amplitude 6.5 kV

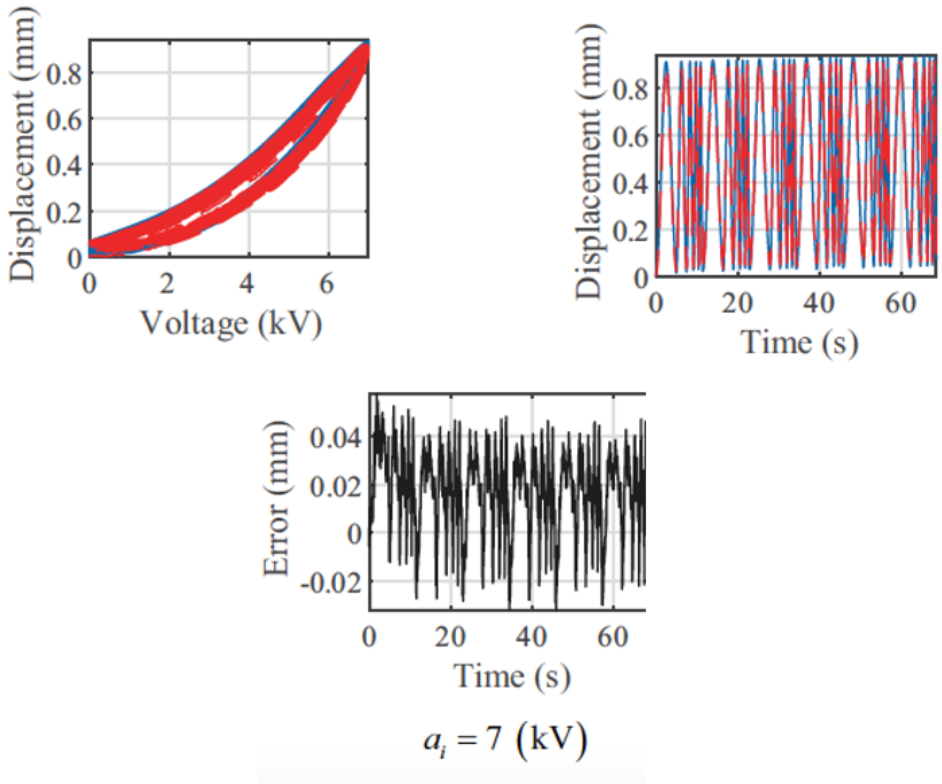

Figure 4.20: Model validation with driving voltage amplitude 6.0 kV

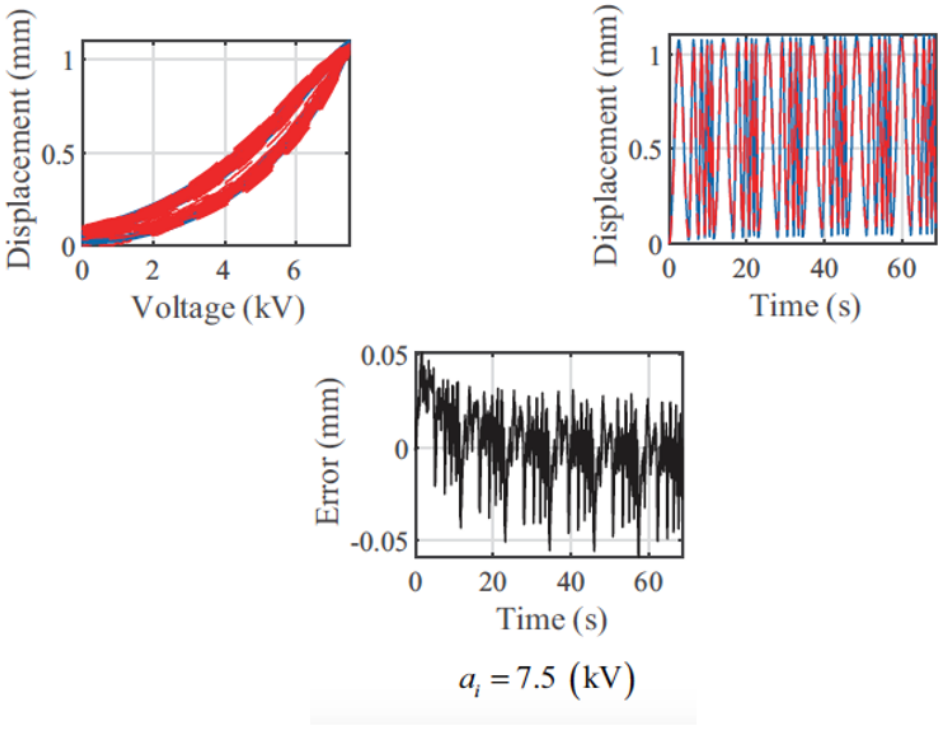

Figure 4.21: Model validation with driving voltage amplitude 6.5 kV

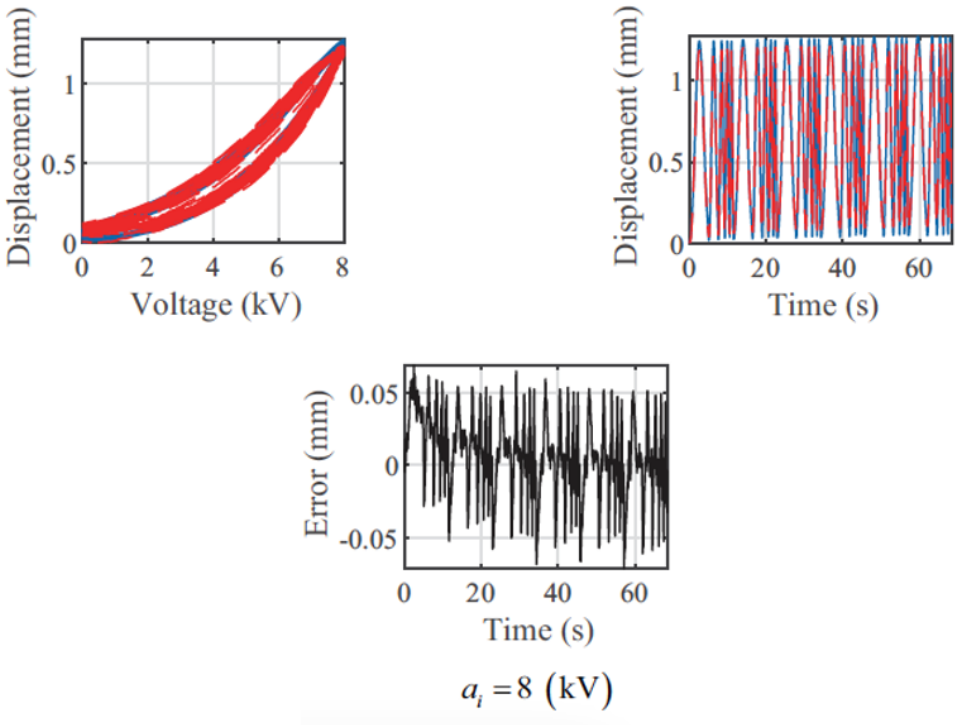

Figure 4.22: Model validation with driving voltage amplitude 8.0 kV

Chapter 5

Control Approach for Dielectric Elastomer Actuators with data-in-loop Model

5.1 Introduction

In Chapter 4, we propose an encompassing data-in-loop model tailored to elucidate the intricate nonlinear and dynamic characteristics inherent in Dielectric Elastomer Actuators (DEAs). Our empirical findings underscore the emergence of undesirable and deleterious effects stemming from these nonlinear behaviors, with particular emphasis on the pervasive influence of hysteresis. These effects have the potential to engender performance degradation in DEAs, thereby introducing inaccuracies and oscillatory tendencies. Consequently, this chapter meticulously directs its focus toward the formulation of a cascading model framework. Within this framework, a dynamic component precedes a hysteresis model. The overarching objective of this endeavor is the conception and implementation of a robust adaptive controller, strategically fortified to mitigate these challenges and ensure steadfast performance. In this chapter, we will focus on the development of a model-based Adaptive Robust Control (ARC) approach for the trajectory control of DEAs.

To facilitate the practical implementation of the algorithms on physical actuators, certain assumptions were deemed necessary for the specific application:

1. Given the inherent complexity and parameter abundance characterizing the physics-based models expounded in Chapter 3, these models are not suitable for controller design purposes. Consequently, the development of control strategies

is based on the data-in-loop model presented in Chapter 4.

2. Given the use of Polydimethylsiloxane (PDMS) materials, the creep effect is deemed insignificantly pronounced. We treat this nonlinearity as external disturbances and potential system parameter drift.

3. It is worth noting that the control of input-quadratic nonlinear systems remains a formidable challenge within the control community [42]. In the context of this application, we handle the square of the voltage, denoted as V^2, as virtual control signals.

5.2 Problem Statement

Based on the aforementioned premise, the data-in-loop model developed in Chapter 4, as illustrated in Fig. 4.12, can be further simplified. In Fig. 5.1, we adopt the square of the voltage, denoted as $v(t) = V^2$, as the system input. The hysteresis block, represented by $w(t) = \Pi[v](t)$, effectively captures the inherent hysteresis nonlinearity observed in Dielectric Elastomer Actuators (DEAs). The mechanical component is treated as a linear system, amenable to parameterization as $\varphi(x)^T\theta$. Notably, the creep effect can be construed as either external disturbances or perturbations occurring in the system parameters θ. For the purposes of controller design, we duly consider them as bounded disturbances, denoted as Δ.

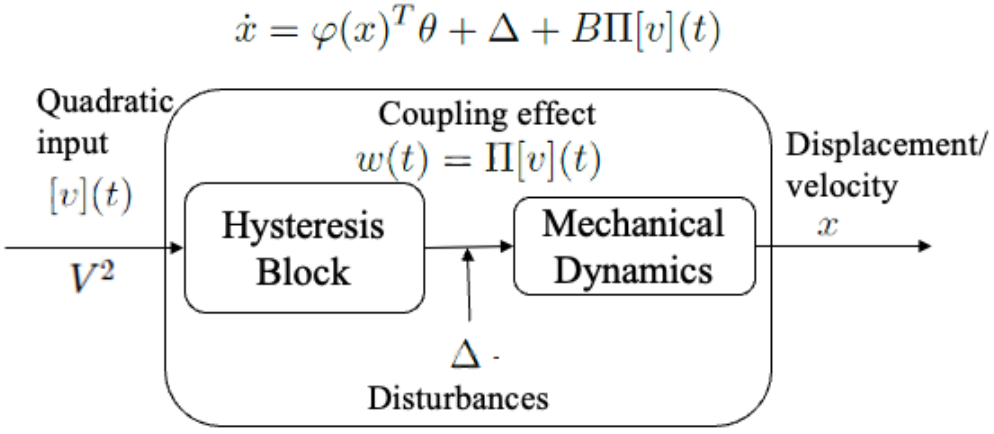

Figure 5.1: Simplified DEA model with assumptions

Based on the simplified model, the behaviors of the DEAs can be characterized as:

$$\dot{x} = \varphi(x)^T\theta + \Delta + B\Pi[v](t) \tag{5.1}$$

Here, x denotes the state of the dynamic system, θ encapsulates the parameter vector of the system, and $\varphi(x)$ represents the associated regressor. The majority of nonlinear dynamic systems can be effectively cast within this structural framework [70]. In this context, Δ signifies the disturbance, B pertains to the actuation parameter, and $w(t)$—as introduced coupling effects.

The system's schematic overview is depicted in Figure 5.2. The primary goal revolves around devising a controller $v(t)$ that orchestrates the system's state x to trace the reference trajectory x_d.

The pursuit of tracking control for such systems poses substantial challenges, attributed to the following factors:

1. Coupled dynamics and actuator hysteresis: In practical scenarios, the system dynamics are intricately intertwined with the behavior of actuators, which inherently exhibit hysteresis effects. Consequently, the measurement of the actuator's output, denoted as w and serving as the input to the dynamics, remains elusive.

2. Complex hysteresis nonlinearities: The hysteresis phenomena manifest as intricate and nonlinear behaviors. Confronting and mitigating the adverse consequences of this effect poses considerable difficulty.

3. Unknown dynamic parameters: Often, the system's dynamic parameters are uncharted territory. Designing controllers for systems with such limited information is a nontrivial task.

4. Disturbance consideration: Incorporating disturbances into the control scheme for these systems further compounds the challenge. Existing controller design methodologies may not readily accommodate this requirement.

5.3 Prandtl-Ishlinskii (PI) Hysteresis Model

To tackle this intricate issue, the exploration necessitates the establishment of a model that aptly characterizes the hysteresis nonlinear effect. Currently, available hysteresis models can be broadly classified into two categories: physics-based models and phenomenological models [61].

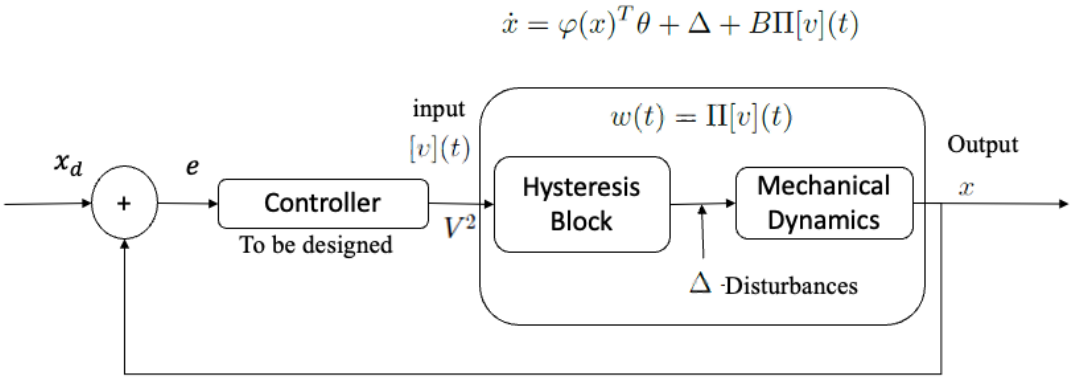

Figure 5.2: Structure of the control problem for DEAs

Physics-based models are derived from the foundational physics principles or phenomena. Notable examples encompass the Jiles-Atherton (J-A) Model [71] and the domain wall model [72], both rooted in underlying physical mechanisms.

Operator based models stem from input-output relationships of hysteresis behaviors, often neglecting certain intricate physics details. This category encompasses models such as the Duhem model [61], the Backlash-like model [63], and the Prandtl-Ishlinskii model (PI model) [58], among others.

Among the multitude of hysteresis models that have been proposed, the Prandtl-Ishlinskii (PI) model has emerged as particularly prominent. This model's allure lies in its possession of an analytical inverse [45], a quality that bestows substantial advantages upon controller design tailored to actuators grappling with hysteresis effects. In the context of this paper, the PI model is chosen as the framework to depict the hysteresis exhibited by actuators. The research endeavors will pivot on the integration of this model with adaptive robust control techniques [73], aimed at mitigating the limitations imposed by this nonlinear effect.

5.3.1 Play Operator

The Prandtl-Ishlinskii (PI) model belongs to the category of phenomenological models. It characterizes hysteresis behavior through the incorporation of fundamental hysteresis operators. Among these, two of the most widely recognized operators are the play operator and the stop operator.

As illustrated in Figure 5.3, both of these fundamental operators exhibit memory effects with a specified threshold denoted as r. To maintain a general perspective,

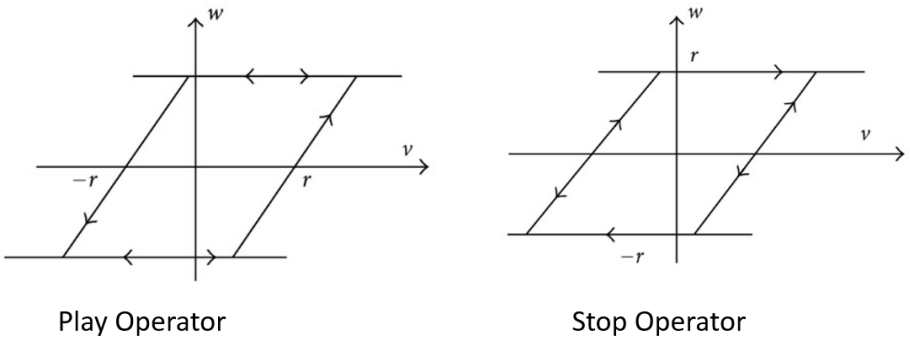

Figure 5.3: Play operator and stop operator

the remainder of this paper will center its attention on the play operator and the Prandtl-Ishlinskii (PI) model formulated on the foundation of play operators.

The conduct exhibited by the play operator, depicted in Figure 5.3, can be delineated as follows:

$$\begin{cases} w(0) = & F_r[v](0) = f_r(v(0), 0) \\ w(t_{i+1}) = & F_r[v](t_{i+1}) = f_r(v(t_{i+1}), w(t_i)), \\ & for\ t_i < t \leq t_{i+1},\ 0 \leq i \leq N-1 \end{cases} \tag{5.2}$$

with

$$f_r(v, w) = max\{v - r, min\{v + r, w\}\} \tag{5.3}$$

In this context, the symbols hold the following meanings:$v(t)$ represents the input signal, $w(t)$ signifies the output signal, $[0, t_E]$ denotes a domain encompassing monotone continuous functions [58], $w(0)$ stands for the initial output, The subsequent output of the operator hinges on the latest output $w(t_i)$.

5.3.2 Prandtl-Ishlinskii Model

Drawing upon the play operator elucidated in Section 5.3.1, the foundation is laid for the play operator-based Prandtl-Ishlinskii model. Notably, Prandtl's work [74] has presented a formula conducive to describing hysteresis behavior, as detailed below:

$$w(t) = \Pi[v](t) = p_0 v(t) + \int_0^R p(r) F_r[v](t) dr \tag{5.4}$$

where p_0 stands as a positive parameter, $p(r)$ denotes a continuous density function, adhering to the conditions $p(r) > 0$ and $\int_0^\infty rp(r)dr < \infty$. It's noteworthy that $p(r)$ diminishes as r becomes sizable, thus warranting the introduction of an upper integration limit R for practicality [58].

In practical applications, PI models are commonly employed in their discrete form:

$$w(t) = \Pi[v](t) = p_0 v(t) + \sum_{i=1}^{n} p(r_i) F_{ri}[v](t) \tag{5.5}$$

where n signifies the count of engaged play operators, $p(r_i)$ represents a sequence of weights associated with the play operators, $F_{ri}v$ corresponds to the outputs of the fundamental operators involved.

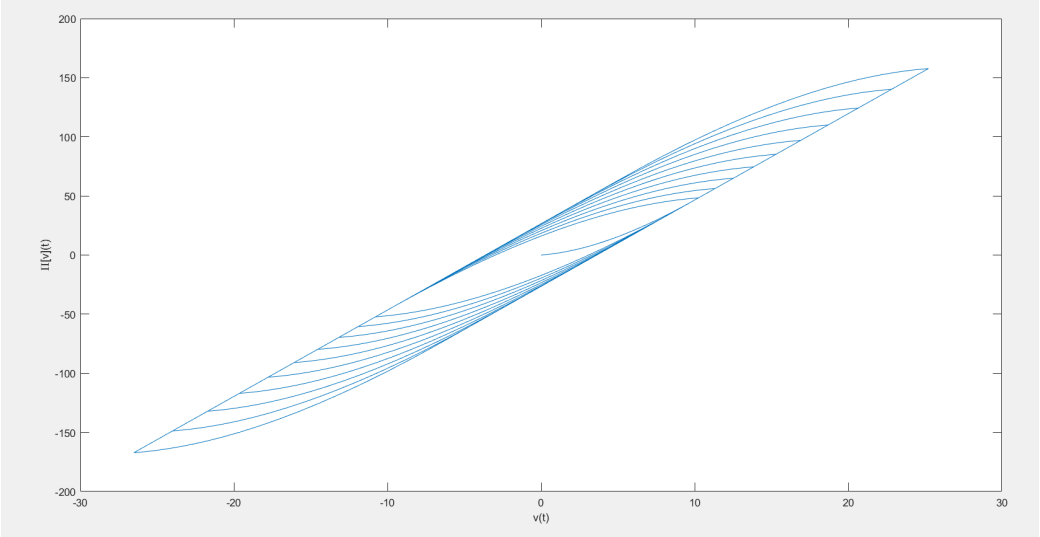

Figure 5.4: Hysteresis nonlinearities described by PI model

In Figure 5.4, the depicted plot elucidates the input-output correspondence of a PI model. For this instance, the parameters were configured as follows: $p_0 = 1$ and $p(r) = e^{-0.1r}$. The initial value was designated as $w(0) = 0$.

5.3.3 Some Advantages of PI Model

The PI model stands as a preeminent choice among hysteresis models, finding extensive application across diverse realms of research and industries. This popularity can be attributed to its distinct attribute of possessing an analytical inverse. Furthermore, a decomposition method for the discrete PI model was put forth in [75]. This model assumes a representation akin to the dot product involving a vector

of fundamental play operators and a vector of weights. Capitalizing on these valuable characteristics, the development of an adaptive robust controller becomes feasible for addressing the intricate challenges presented by this system.

5.3.3.1 Inverse Prandtl-Ishlinskii Model (Inverse PI Model)

Among the numerous hysteresis models, the PI model and certain variations thereof stand out due to their valuable characteristic of possessing an analytical inverse. Notably, [45] has furnished an analytical methodology for constructing the inverse of the PI model. This feat was accomplished by leveraging the initial loading curve inherent to the PI model.

$$\Omega(r) = p_0 r + \int_0^r p(\epsilon)(r-\epsilon)d\epsilon \tag{5.6}$$

The construction of the inverse PI model is facilitated by the input-output relationship, wherein $\dot{\Omega}(0) = p_0$ and $\ddot{\Omega}(r) = p(r)$ hold true. By mirroring the loading curve along the line $y = x$, the inverse PI model is effectively established. As a consequence, the new threshold for the operators featured within the derived inverse model can be determined:

$$s_i = p_0 r_i + \sum_{j=1}^{i} p(r_j)(r_i - r_j) \tag{5.7}$$

where r_j represents the thresholds of the play operators within the PI model, triggered by the loading curve, s_i signifies the thresholds of the play operators within the inverse model. Having established these relationships, the groundwork is laid for constructing the inverse PI model:

$$\Pi^{-1}[v](t) = \dot{\Omega}^{-1}(0)v(t) + \int_0^{\infty} \ddot{\Omega}^{-1}(s)F_s[v](t)ds \tag{5.8}$$

where $\Omega^{-1}v(t)$ signifies the inverse loading curve, and its computation is accomplished through the following expression:

$$\dot{\Omega}^{-1}(0) = \frac{1}{p_0} \tag{5.9}$$

and

$$\ddot{\Omega}^{-1}(s_i) = \frac{p_i}{(p_0 + \sum_{j=1}^{i} p(r_j))(p_0 + \sum_{j=1}^{i-1} p(r_j))} \tag{5.10}$$

In most previous research and practical applications, the identification of hysteresis parameters has been a prerequisite for the development of an inverse model.

This necessitated an offline approach, established prior to deployment. However, the novel implementation presented in this paper harnesses adaptive control techniques, enabling the online estimation of hysteresis density functions. As a result, the inverse model can be formulated and dynamically updated during the course of the control task. This progressive approach will be expounded upon in the subsequent sections detailing the controller design.

5.3.3.2 Decomposition of Discrete Prandtl-Ishlinskii Model

As stated in the previous subsection, the discrete PI Model entails the integration of multiple fundamental play operators. Consequently, the actuator's output $w(t)$ can be aptly depicted in the following manner:

$$\begin{aligned} Bw(t) &= B\Pi[v](t) \\ &= B(p_0 v(t) + \sum_{i=1}^{n} p(r_i) F_{ri}[v](t)) \\ &= OP[v](t)^T P \end{aligned} \tag{5.11}$$

where $OPv = [v, F_{r1}(v), \ldots, F_{rn}(v)] \in R^{1\times(n+1)}$ represents a vector comprising the outputs of the play operators. Notably, this vector is discernible, being reliant on the input signals v and the thresholds r_i associated with the play operators. The thresholds are user-defined, while the control signals are accessible. $P = [Bp_0, Bp(r_1), \ldots, Bp(r_n)]^T \in R^{(n+1)\times 1}$ denotes a vector embodying the weights intended for estimation. The input to the dynamics $Bw(t)$ can be presented as the result of the product between these two components.

5.4 Controller Design

Leveraging the properties delineated above, the system model denoted as (5.1) can be expressed in the subsequent manner:

$$\dot{x} = \varphi(x)^T \theta + \Delta + OP[v](t)^T P \tag{5.12}$$

where θ embodies the vector of unidentified parameters, $\varphi(x)$ stands for the associated regressor matrix, Δ represents disturbances, $OP[v]$ signifies the vector containing the outputs derived from the fundamental play operators, P denotes the vector of undetermined weights within the PI hysteresis model.

Motivated by the adaptive controller proposed in [76], the current approach aims to concurrently learn the system's dynamic parameters θ and the enigmatic hysteresis weights P in an online fashion throughout the tracking control process. Moreover, to effectively address the influence of disturbances Δ, the design of the controller for this novel system capitalizes on the adaptive robust control (ARC) methodology introduced in [73].

5.4.1 Controller Structure

In the design of the adaptive robust controller, the following variables come into play:

$$\begin{cases} e = x - x_d \\ \tilde{\theta} = \theta - \hat{\theta} \\ \tilde{P} = P - \hat{P} \end{cases} \tag{5.13}$$

where$e$ represents the tracking error of the system, $\hat{\theta}$ signifies the estimated dynamic parameters vector θ, $\tilde{\theta}$ embodies the estimation error associated with the dynamic parameters θ, $\hat{P}$ denotes the estimated hysteresis weights vector P, $\tilde{P}$ stands for the estimation error pertaining to the weights vector P.

Hence, the controller can be formulated as follows:

$$v = \Pi_{\hat{P}}^{-1}[u] \tag{5.14}$$

where u represents a virtual adaptive robust control (ARC) signal, v stands for the actual control signal, $\Pi_{\hat{W}}^{-1}$ denotes the inverse of the Prandtl-Ishlinskii hysteresis model based on the estimated weights $\hat{P}$.

Property 1 *When employing the control law (5.14), i.e., $u = OP[v]^T\hat{P}$, the output of the hysteresis actuator can be expressed as follows:*

$$\begin{aligned} w(t) = OP[v]^T P =& OP[v]^T(\hat{P} + \tilde{P}) \\ =& u + OP[v]^T\tilde{P} \end{aligned} \tag{5.15}$$

Hence, the output of the hysteresis actuators can be comprehended as comprising the virtual control law u and an associated estimation error term $OP[v]^T\tilde{P}$.

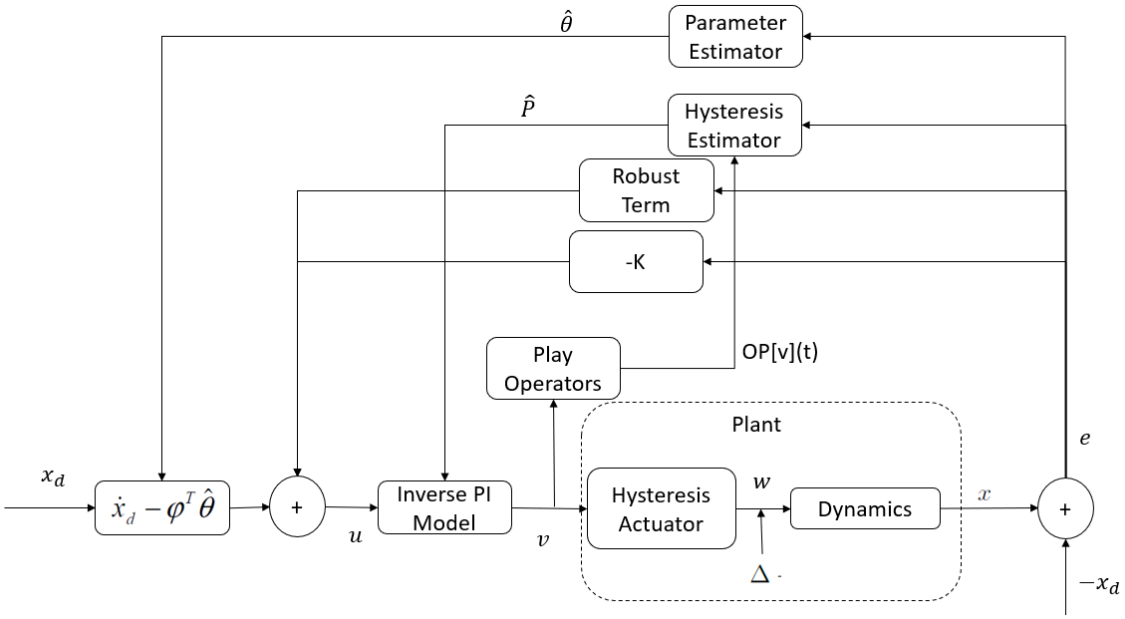

Figure 5.5: The structure of the controller

5.4.2 Virtual Control Law Design

As depicted in Figure 5.5, the formulation of the virtual control law $u(t)$ is illustrated:

$$u = -\varphi(x)^T\hat{\theta} + \dot{x}_d - Ke + u_r \tag{5.16}$$

where K denotes the control feedback gain, $-\varphi(x)^T\hat{\theta} + \dot{x}_d$ represents the feed-forward term, u_r signifies the robust term, which will be elaborated upon in the subsequent design process.

5.4.3 Dynamic Parameter and Hysteresis Adaptation

Due to the influence of system disturbances, the conventional adaptation law [76] is enhanced by integrating a discontinuous projection operator [73]:

Figure

$$\dot{\hat{\theta}} = Proj(\hat{\theta}, \Gamma_1\varphi e) \tag{5.17}$$

where $\Gamma_1 = diag(\gamma_{1,1}, \gamma_{1,2}, \ldots, \gamma_{1,m})$ denotes the learning gain matrix for the dynamic parameters, $Proj(\hat{\theta}, \cdot)$ represents the discontinuous projection operation, which is detailed as follows:

$$Proj(\hat{\theta}_i, \cdot_i) = \begin{cases} 0 & if\ \theta_i = \theta_{imax}\ and\ \cdot_i > 0 \\ 0 & if\ \theta_i = \theta_{imin}\ and\ \cdot_i < 0 \\ \cdot_i & else \end{cases} \tag{5.18}$$

where $\hat{\theta}_i$ signifies the estimated value of the i_{th} parameter within θ. θ_{max} and θ_{min} represent the upper and lower bounds of the parameter values. Utilizing this projection operator, the estimation θ gains advantages from the ensuing two properties:

$$\theta_{min} < \hat{\theta} < \theta_{max} \tag{5.19}$$

and

$$-e^T \varphi^T \tilde{\theta} + Proj(\hat{\theta}, \Gamma_1 \varphi e) \Gamma_1^{-1} \tilde{\theta} \leq 0 \tag{5.20}$$

which will play a crucial role in the subsequent stability analysis of the controller.

Likewise, the tuning of hysteresis estimations involving the weight vector $\hat{P}$ can also be formulated with the assistance of the projection operator.

$$\dot{\hat{P}} = Proj(\hat{P}, \Gamma_2 OP[v]e) \tag{5.21}$$

where $\Gamma_2 = diag(\gamma_{2,0}, \gamma_{2,1}, \ldots, \gamma_{2,n})$ represents the learning gain matrix for the hysteresis weights.

$$Proj(\hat{P}, \cdot) = \begin{cases} 0 & if\ P_i = P_{imax}\ and\ \cdot_i > 0 \\ 0 & if\ P_i = P_{imin}\ and\ \cdot_i < 0 \\ \cdot_i & else \end{cases} \tag{5.22}$$

Moreover, the adaptation of the hysteresis weights P can draw benefits from the properties (5.19) and (5.20).

5.4.4 Stability Analysis

In order to ensure the stability of the proposed controller and facilitate the design of the robust term u_r, the subsequent Lyapunov candidate is introduced:

$$V = V_s + V_\theta + V_P = \frac{1}{2}(e^T e + \tilde{\theta}^T \Gamma_1^{-1} \tilde{\theta} + \tilde{P}^T \Gamma_2^{-1} \tilde{P}) \tag{5.23}$$

Subsequently, the derivative $\dot{V}$ is determined as follows:

$$\dot{V} = e^T \dot{e} + \tilde{\theta}^T \Gamma_1^{-1} \dot{\tilde{\theta}} + \tilde{P}^T \Gamma_2^{-1} \dot{\tilde{P}} \tag{5.24}$$

By substituting controller (5.14) and (5.16) into the system dynamics (5.1), the error dynamics of the closed-loop system can be derived as:

$$\dot{e} + Ke = -\varphi^T \tilde{\theta} - OP[v]^T \tilde{P} + \Delta + u_r \tag{5.25}$$

Combining equations (5.24) and (5.25), we can obtain:

$$\begin{cases} \dot{V} = -e^T K e + e^T (\Delta + u_r) \\ \dot{V}_s = -e^T K e + e^T (-\varphi^T \tilde{\theta} - OP[v]^T \tilde{P} + \Delta + u_r) \end{cases} \tag{5.26}$$

Consequently, by selecting the robust term u_r as:

$$\begin{aligned} u_r = -\frac{1}{4\varepsilon} [&\|\theta_{max} - \theta_{min}\|^2 \|\varphi\|^2 \\ &+ \|P_{max} - P_{min}\|^2 \|OP[v]\|^2 + \delta] e \end{aligned} \tag{5.27}$$

where ε is a parameter to be designated, δ signifies the disturbance limit Δ.

As such, the derivative of the Lyapunov candidate becomes:

$$\dot{V}_s \leq -e^T K e + \varepsilon \tag{5.28}$$

Consequently, both V and V_s exhibit non-increasing behavior, affirming that the designed controller ensures the system's stability.

5.5 Simulation Study

In this section, the aforementioned approach will be demonstrated through the application to a simple nonlinear system, which can be defined as follows:

$$\dot{x} = -3x^2 + \Delta + w \tag{5.29}$$

in which

$$\begin{cases} \phi(x) & = -x^2 \\ \theta & = 3 \end{cases} \tag{5.30}$$

For modeling the hysteresis effects of the actuators, the PI model is adopted, with parameters set as $p_0 = 1$ and $p_r = e^{(-0.1r)}$.

The desired trajectory is defined as $x_d = 1 - cos(t)$. The disturbance is specified as $\Delta = 0.7(-1)^{round(t)}$, oscillating periodically between $+0.7$ and -0.7. The simulation is conducted within the Simulink environment, with a maximum step size of $1ms$.

The controller parameters are detailed in Table 5.1. The results of the simulation are depicted in Figures 5.6-5.8.

Table 5.1: Controller Parameters

Γ_1	100	Γ_2	$100I$
K	10		
δ	0.7	ε	0.5
$\hat{\theta}_0$	2	$\hat{P}_0$	0.5P
θ_{min}	1	P_{min}	5P
θ_{max}	5	P_{max}	0.2P

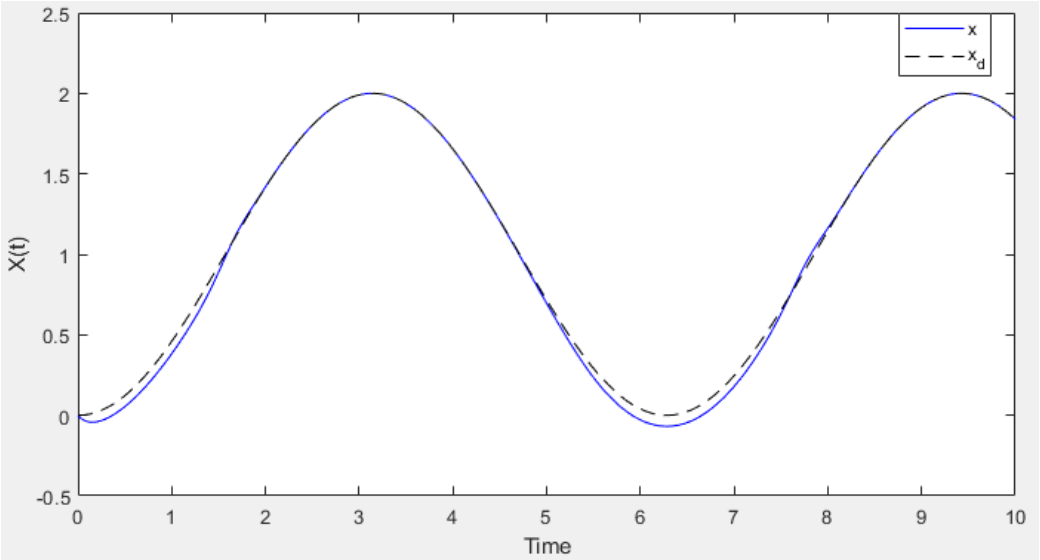

Figure 5.6: Trajectory tracking of the developed controller, with disturbances

As observed in Figures 5.6 and 5.8, it is evident that despite the challenges elucidated earlier, the proposed controller is able to ensure commendable performance. Furthermore, the controller is adept at estimating unknown system dynamic

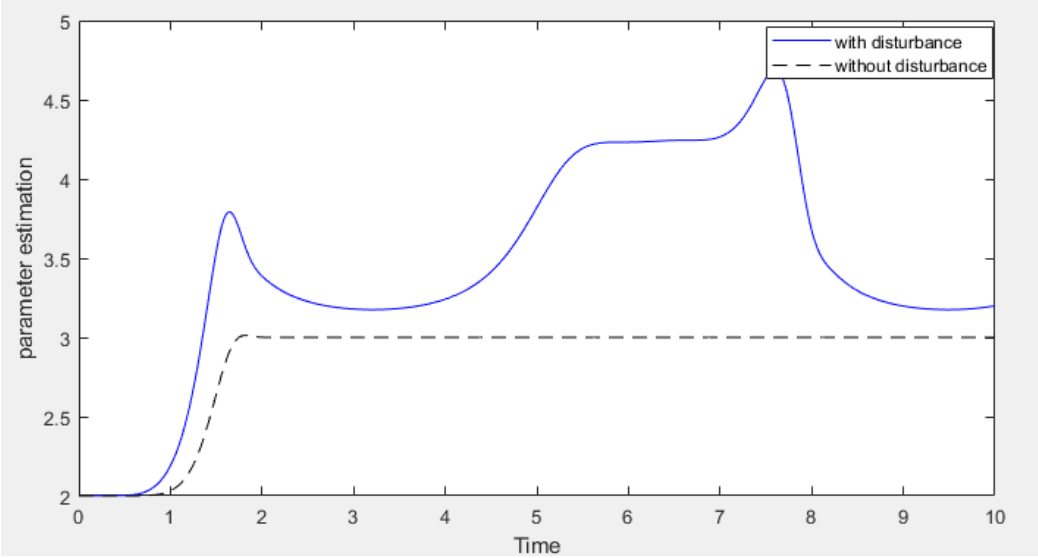

Figure 5.7: Prediction of system parameter $\theta = 3$, with and without disturbances

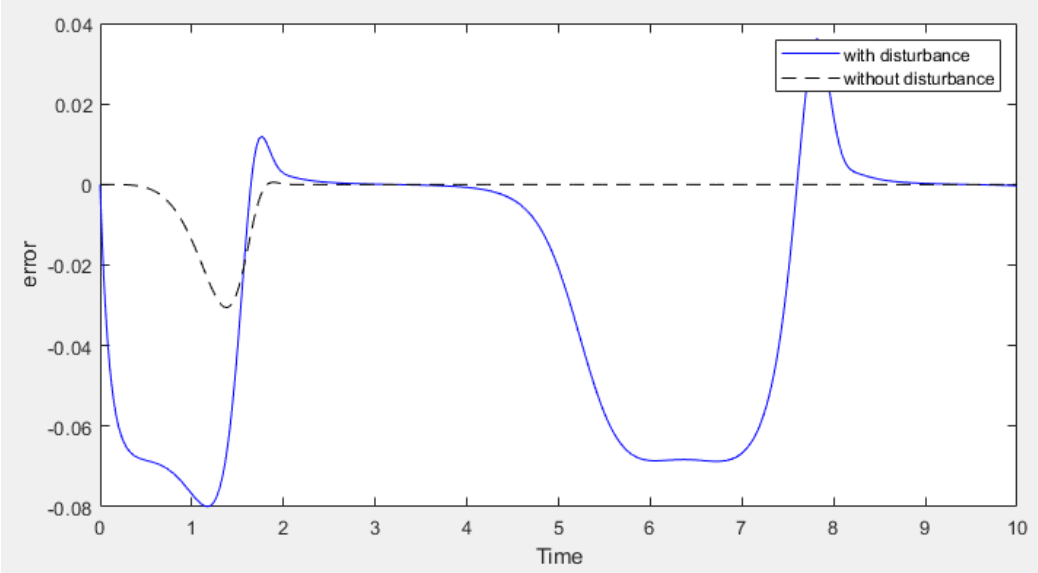

Figure 5.8: Tracking error of the system with hysteresis actuator, with and without disturbances

parameters, as evident from Figure 5.7. Notably, when disturbances are absent, the estimation rapidly converges to the actual parameter value of $\theta = 3$.

5.6 Experimental verification

To further validate the efficacy of the proposed control approach, the developed algorithm will be implemented on the conical actuators, as detailed in Chapter 1.3.

The identified parameters in Chapter 4.6 will serve as initial estimations for the system dynamics parameters and hysteresis density functions. In order to acquire velocity signals for the Dielectric Elastomer Actuators (DEAs), a first-order low-pass filter represented by $H(S) = \frac{1}{1+0.2S}$ will be applied to the derivative of the position signals.

A reference trajectory of $x_d = 0.1(0.5 + \sin(t))\ mm$ is chosen for the validation. Figure 5.9 illustrates the system's response, showing that at the outset, the system exhibits some errors, which are subsequently effectively mitigated by the controller. Figure 5.10 provides a visual representation of the control signals employed for the tracking task.

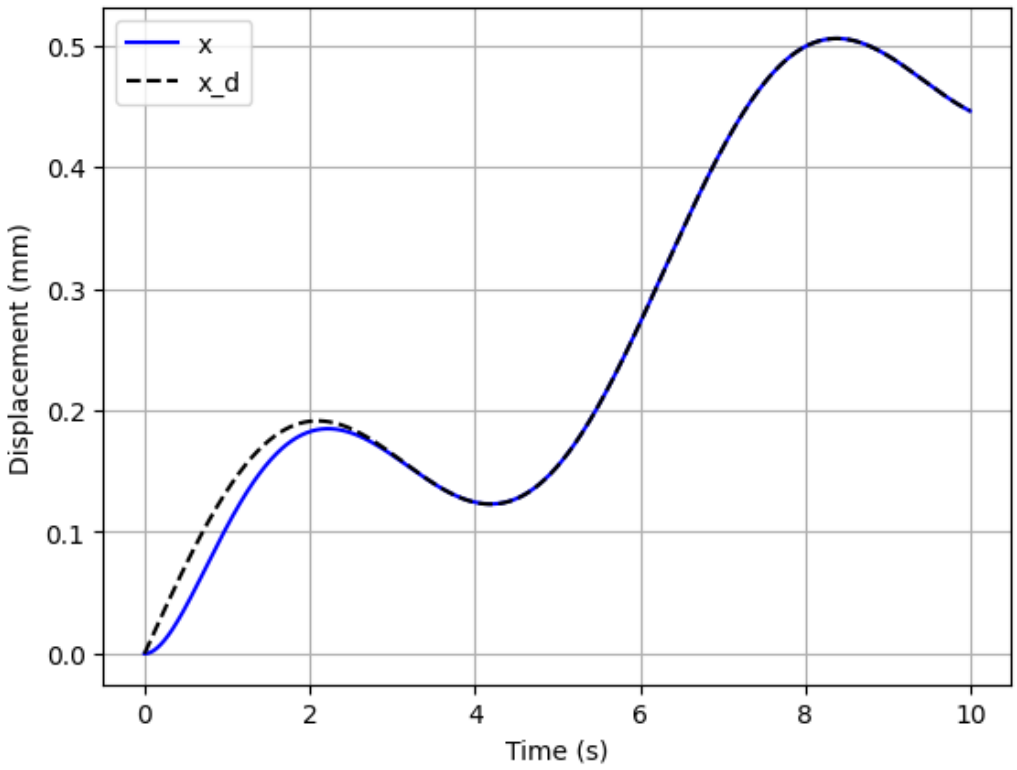

Figure 5.9: Trajectory tracking for $x_d = 0.1(0.5 + \sin(t))\ mm$

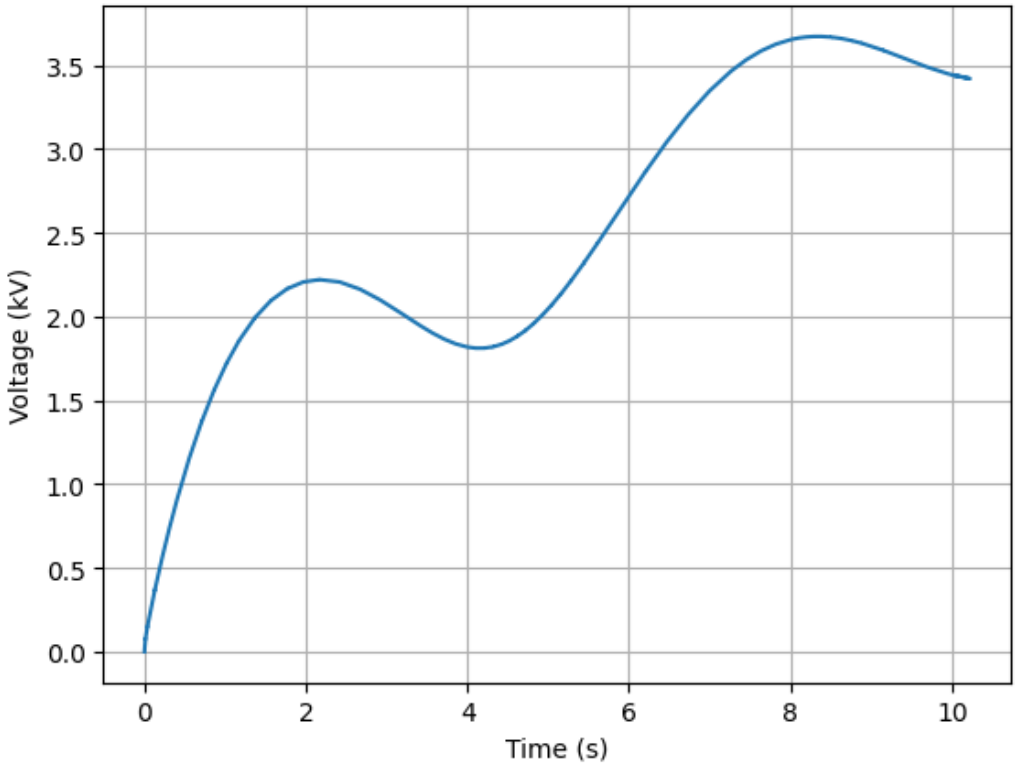

Figure 5.10: Control signal for $x_d = 0.1(0.5 + \sin(t))\ mm$

5.7 Concluding Remarks

In this chapter, we present an adaptive robust controller as a viable solution to tackle the challenges posed by uncertain dynamic systems coupled with actuators characterized by unknown hysteresis and exposed to external disturbances. The analysis of the Prandtl-Ishlinskii (PI) hysteresis model has yielded significant insights that we leverage in this endeavor. By harnessing these insights, we explore the integration of the hysteresis model with the adaptive robust control approach. The resulting adaptive robust controller demonstrates proficiency in achieving tracking objectives while simultaneously estimating system parameters, even in scenarios characterized by limited system information and the presence of disturbances. We substantiate the effectiveness of the proposed controller through a comprehensive evaluation involving simulations and experimental results.

Chapter 6

Conclusions and Future Work

6.1 Concluding Remarks

Dielectric Elastomer (DE) enabled actuators exhibit great promise for application in the field of soft robotics, owing to their exceptional performance characteristics. However, the complicated nonlinear nature of Dielectric Elastomer Actuators (DEAs), which includes complexities such as hysteresis and numerous dependencies, makes the modeling and control of DEAs inherently challenging. This dissertation represents a comprehensive exploration of the modeling and control of DEAs, with the overarching objective of laying a solid foundation for the advancement of soft robotic applications integrating DE technology. The principal accomplishments of this research endeavor can be succinctly summarized as follows:

1. **Experimental Analysis:** A comprehensive series of experimental tests were conducted to analyze the input-output characteristics of Dielectric Elastomer Actuators (DEAs) across varying input amplitudes ($6.0kV - 8.0kV$), frequencies ($0.2Hz - 1Hz$), and mechanical loads ($m = 100g - 500g$). The results revealed the intricate and complex nature of DEA responses, emphasizing their dependence on input frequencies, amplitudes, and external mechanical loads. These findings provide essential insights into DEA behavior, forming the foundation for subsequent modeling and control strategies.

2. **Physics-Based Models:** Two distinct physics-based models for conical and planar DEAs were introduced, based on the principles of free energy within viscoelastic materials. These models accurately capture the intricate behaviors of DEAs, including their complex dependencies on various factors. Experimental validations demonstrated the models' effectiveness in representing

DEA behaviors, enhancing our understanding and control of these dynamic systems.

3. **Data-in-Loop Model:** To address the need for actuator-specific details in previous models, a versatile data-in-loop model was proposed. This innovative model utilizes nonlinear blocks, incorporating features such as creep and hysteresis, to represent intricate DEA behaviors without relying on geometry-specific information. This approach accommodates the complex dependencies inherent in DEA systems.

4. **Robust Adaptive Controller:** Nonlinear effects in DEAs can lead to control performance issues. To mitigate these effects, feedforward inverse compensation methods were applied for controller design. A PI hysteresis-based model characterizes the nonlinear impact in DEAs, and the direct inverse compensation technique is employed to derive the inverse of the PI model. This forms the basis for a robust adaptive controller, aimed at improving control performance and addressing the challenges posed by dynamic behaviors in DEAs. Simulation and experimental results validated the efficiency of the developed controller.

These achievements collectively contribute to advancing our understanding, modeling, and control of DEAs, paving the way for their more effective utilization in soft robotics applications.

6.2 Recommendations for Future Works

Continuing the trajectory of investigation within this dissertation's research domain, the following prospective research avenues hold considerable promise for future exploration:

1. Building upon the physics-based model, there is a compelling need to develop an automated modeling algorithm that incorporates the actuators' parameters seamlessly. This algorithmic approach aims to streamline the modeling process, ensuring efficiency and accuracy in predicting the behavior of the actuators.

2. Building upon the established data-in-loop model, it becomes imperative to incorporate considerations for the interaction with the environment. This step is essential to not only enhance the model's robustness and accuracy but also

to enable the seamless integration of the developed methods into practical applications within the realm of soft robotics.

3. The advanced inverse-based robust adaptive controller, as it stands, possesses considerable potential for further extension, enabling its applicability to intricate nonlinear behaviors exhibited by actuators and complex system dynamics. This extension would not only enhance the controller's versatility but also broaden its scope of application in diverse engineering scenarios.

6.3 Publications

The findings from this dissertation research have been disseminated through publication and submission across various esteemed journals and international conferences, as detailed below.

Book Chapters:

[B1] Y. Wang, J. Wu, W. Ye, P. Huang, K. Ohnishi, and C.-Y. Su, "Dielectric Elastomer Intelligent Devices for Soft Robots," Developments in Advanced Control and Intelligent Automation for Complex Systems, vol. 329, Springer Nature, 2021.

Journal Publications:

[J1] J. Wu, Y. Wang, W. Ye, J. She, C.-Y. Su, " Dynamic modelling of liquid crystal elastomer actuators based on a physics-phenomenon-combined approach," International Journal of System Sciences, 2022, doi: 10.1080/00207721.2022.2163205

[J2] J. Wu, W. Ye, Y. Wang, C.-Y. Su, "Modeling Based on a Two-step Parameter Identification Strategy for Liquid Crystal Elastomer Actuator Considering Dynamic Phase Transition Process," IEEE Transactions on Cybernetics, 2022, doi: 10.1109/TCYB.2022.3179433

[J3] J. Wu, Y. Wang, W. Ye, C.-Y. Su, "Positioning Control of Liquid Crystal Elastomer Actuator Based on Double Closed-Loop System Structure", Control Engineering Practice, vol. 123, pp. 105136, 2022.

[J4] J. Wu, W. Ye, Y. Wang and C. -Y. Su, "A General Position Control Method for Planar Underactuated Manipulators With Second-Order Nonholonomic Constraints," IEEE Transactions on Cybernetics, vol. 51, no. 9, pp. 4733-4742, Sept. 2021.

[J5] J. Wu, W. Ye, Y. Wang, and C.-Y. Su, "Modeling of Photo-Responsive Liquid Crystal Elastomer Actuators," Information Sciences, vol. 560, pp. 441–455, Jun. 2021.

[J6] Q. Lu, D. Zhang, W. Ye, J. Fan, S. Liu and C. -Y. Su, "Targeting Posture

Control With Dynamic Obstacle Avoidance of Constrained Uncertain Wheeled Mobile Robots Including Unknown Skidding and Slipping," IEEE Transactions on Systems, Man, and Cybernetics: Systems, vol. 51, no. 11, pp. 6650-6659, Nov. 2021.

[J7] H. Xiao, J. Wu, W. Ye, and Y. Wang, "Dynamic Modeling of Dielectric Elastomer Actuators Based on Thermodynamic Theory," Mechanics of Advanced Materials and Structures, pp. 1-10, Nov. 2020.

[J8] P. Huang, W. Ye, and Y. Wang, "Dynamic Modeling of Dielectric Elastomer Actuator With Conical Shape," PLoS ONE, vol. 15, no. 8, p. e0235229, Aug. 2020.

[J9] P. Zhang, X. Lai, Y. Wang, C.-Y. Su, W. Ye, and M. Wu, "A Novel Position-Posture Control Method Using Intelligent Optimization for Planar Underactuated Mechanical Systems," Mechanism and Machine Theory, vol. 140, pp. 258–273, Oct. 2019.

[J10] J. Wu, Y. Wang, W. Ye, and C.-Y. Su, "Control Strategy Based on Fourier Transformation and Intelligent Optimization for Planar Pendubot," Information Sciences, vol. 491, pp. 279–288, Jul. 2019.

[J11] W. Ye, Z. Li, C. Yang, F. Chen, and C.-Y. Su, "Motion Detection Enhanced Control of an Upper Limb Exoskeleton Robot for Rehabilitation Training," International Journal of Humanoid Robotics., vol. 14, no. 01, p. 1650031, Mar. 2017.

[J12] Z. Li, Q. Ge, W. Ye, and P. Yuan, "Dynamic Balance Optimization and Control of Quadruped Robot Systems With Flexible Joints," IEEE Transactions on Systems, Man, and Cybernetics: Systems, vol. 46, no. 10, pp. 1338–1351, Oct. 2016.

Refereed Conference Proceedings:

[C1] W. Ye, F. Aghili, J. Wu, and C.-Y. Su, "Robust Adaptive Control of Uncertain Systems Preceded with Unknown Hysteresis Actuators", in 2021 IEEE 7th International Conference on Control Science and Systems Engineering (ICCSSE), Virtual, Aug. 2021.

[C2] H. Xiao, J. Wu, W. Ye, and Y. Wang, "Dynamic Modeling for Dielectric Elastomer Actuators Based on LSTM Deep Neural Network," in 2020 5th International Conference on Advanced Robotics and Mechatronics (ICARM), Shenzhen, China, Dec. 2020.

[C3] P. Huang, J. Wu, W. Ye, and Y. Wang, "Study of Soft Force and Displacement Sensor Based on Dielectric Elastomer," in 2020 5th International Conference on Advanced Robotics and Mechatronics (ICARM), Shenzhen, China, Dec. 2020.

[C4] W. Ye, F. Aghili, and J. Wu, "Adaptive Control of a Class of Nonlinear Systems with Unknown Prandtl-Ishlinskii Hysteresis," in 2019 IEEE 4th International Conference on Advanced Robotics and Mechatronics (ICARM), Toyonaka, Japan,

Jul. 2019.

[C5] J. Wu, Y. Wang, and W. Ye, "A One-Stage Control Strategy for Planar Underactuated Manipulators," in 2019 IEEE 4th International Conference on Advanced Robotics and Mechatronics (ICARM), Toyonaka, Japan, Jul. 2019.

[C6] Q. Lu et al., "Distributed Leader-follower Formation Control of Nonholonomic Mobile Robots," 8th IFAC Symposium on Mechatronic Systems MECHATRONICS 2019, Vienna, Austria, 4–6 September 2019.

[C7] W. Ye and F. Aghili, "Robot Manipulators Control with Parameters Adaptation and State Estimation," in 2018 3rd International Conference on Advanced Robotics and Mechatronics (ICARM), Singapore, Jul. 2018.

References

[1] D. Rus and M. T. Tolley, "Design, fabrication and control of soft robots," *Nature*, vol. 521, no. 7553, p. 467, 2015.

[2] G.-Y. Gu, J. Zhu, L.-M. Zhu, and X. Zhu, "A survey on dielectric elastomer actuators for soft robots," *Bioinspiration and Biomimetics*, vol. 12, no. 1, p. 011003, 2017.

[3] R. Sarban, B. Lassen, and M. Willatzen, "Dynamic electromechanical modeling of dielectric elastomer actuators with metallic electrodes," *IEEE/ASME Transactions on Mechatronics*, vol. 17, no. 5, pp. 960–967, 2012.

[4] A. O'Halloran, F. O'malley, and P. McHugh, "A review on dielectric elastomer actuators, technology, applications, and challenges," *Journal of Applied Physics*, vol. 104, no. 7, 2008.

[5] A. D. Marchese, R. Tedrake, and D. Rus, "Dynamics and trajectory optimization for a soft spatial fluidic elastomer manipulator," *The International Journal of Robotics Research*, vol. 35, no. 8, pp. 1000–1019, 2016.

[6] C. D. Onal and D. Rus, "Autonomous undulatory serpentine locomotion utilizing body dynamics of a fluidic soft robot," *Bioinspiration and Biomimetics*, vol. 8, no. 2, p. 026003, 2013.

[7] B. Mazzolai, L. Margheri, M. Cianchetti, P. Dario, and C. Laschi, "Soft-robotic arm inspired by the octopus: Ii. from artificial requirements to innovative technological solutions," *Bioinspiration and Biomimetics*, vol. 7, no. 2, p. 025005, 2012.

[8] M. T. Tolley, R. F. Shepherd, B. Mosadegh, K. C. Galloway, M. Wehner, M. Karpelson, R. J. Wood, and G. M. Whitesides, "A resilient, untethered soft robot," *Soft robotics*, vol. 1, no. 3, pp. 213–223, 2014.

[9] A. D. Marchese, C. D. Onal, and D. Rus, "Autonomous soft robotic fish capable of escape maneuvers using fluidic elastomer actuators," *Soft robotics*, vol. 1, no. 1, pp. 75–87, 2014.

[10] R. F. Shepherd, F. Ilievski, W. Choi, S. A. Morin, A. A. Stokes, A. D. Mazzeo, X. Chen, M. Wang, and G. M. Whitesides, "Multigait soft robot," *Proceedings of the National Academy of Sciences*, vol. 108, no. 51, pp. 20400–20403, 2011.

[11] S. A. Morin, R. F. Shepherd, S. W. Kwok, A. A. Stokes, A. Nemiroski, and G. M. Whitesides, "Camouflage and display for soft machines," *Science*, vol. 337, no. 6096, pp. 828–832, 2012.

[12] S. Xu, Y. Zhang, J. Cho, J. Lee, X. Huang, L. Jia, J. A. Fan, Y. Su, J. Su, H. Zhang, *et al.*, "Stretchable batteries with self-similar serpentine interconnects and integrated wireless recharging systems," *Nature Communications*, vol. 4, p. 1543, 2013.

[13] G. Robinson and J. B. C. Davies, "Continuum robots-a state of the art," in *Proceedings 1999 IEEE international conference on robotics and automation (Cat. No. 99CH36288C)*, vol. 4, pp. 2849–2854, IEEE, 1999.

[14] X. Zhao, "Multi-scale multi-mechanism design of tough hydrogels: building dissipation into stretchy networks," *Soft Matter*, vol. 10, no. 5, pp. 672–687, 2014.

[15] S. Kim, C. Laschi, and B. Trimmer, "Soft robotics: a bioinspired evolution in robotics," *Trends in Biotechnology*, vol. 31, no. 5, pp. 287–294, 2013.

[16] P. Brochu and Q. Pei, "Advances in dielectric elastomers for actuators and artificial muscles," *Macromolecular Rapid Communications*, vol. 31, no. 1, pp. 10–36, 2010.

[17] C. Laschi and M. Cianchetti, "Soft robotics: new perspectives for robot bodyware and control," *Frontiers in Bioengineering and Biotechnology*, vol. 2, p. 3, 2014.

[18] F. Carpi, S. Bauer, and D. De Rossi, "Stretching dielectric elastomer performance," *Science*, vol. 330, no. 6012, pp. 1759–1761, 2010.

[19] S. Bauer, S. Bauer-Gogonea, I. Graz, M. Kaltenbrunner, C. Keplinger, and R. Schwödiauer, "25th anniversary article: a soft future: from robots and sensor skin to energy harvesters," *Advanced Materials*, vol. 26, no. 1, pp. 149–162, 2014.

[20] R. E. Pelrine, R. D. Kornbluh, and J. P. Joseph, "Electrostriction of polymer dielectrics with compliant electrodes as a means of actuation," *Sensors and Actuators A: Physical*, vol. 64, no. 1, pp. 77–85, 1998.

[21] R. Pelrine, R. Kornbluh, Q. Pei, and J. Joseph, "High-speed electrically actuated elastomers with strain greater than 100%," *Science*, vol. 287, no. 5454, pp. 836–839, 2000.

[22] R. J. Webster III and B. A. Jones, "Design and kinematic modeling of constant curvature continuum robots: A review," *The International Journal of Robotics Research*, vol. 29, no. 13, pp. 1661–1683, 2010.

[23] E. D. Wilson, T. Assaf, M. J. Pearson, J. M. Rossiter, S. R. Anderson, and J. Porrill, "Bioinspired adaptive control for artificial muscles," in *Biomimetic and Biohybrid Systems: Second International Conference, Living Machines 2013, London, UK, July 29–August 2, 2013. Proceedings 2*, pp. 311–322, Springer, 2013.

[24] M. Y. Ozsecen and C. Mavroidis, "Nonlinear force control of dielectric electroactive polymer actuators," in *Electroactive Polymer Actuators and Devices (EAPAD) 2010*, vol. 7642, pp. 673–680, SPIE, 2010.

[25] S. Xie, P. Ramson, D. Graaf, E. Calius, and I. Anderson, "An adaptive control system for dielectric elastomers," in *2005 IEEE International Conference on Industrial Technology*, pp. 335–340, IEEE, 2005.

[26] I. Krakovskỳ, T. Romijn, and A. Posthuma de Boer, "A few remarks on the electrostriction of elastomers," *Journal of Applied Physics*, vol. 85, no. 1, pp. 628–629, 1999.

[27] M. Mooney, "A theory of large elastic deformation," *Journal of Applied Physics*, vol. 11, no. 9, pp. 582–592, 1940.

[28] R. W. Ogden, "Large deformation isotropic elasticity–on the correlation of theory and experiment for incompressible rubberlike solids," *Proceedings of the Royal Society of London. A. Mathematical and Physical Sciences*, vol. 326, no. 1567, pp. 565–584, 1972.

[29] O. H. Yeoh, "Characterization of elastic properties of carbon-black-filled rubber vulcanizates," *Rubber Chemistry and Technology*, vol. 63, no. 5, pp. 792–805, 1990.

[30] M. Wissler and E. Mazza, "Modeling of a pre-strained circular actuator made of dielectric elastomers," *Sensors and Actuators A: Physical*, vol. 120, no. 1, pp. 184–192, 2005.

[31] J.-S. Plante and S. Dubowsky, "On the performance mechanisms of dielectric elastomer actuators," *Sensors and Actuators A: Physical*, vol. 137, no. 1, pp. 96–109, 2007.

[32] Z. Suo, "Theory of dielectric elastomers," *Acta Mechanica Solida Sinica*, vol. 23, no. 6, pp. 549–578, 2010.

[33] L. G. Treloar, "The physics of rubber elasticity," 1975.

[34] A. N. Gent, "A new constitutive relation for rubber," *Rubber chemistry and technology*, vol. 69, no. 1, pp. 59–61, 1996.

[35] J. Zhu, S. Cai, and Z. Suo, "Nonlinear oscillation of a dielectric elastomer balloon," *Polymer International*, vol. 59, no. 3, pp. 378–383, 2010.

[36] H. Xiao, J. Wu, W. Ye, and Y. Wang, "Dynamic modeling of dielectric elastomer actuators based on thermodynamic theory," *Mechanics of Advanced Materials and Structures*, vol. 29, no. 11, pp. 1543–1552, 2022.

[37] U. Gupta, Y. Wang, H. Ren, and J. Zhu, "Dynamic modeling and feedforward control of jaw movements driven by viscoelastic artificial muscles," *IEEE/ASME transactions on mechatronics*, vol. 24, no. 1, pp. 25–35, 2019.

[38] G.-Y. Gu, U. Gupta, J. Zhu, L.-M. Zhu, and X. Zhu, "Modeling of viscoelastic electromechanical behavior in a soft dielectric elastomer actuator," *IEEE Transactions on Robotics*, vol. 33, no. 5, pp. 1263–1271, 2017.

[39] B.-X. Xu, R. Mueller, A. Theis, M. Klassen, and D. Gross, "Dynamic analysis of dielectric elastomer actuators," *Applied Physics Letters*, vol. 100, no. 11, 2012.

[40] J. Sheng, H. Chen, L. Liu, J. Zhang, Y. Wang, and S. Jia, "Dynamic electromechanical performance of viscoelastic dielectric elastomers," *Journal of Applied Physics*, vol. 114, no. 13, 2013.

[41] M. M. Joglekar, "An energy-based approach to extract the dynamic instability parameters of dielectric elastomer actuators," *Journal of Applied Mechanics*, vol. 81, no. 9, p. 091010, 2014.

[42] M. Sassano and A. Astolfi, "Optimality and passivity of input-quadratic nonlinear systems," *IEEE Transactions on Automatic Control*, vol. 65, no. 8, pp. 3229–3240, 2020.

[43] S. Rosset, B. M. O'Brien, T. Gisby, D. Xu, H. R. Shea, and I. A. Anderson, "Self-sensing dielectric elastomer actuators in closed-loop operation," *Smart Materials and Structures*, vol. 22, no. 10, p. 104018, 2013.

[44] G. Tao and P. V. Kokotovic, "Adaptive control of plants with unknown hystereses," *IEEE Transactions on Automatic Control*, vol. 40, no. 2, pp. 200–212, 1995.

[45] P. Krejci and K. Kuhnen, "Inverse control of systems with hysteresis and creep," *IEE Proceedings-Control Theory and Applications*, vol. 148, no. 3, pp. 185–192, 2001.

[46] J. Zou and G. Gu, "Feedforward control of the rate-dependent viscoelastic hysteresis nonlinearity in dielectric elastomer actuators," *IEEE Robotics and Automation Letters*, vol. 4, no. 3, pp. 2340–2347, 2019.

[47] P. Huang, J. Wu, C.-Y. Su, and Y. Wang, "Tracking control of soft dielectric elastomer actuator based on nonlinear pid controller," *International Journal of Control*, pp. 1–11, 2022.

[48] C. M. Druitt and G. Alici, "Intelligent control of electroactive polymer actuators based on fuzzy and neurofuzzy methodologies," *IEEE/ASME Transactions on Mechatronics*, vol. 19, no. 6, pp. 1951–1962, 2014.

[49] L. Li, J. Li, L. Qin, J. Cao, M. S. Kankanhalli, and J. Zhu, "Deep reinforcement learning in soft viscoelastic actuator of dielectric elastomer," *IEEE Robotics and Automation Letters*, vol. 4, no. 2, pp. 2094–2100, 2019.

[50] G.-Y. Gu, U. Gupta, J. Zhu, L.-M. Zhu, and X.-Y. Zhu, "Feedforward deformation control of a dielectric elastomer actuator based on a nonlinear dynamic model," *Applied Physics Letters*, vol. 107, no. 4, 2015.

[51] G. Rizzello, M. Hodgins, D. Naso, A. York, and S. Seelecke, "Modeling of the effects of the electrical dynamics on the electromechanical response of a deap circular actuator with a mass–spring load," *Smart Materials and Structures*, vol. 24, no. 9, p. 094003, 2015.

[52] C. Zhang, W. Sun, H. Chen, L. Liu, B. Li, and D. Li, "Electromechanical deformation of conical dielectric elastomer actuator with hydrogel electrodes," *Journal of Applied Physics*, vol. 119, no. 9, 2016.

[53] D. Roylance, "Engineering viscoelasticity," *Department of Materials Science and Engineering–Massachusetts Institute of Technology, Cambridge MA*, vol. 2139, pp. 1–37, 2001.

[54] J. Zou and G. Gu, "High-precision tracking control of a soft dielectric elastomer actuator with inverse viscoelastic hysteresis compensation," *IEEE/ASME Transactions on Mechatronics*, vol. 24, no. 1, pp. 36–44, 2018.

[55] C. Cao, S. Burgess, and A. T. Conn, "Toward a dielectric elastomer resonator driven flapping wing micro air vehicle," *Frontiers in Robotics and AI*, vol. 5, p. 137, 2019.

[56] B. Mokaberi and A. A. Requicha, "Compensation of scanner creep and hysteresis for afm nanomanipulation," *IEEE Transactions on Automation Science and Engineering*, vol. 5, no. 2, pp. 197–206, 2008.

[57] F. Preisach, "Über die magnetische nachwirkung," *Zeitschrift für physik*, vol. 94, no. 5-6, pp. 277–302, 1935.

[58] M. Brokate and J. Sprekels, *Hysteresis and phase transitions*, vol. 121. Springer Science & Business Media, 2012.

[59] H. T. Banks and A. Kurdila, "Hysteretic control influence operators representing smart material actuators: identification and approximation," in *Proceedings of 35th IEEE Conference on Decision and Control*, vol. 4, pp. 3711–3716, IEEE, 1996.

[60] A. Visintin and A. Sprekels, "Differential models of hysteresis," *ZAMM-Zeitschrift fur Angewandte Mathematik und Mechanik*, vol. 76, no. 10, pp. 144–144, 1996.

[61] I. D. Mayergoyz, *Mathematical models of hysteresis*. Springer Science & Business Media, 2012.

[62] M. Ismail, F. Ikhouane, and J. Rodellar, "The hysteresis bouc-wen model, a survey," *Archives of Computational Methods in Engineering*, vol. 16, pp. 161–188, 2009.

[63] C.-Y. Su, Y. Stepanenko, J. Svoboda, and T.-P. Leung, "Robust adaptive control of a class of nonlinear systems with unknown backlash-like hysteresis," *IEEE Transactions on Automatic Control*, vol. 45, no. 12, pp. 2427–2432, 2000.

[64] M. A. Krasnosel'skii and A. V. Pokrovskii, *Systems with hysteresis*. Springer Science & Business Media, 2012.

[65] M. Brokate, "Some mathematical properties of the preisach model for hysteresis," *IEEE Transactions on Magnetics*, vol. 25, no. 4, pp. 2922–2924, 1989.

[66] P. Krejcı, *Hysteresis, convexity and dissipation in hyperbolic equations*. Tokyo: Gakkotosho, 1996.

[67] X. Zhao and Y. Tan, "Modeling hysteresis and its inverse model using neural networks based on expanded input space method," *IEEE Transactions on Control Systems Technology*, vol. 16, no. 3, pp. 484–490, 2008.

[68] Q. Xu, "Identification and compensation of piezoelectric hysteresis without modeling hysteresis inverse," *IEEE Transactions on Industrial Electronics*, vol. 60, no. 9, pp. 3927–3937, 2012.

[69] G.-Y. Gu, L.-M. Zhu, and C.-Y. Su, "Modeling and compensation of asymmetric hysteresis nonlinearity for piezoceramic actuators with a modified prandtl–ishlinskii model," *IEEE Transactions on Industrial Electronics*, vol. 61, no. 3, pp. 1583–1595, 2013.

[70] A. Isidori, *Nonlinear control systems: an introduction*. Springer Science & Business Media, 2013.

[71] D. C. Jiles and D. L. Atherton, "Theory of ferromagnetic hysteresis," *Journal of magnetism and magnetic materials*, vol. 61, no. 1-2, pp. 48–60, 1986.

[72] R. C. Smith and Z. Ounaies, "A domain wall model for hysteresis in piezoelectric materials," *Journal of Intelligent Material Systems and Structures*, vol. 11, no. 1, pp. 62–79, 2000.

[73] B. Yao and M. Tomizuka, "Adaptive robust control of siso nonlinear systems in a semi-strict feedback form," *Automatica*, vol. 33, no. 5, pp. 893–900, 1997.

[74] L. Prandtl, "Ein gedankenmodell zur kinetischen theorie der festen körper," *ZAMM-Journal of Applied Mathematics and Mechanics/Zeitschrift für Angewandte Mathematik und Mechanik*, vol. 8, no. 2, pp. 85–106, 1928.

[75] W. Ye, F. Aghili, and J. Wu, "Adaptive control of a class of nonlinear systems with unknown prandtl-ishlinskii hysteresis," in *2019 IEEE 4th International Conference on Advanced Robotics and Mechatronics (ICARM)*, pp. 1010–1015, IEEE, 2019.

[76] J.-J. E. Slotine and W. Li, "On the adaptive control of robot manipulators," *The International Journal of Robotics Research*, vol. 6, no. 3, pp. 49–59, 1987.